QATAR UNIVERSITY

COLLEGE OF ENGINEERING

AN EXPERIMENTAL AND NUMERICAL INVESTIGATION OF THE COMBINATION OF DIFFERENT DAMPER TYPES FOR IMPROVED CONTROL OF VIBRATION

BY

YOUSIF BABIKIR ALI BABIKIR BADRI

A Thesis Submitted to

the College of Engineering

in Partial Fulfillment of the Requirements for the Degree of

Master of Science in Mechanical Engineering

January 2022

COMMITTEE PAGE

The members of the Committee approve the Master's Thesis of
Yousif Babikir Ali Babikir Badri defended on 25/11/2021.

Sadok Sassi
Thesis/Dissertation Supervisor

Mohammed Hussein
Thesis/Dissertation Co-Supervisor

Jamil Renno
Thesis/Dissertation Co-Supervisor

Dr. Mansour Karkoub
Committee Member

Dr. Mohamed Roshun
Committee Member

Dr. Asan Muthalif
Committee Member

Approved:

Khalid Kamal Naji, Dean, College of Engineering

ABSTRACT

Badri, Yousif, Master, January: 2022, Master of Science in Mechanical Engineering.

Title:_An experimental and numerical investigation of the combination of different damper types for improved control of vibration.

Supervisors of Thesis: Sadok, Sassi, Mohammed Hussein, and Jamil Renno

Eliminating and reducing unwanted vibrations required a good knowledge of the dynamic system's fundamental components; mass, spring, and damper. Meanwhile, dampers are responsible for reducing the vibration's amplitudes and the time needed by a structure to reach its steady state. This research is focused on studying a combination of different dampers through computational and experimental approaches. Furthermore, parametric studies are conducted to investigate the parameters that affect each damper's damping behavior.

Two dampers were designed, manufactured, modeled, and tested through this study. Firstly, a hybrid damper was developed by integrating two damping technologies; Viscous Fluid Damper (VFD) and Particle Impact Damper (PID). The VFD used in this study was a Mono-tube commercial viscous damper used in the automobile suspension system. On the other hand, the PID part consisted of a circular plastic enclosure filled with Stainless Steel 15mm diameter bearing balls. The Fluid Impact Hybrid Damper (FIHD) was designed by attaching the PID part to the VFD piston rod. A shaker testing setup was developed to drive the hybrid damper's piston rod into a sinusoidal dynamic load with a 1-8 Hz frequency range. The number of balls was changed three times (5, 10, and 15) to examine this parameter effect on the FIHD's damping effect. In addition, a Finite Element Model (FEM) of the FIHD was developed using LS-Dyna explicit solver. The FEM of the FIHD simulated the elastoplastic collisions between the balls and the walls using a piecewise-linear plasticity material

model. Results were presented using Frequency Response Function (FRF) to show the damping effect in a set of force-independent results. The evaluated FRF of the two approaches (Experiment and FEM model) showed a noticeable reduction in amplitude at the system's natural frequency (2 Hz). In addition to the hybrid damper, this study also investigated a damper that belongs to the semi-active countermeasures known as Magnetorheological fluid (MRF) damper. MRF dampers' damping effect is controlled using a magnetic field produced by an excitation system. In an MRF damper, a smart fluid is used as the damper fluid instead of using the classic hydraulic oil. The excitation system components were designed and manufactured based on dimensions reported in a previous study. The excitation system's magnetic field (MF) density value was obtained both experimentally and numerically using Comsol FE software. The MF study aimed to address the parameters that affect the magnetic field density, and thus, the MRF damping effect. Eventually, a Computational Fluid Dynamic (CFD) Analysis is conducted on the MRF damper. The CFD analysis describes the fluid flow between the compression and rebound champers through the internal orifices. Averaged Navier-Stokes equations are solved by the SIMPLE method, and the RNG k-ε is used to model turbulence when the fluid passes through the orifice. The viscosity of the MRF was evaluated experimentally using a viscosity meter when applying different values of magnetic flux. The magnetic flux values were changed along with changing the excitation current values from 0 A to 5 A with a 1 A increment. Rebound and compression forces were observed from the static pressure contour plot. Based on the damping coefficients obtained from different viscosities values, the results showed that the damping values are exponentially increasing when increasing viscosity.

DEDICATION

To the soul of my father, Prof. Babikir Badri, may Allah Almighty bless him.

To my beloved mother who endured the arduous task of raising me and my brothers.

ACKNOWLEDGMENTS

First and foremost, all thanks to Allah (God) Almighty for giving me this wonderful opportunity.

I would like to express my deepest gratitude and appreciation to my supervisor Prof. Sadok Sassi who's insight and knowledge in Dynamics and Vibrations steered me through this research work. Without his appreciated guidance, patience, persistent help, and continuous support, I would not have been able to complete this research.

I would like to thank my Co-supervisor, Prof. Mohammed Hussein, for his enthusiastic guidance, ideas, effort, and countless hours he spent on my progress meetings, which helped me enhance the research work quality. In addition, I am greatly indebted to him for his all-out effort in securing funding for my first year of research. I must also thank my Co-supervisor, Dr. Jamil Renno, for the appreciated assistance he provided me with to overcome the research challenges easily, quickly, and intelligently.

Special thanks go to Prof. Elsadig Mahdi for his trust in giving me a great opportunity when he endorsed me to work with Prof. Mohammed Hussein.

I am grateful for the financial support from the College of Engineering at Qatar University (grant reference number: QUST-1-CENG-2020–15) and the grant sponsored by Qatar Rail with a grant reference number: QUEX-CENG- Rail 17/18. The financial support is gratefully acknowledged.

Special thanks go to all of my teaching staff, colleagues, and mates in my batch at Qatar University for their kind support.

Most importantly, my deepest appreciation and thanks go out to my beloved family, especially to my parents, who supported me unconditionally through thick and thin.

PUBLICATIONS

This work has already been disseminated through the following publications:

- Y. Badri, M. Hussein, S. Sassi, and J. Renno, “Investigation of the Effect of the Force-Frequency on the Behaviour of a New Viscous Damper for Railway Applications,” INTERNATIONAL CONFERENCE ON CIVIL INFRASTRUCTURE AND CONSTRUCTION 2020’’, pp. 666–671, 2020.
- Y. Badri, T. Syam, S. Sassi, M. Hussein, J. Renno, and S. Ghani, “Investigating the characteristics of a magnetorheological fluid damper through CFD modeling Investigating the characteristics of a magnetorheological fluid damper through CFD modeling,” 2021.
- Y. Badri, S. Sassi, M. Hussein, and J. Renno, “Experimental and numerical investigation of damping in a hybrid automotive damper combining viscous and multiple-impact mechanisms,” Journal of Vibration and Control, no. July, p. 107754632110381, 2021.
- Y. Badri, T. Syam, S. Sassi, M. Hussein, J. Renno, and S. Ghani, “Numerical Study on the Damping Characteristics of a Shock Absorber Valve Utilizing Different Velocities Through CFD Analysis,” 8th Int. Conf. Comput. Methods Struct. Dyn. Earthq. Eng. Methods Struct. Dyn. Earthq. Eng., pp. 4353–4362, 2021.

TABLE OF CONTENTS

LIST OF TABLES

LIST OF FIGURES

CHAPTER 1: INTRODUCTION

Noise and Vibration are socio-environmental problems that call for solutions by engineers. Controlling noise and vibration requires a good knowledge of the dynamic systems and their main components, i.e., mass, stiffness, and damping. In particular, dampers' main application prevents discomfort vibrations, outright structural failure, or reduces noise emission [1]. This thesis will mainly focus on investigating the combination of different types of dampers having viscous dampers as their fundamental part. In this chapter, the three types of vibration countermeasures will be discussed. In addition, the understudy dampers will be defined, and their related materials will be mentioned. Then, the study statement and its significance are given. At the end of the chapter, the thesis objectives and aims are presented, followed by the thesis content.

Generally, the vibration isolation countermeasures can be classified into three types: Passive, Active, and Semi-active. In the following sub-sections, Passive dampers and Semi-active dampers will be discussed.

1.1 Passive dampers

Passive damping can be defined as the inherent damping in the mechanical systems that can reduce vibrations energy over time. Most noise and vibration control systems are open loops, where the damping occurs naturally without sensing the amount of vibration [2]. In other words, passive damping controls the vibration due to previous predesigned considerations of the damper. Both industrials and scholars' practitioners conducted innovations and developments intensely on the different types of passive dampers such as; frictional dampers, viscoelastic dampers, viscous dampers, and particle impact dampers. Although each of those dampers has its unique characteristics,

their passive attitude in reducing and eliminating the vibration energy by converting it to another form of energy (mostly heat) is the same. A brief definition of the passive dampers used in this study will be discussed in the following sub-sections.

1.1.1 Viscous dampers

Usually, a viscous fluid damper (VFD) consists of a steel cylinder filled with silicone oil. An orifice plate (damper piston), connected to a rod attached to the vibrating structure, moves inside the cylinder and absorbs the disturbances. The movement of the rod forces the fluid to flow through the orifice plate between two chambers, resulting in pressure difference and generating the damping force. Viscous dampers were found to be sufficient for vibration energy dissipating and isolation for both mechanical and civil applications [3]–[6]. Many studies investigated experimentally and numerically the characteristics of viscous dampers in response to a different form of vibration excitation [7]–[9].

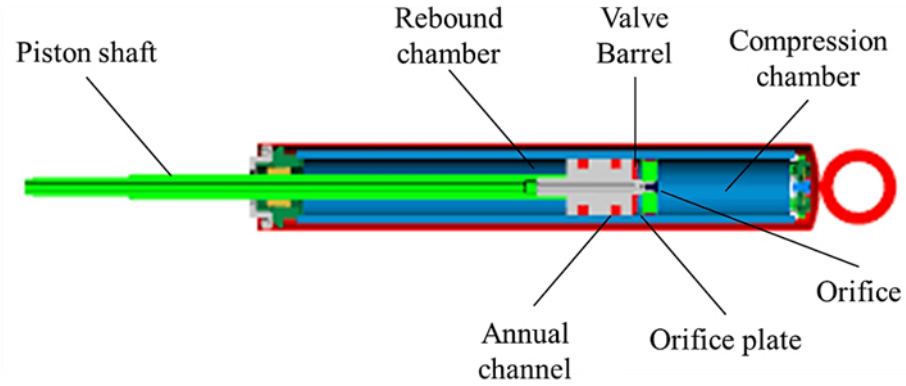

Figure 1. Viscous damper components [10].

Most vehicular shock absorbers are either twin-tube or mono-tube types with some variations on these themes, as shown in Fig. 1. A Twin-tube shock absorber consists of two nested cylindrical tubes. The inner tube is called a working or pressure tube, while

the outer tube is called a reservoir tube. At the lower bottom of the damper, valves (base valves) separate the fluid between the two tubes. Mono-tube dampers were considered a revolutionary advancement when invented by August Bilstein back in the 1950s [11]. As its name implies, the mono-tube shock absorber (single end piston damper), which is gas-pressurized, consists of only one tube [11]. When the piston moves, the single-piston end divides the oil reservoir into two chambers (rebound and compression). Because of the monotube single-cylinder, no base valves are needed to control the flow between the two chambers as in the Twin-tube.

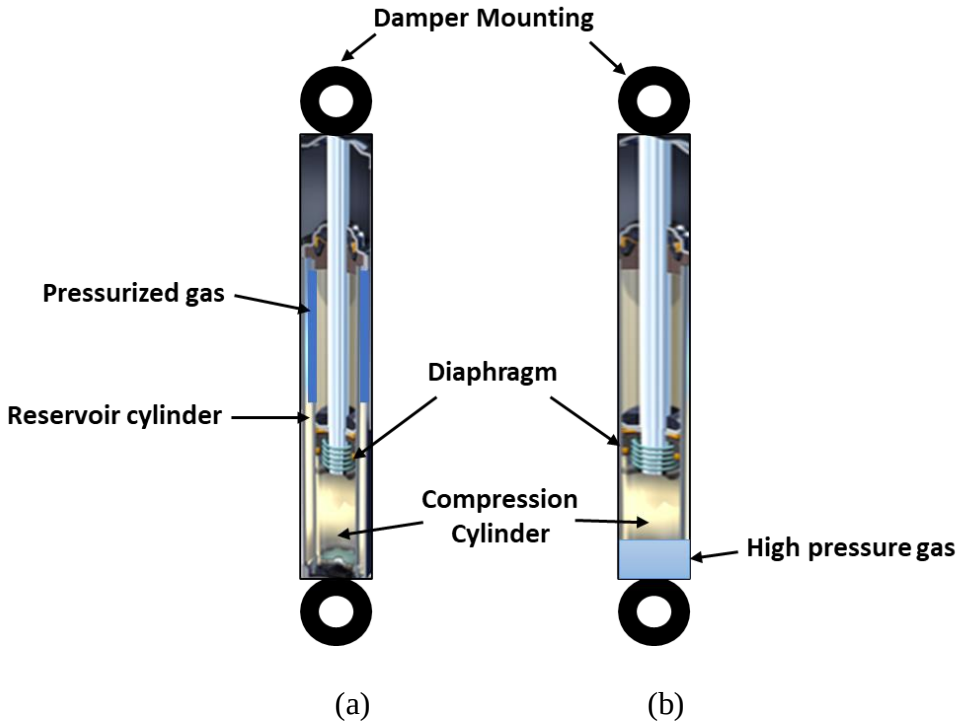

Figure 2. Viscous damper: (a) Twin-tube, (b) Mono-tube.

The differences in design features of the two types are clearly shown in Fig.2. These differences govern not only the flow pressure inside the cylinder but also the damping force, ride quality, and damper sensitivity are also affected. The main differences between the two types of viscous dampers are summarized and highlighted below in Table 1.

Table 1. Comparison between Twin-tube and Mono-tube viscous dampers [12]

Characteristics	Twin-tube	Mono-tube
valve mechanism	Multiple	Single
Cylinder circumference-Piston size	small	large
Gas pressure	low	High
Responsiveness	Moderate	Very sensitive
Aeration	Possible	Rarely
Ride quality	Smooth	stiffer
Damping force	Limited	Wide range
Production cost	low	High

Based on each damper criteria, the vehicles types using the damper in their suspension system will vary accordingly. Mono tube shocks are typically found in trucks, vans, or vehicles used for hauling, transportation, or any equipment driven in harsh road conditions. At the same time, twin-tube is mainly used for cars suspension systems and smaller sport utility vehicles (SUVs) [13].

1.1.2 Particle Impact Damper (PID)

Nowadays, particle-impact dampers (PID) are gaining more interest among researchers and engineers for the passive control of vibrations [14], [15]. The impact damper is a typical passive-control device that consists of freely moving masses constrained by two stops inside a container, mounted on the primary system [16]. When the moving masses impact the enclosing obstacles, momentum exchange occurs together with energy

dissipation [17]. Figure 3 depicts the most common types of impact dampers presented in the literature.

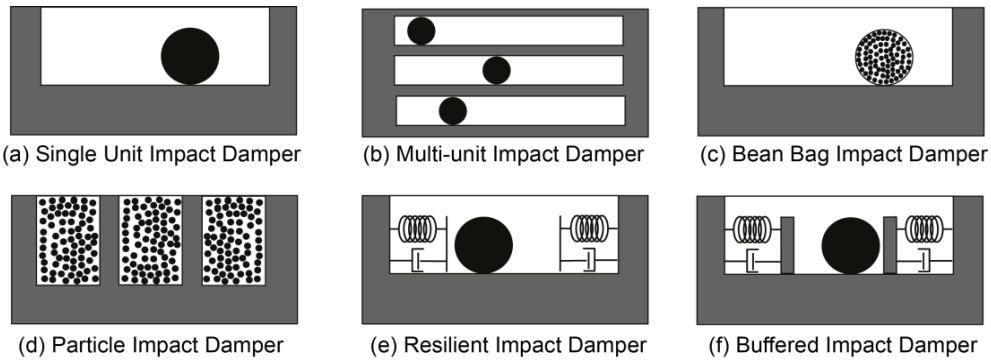

Figure 3. Types of Traditional Particle Dampers [16].

The impact damper has found wide use in the industry because it is simple, low-cost, robust, effective in vibration suppression over a wide range of accelerations and frequencies. In addition, PIDs could be installed in an application where harsh environmental conditions exist [18] [19]. Due to PIDs' previously mentioned favorable damping characteristics, several engineering fields considered using them in their applications. For example, PIDs were used in the aerospace field to reduce aircraft vibration [20], and wind turbines field to control the response of dynamic-wind load [21]. In addition, PIDs are excessively used in machinery fields such as; compressor machinery fields, metal-cutting machine tools, electro-mechanical systems [14].

The automotive field was also taking advantage of the developing technology of PIDs by applying them to their application. For example, PIDs were used in vehicles Inhibiting the steering wheel vibration steering control electric motor’s noise during idling [22]. As can be seen from these applications, PIDs can be used in devices and machines that vary in size, mass, operating conditions, and function. Consequently, the vibration energy's magnitude, frequency, and excitation profile will vary accordingly.

Therefore, no common PID will suit every application. However, it is not an easy job to classify PIDs according to their related application. Alternatively, Lu et al. [14] comprehended a review paper classifying PIDs according to the aspect of development applied in traditional PIDs (Fig.3). Those aspects mainly focused on three variants that distinguished each PID from the other. Therefore, configuration, material, and combination of damping technology were adopted as the three classification variants of the PIDs. Consequently, besides traditional PID, three categories of particle dampers were developed; Configuration Improved Type, Material Improved, Combination Type (Fig.4).

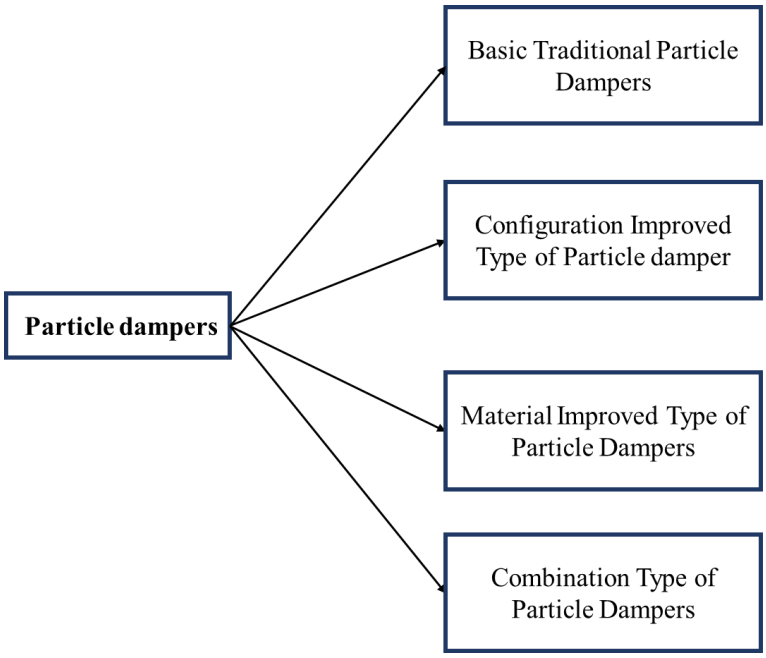

Figure 4. Categories of particle dampers.

In configuration improved type, modifications are made on the PID structure (e.g., particles and cavities) to enhance the vibration attenuation mechanism. On the other hand, the material-improved type employs a novel and traditional material for the box and the particles. Selecting the appropriate material will reduce noise and increase

plastic deformation, thus amplifying the vibration energy absorption. Although extensive research was conducted on the three categories, the combination improved type has the least number of investigations. Therefore, part of this study will be presenting a novel combination type of fluid-impact hybrid damper (FIHD) [23]. Moreover, designing, manufacturing, testing, and modeling will be presented in detail through the following chapters (3-5). Despite the PID's unpredicted behavior in damping, standard features should be provided to secure efficient damping. In the design phase of PID, many considerations should be known for a better structure damping effect. Firstly, the volume that includes the balls should be positioned to the maximum vibration amplitude location [15]. The rest of the design considerations could only be understood if the damping mechanism of the PID is first clarified. The damping mechanism of the PID mainly depends on two types of collisions; between particles to particles and between container walls and particles (Figure 5). Those two collision types govern the momentum exchange between the vibrating structure and the PID damper. The reduction of energy is a direct consequence of such a collision. Thorough investigation proved that the damping effect is mainly produced from particle to particle collisions. On the other hand, walls-particles collisions exchange movement between the vibrating structure and the PID with a low damping effect [15].

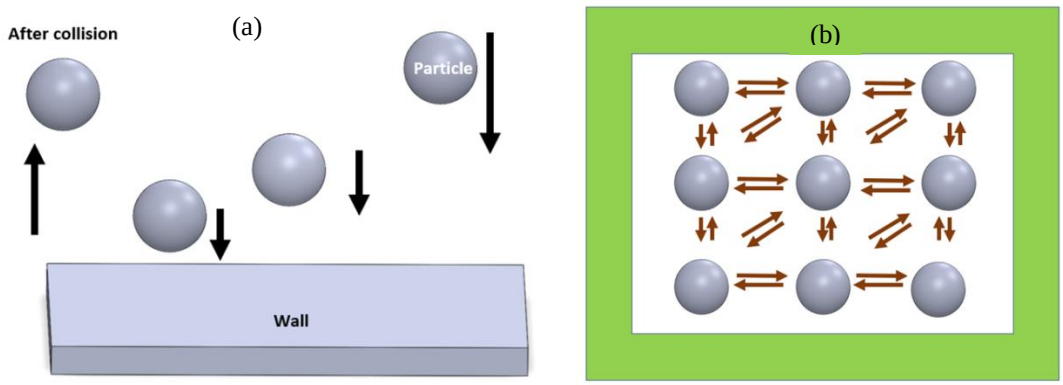

Figure 5. Damping mechanism of PID: (a) Wall-particles colloisions, (b)

Particles-particles colloisions.

Usually, there is no fixed rule to follow when designing the PID. Instead, it is a tradeoff relationship between two main factors; the coefficient of restitution (e) and the friction coefficient. Those two factors govern the damping functioning of the PID. Therefore, the design consideration of PID should be focusing on compromising the effect of the two coefficients. Generally, several concepts should be known before starting the design of PIDs [15]. Those concepts are addressed below.

- Increasing the sliding friction coefficient between the particles and the walls will decrease the damping effect of the PID. This can easily be explained by the correspondent decreasing in the (e) value and hence the momentum exchange.
- For small containers, the (e) value should be low to increase the damping effect, and for big containers, the design should maintain a high value of (e) to increase the damping.
- Using soft material or coating the internal surface of the container is important to reduce the noise and maintain a coefficient of friction at a value where many collisions could occur.
- The PID should be located where the maximum amplitude of vibration occurs.

1.2 Semi-active dampers

Semi-active dampers are mechanical devices that can give a variable damping value when connecting to a small power source [24]. Therefore, the variable damping value will provide a steady-state operation regardless of the continuous changes in the disturbance and vibrations coming from the surrounding environment. Semi-active and

fully active dampers overcome the possible range of damping characteristics provided by the conventional passive dampers. The semi-active control technology is implemented in different devices, and typical semi-active devices include Servo/Solenoid valve, Magnetorheological (MR), Electrorheological (ER), and Electromagnetic dampers.

1.2.1 Magnetorheological fluid (MRF)

The origins of the MRF belong to smart material, which changes its rheological behavior along with the applied magnetic flux [25]. Although MRF is much similar to Ferrofluid (FF) in particles aggregation when magnetically controlled, the magnetized particles size of the two fluids is different. Moreover, the FF particles size is nanometer range (3-15 nm), while you can find that MRF particles are above one micrometer (1-20 μm) [26]. The micron particles of MRF are almost stationary, and their Brownian motion is negligible. On the other hand, FF particles perform intense thermal movement due to their permanent dipole moment. Therefore, the Agglomerate formation of the MRF particles is essential due to the particles' stationarity when the fluid is magnetically induced [26]. The MRF fluid's previous properties significantly increase the fluid viscosity up to 10^3 times when induced with a magnetic field. In addition, MR fluid could give similar damping of ordinary oil (Newtonian fluids) with moderate viscosity value in the absence of excitation. The micron metallic particle forms a column structure perpendicular to the flux line (Figure 6). The small particle's structure will have yield stress known as field-dependent yield stress. Field-dependent yield stress value will increase as the magnetic field increases, and at any stress point below this value, the fluid will behave as a viscoelastic material.

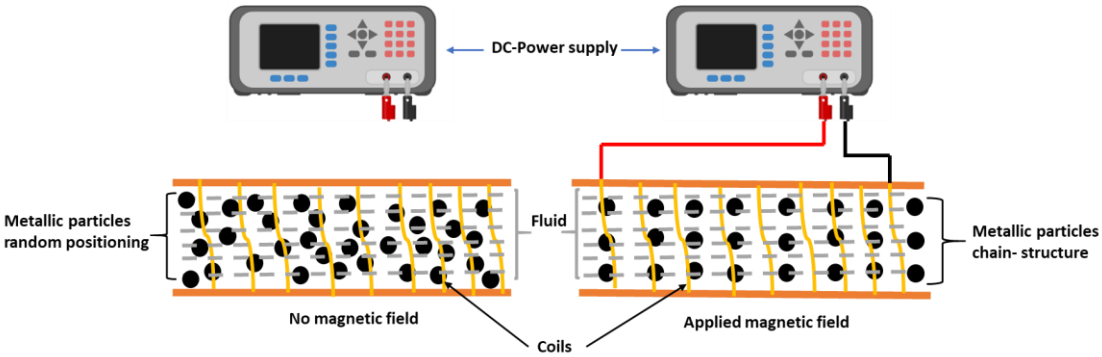

Figure 6. MRF particles arrangement, before and after applying a magnetic field.

MR fluids could be classified depending on the fluid yield stress value and the fluid carrier type. Nowadays, the LORD Corporation company manufactures most of the MR fluids types. Therefore, instead of mentioning each type of characteristics table, Lord corporation product code will be satisfactory for MRF characteristics identification. Based on the fluid carrier, Lord corporation manufactured three types of MRF; oil-based (MRF-132LD), water-based MRF-240BS, and silicone oil-based (MRF-336AG) [27]. Moreover, when considering the value of the fluid yield stress, the MRF will be divided into three groups; low yield stress MRF-122-2ED, medium yield stress MRF-132-DG, and high yield stress MRF140 CG [28]. Although all the previous types are hydrocarbon-based, it was found that MRF with high yield stress tends to consume less power in brake applications [28].

On the other hand, all devices that use MR fluid can be categorized into three operating modes: (a) valve mode, (b) direct shear mode, (c) squeeze mode. Figure 7 shows the schematic of the structural configuration for each mode. Although all the modes may have induced a magnetic field perpendicular to the plate's planes, the actuating part is changed between the fluid and the plates. For example, MR fluid flows in valve mode due to a pressure gradient between two fixed plates. This mode can be found in applications that include hydraulic controls such as; shock absorbers, servo valves.

In contrast, the shear mode includes one plate, which moves relatively while the other plate remains stationary. Clutches, brakes, and braking devices are the devices that use such a mode with MRF. Lastly, squeeze mode induces the flow of MR fluid by applying forces on the two plates in a direction perpendicular to their planes. Due to the small movement of the plates, the Squeeze mode is usually adopted in small-amplitude vibration and impact dampers [29] [30] [31].

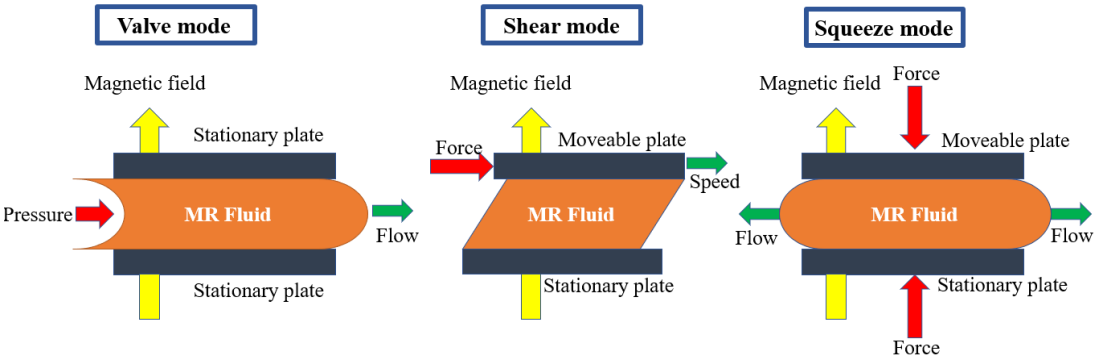

Figure 7. MRF operating modes (reproduced from ([32]).

As shown previously, each one of the three operating modes is implemented in applications where small/high amplitude/frequency is needed. One of the first applications that used valve mode was the suspension element of vehicles [33]. Designing such a damper usually starts by replacing the damper's classic hydraulic oil with an MRF damper and integrating a magnetic coil integrated into the piston of the damper to generate a magnetic field. The induced magnetic field will regulate the MRF flow resistance inside the damper cylinder (Figure 8).

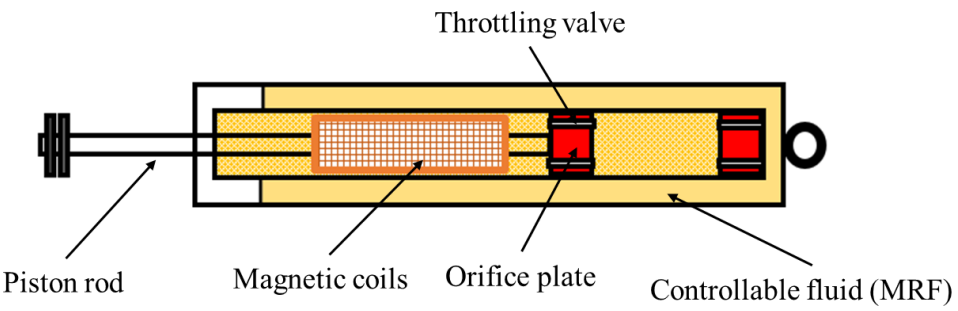

Figure 8. Schematic of MRF twin-tube damper.

MRF damper presents a state-of-art semi-active vibration countermeasure, which supplies different damping values in response to an applied magnetic field. MRF dampers can be controlled to provide a damping effect suitable for various vibrations' frequencies and amplitudes with maximum working efficiency. MRF dampers are mainly used in vehicles suspension systems (Spring-Damper) to overcome the limitations of passive viscous dampers. The axle transfers the movement to the vehicle body when the car spring oscillates due to road imperfection. Therefore, the passenger comfort will be disturbed unless the car suspension system is functioning efficiently. The efficient (optimal) damping required a compromise between safer damping (hard) and comfort damping (soft), which depends on the damper selection as well as it depends on the road profile [24]. The continuous changing in the damping between what is safer and what is required for ride comfort can only be achieved by semi-active damping.

1.3 Problem Statement and its Significance

Developing or improving vibration isolation countermeasures have been gaining scholars' interest since the development of the first tuned mass damper in 1909. The continuous urban expansion and development processes in the transportation sector are

associated with human discomfort resulting from increased noise and vibration levels. In addition to the human discomfort, excessive vibrations also result in outright structural failures of buildings and the damaging of different industrial machines. Historically, vibrations induced from dynamic loads were reduced by using passive dampers, which develop a predetermined damping amount. In contrast, those dampers cannot overcome a particular limitation associated with their damping amount and its variation in response to the dynamic loads.

Moreover, improving the damping performance of passive dampers in certain conditions required adopting one of the following approaches; controlling the damping by modification or tuning of a few internal parameters or integrating extra control technology. Till this moment, the approach based on combining and integrating two damping technologies is the least investigated approach of passive damping. Therefore, this study will explore the possibility of combining the viscous damping and the particle impact damping in the same device and analyze its damping behavior. The second part of the study will present smart rheological material as a damper's fluid. The semi-active MRF damper's damping behavior was extensively investigated analytically by developing equations based on statistical analysis to experimental results. In contrast, analyzing the damping effect of MRF dampers needs more investigation on the fluid flow perspective. Therefore, a computational fluid dynamic analysis will be adopted to create numerical models for the passive and MRF viscous dampers. Meanwhile, the previous experimental work that has been conducted on the MRF dampers mainly focuses on testing setup. Alternatively, a small number of studies overlooked the parameters that may amplify the MRF correspondent magnetic field. However, rather than building an MRF damper experimental setup, this study will address new design features to enhance the MRF's excitation system efficiency and thus its damping effect.

1.4 Research objectives

This research aims to introduce a novel type of hybrid passive dampers (FIHD) and enhance the efficiency of semi-active (MRF) dampers. The behavior and characteristics will be studied both experimentally and numerically.

The main aim of the work will be achieved through the following objectives:

A. Experimental work

- Design and manufacture the hybrid damper (FIHD).
- Design and manufacture a testing setup of small amplitude and small frequency excitation using a shaker.
- Examine the damping effect of the manufactured hybrid damper using the developed testing apparatus.
- Design and manufacture the excitation system of Magnetorheological Fluid (MRF) damper.
- Test the magnetic field density of the damper's excitation system to investigate the parameters that affect the magnetic field intensity and, thus, the magnetorheological fluid's damping effect.

B. Numerical work

- Develop a finite element model that simulates the FIHD behavior.
- Analyze the magnetic field effect through finite element modeling for the semi-active MRF damper.
- Investigate the damping coefficient of the MRF damper through a CFD analysis of the fluid flow inside the damper.

1.5 Research Methodology

Similar to any scientific inquiry, the actual work has started by conducting a thorough investigation of the literature to explore the previous experimental and numerical studies that focused on Hybrid passive and MRF dampers. This works mainly aims to fill the literature gap regarding hybrid passive dampers countermeasure. Therefore, a hybrid damper that combines viscous and particle impact damping effects was designed, manufactured, tested, and modeled numerically. In addition, one more MRF damper was designed and manufactured to replicate an MRF damper developed in a previous study. In contrast, the MRF damper was analyzed numerically to explore design features that may enhance its damping effect. The first damper (FIHD) was investigated experimentally using a shaker setup. The FIHD testing setup aims to examine the dampers' characteristics independently from their surrounding structures. The excitation was in Sine-waveform, and the response was measured using a set of force-sensor and an accelerometer. The MRF experimental findings were obtained from a previous experimental study of a falling mass. Secondly, a numerical model was developed to simulate the behavior of each damper, which replicates the experimental setup. The numerical software packages basically have two solving methods; finite element modeling (FEM) and finite volume modeling (FVM). FEM was developed using LS-Dyna to examine the collisions of the ball of the PID attached to the HFID in increasing the damping effect of a conventional VFD. A Computational Fluid Dynamics (CFD) model was developed to study the flow inside the VFD flow domain and its developed forces that produce the damping forces. The CFD model was then upgraded to fit the use of the MRF damper by setting a variable parameter (viscosity) with the applied current. The results obtained from the experiments and the simulations for both dampers were compared to validate and examine the model accuracy.

1.6 Thesis Content

Chapter 1: Introduction: This chapter introduces the passive and semi-active vibration countermeasures fundamentals, along with the damper types included in the study. Research objective and thesis organization are also included in the first chapter.

Chapter 2: Literature review: This chapter reviews the experimental setups and modeling of each damper developed and redesigned in this work.

Chapter 3: Numerical Modeling of the special dampers: This chapter shows the numerical models developed to understand the behavior of Hybrid-fluid impact dampers and MRF. ANSYS Fluent-CFD tool will be used to simulate the flow domain inside the viscous damper, while LS-Dyna will simulate the balls' collision in the HFID. Lastly, COMSOL-AC/DC magnetic field package will be used for the magnetic field analysis

Chapter 4: Experimental Developments and Prototype Setup of the dampers: This chapter illustrates the manufacturing of the FIHD's essential components and corresponding setup. In addition, the MRF excitation system's components and drawings are presented.

Chapter 5: Conclusions and future works: It will summarize the main findings and conclusions in this thesis and highlight some recommendations for future works.

Chapter 2: Literature Review

The relevant studies reported in this chapter are reviewed to establish a framework for holding and generating new ideas that will help improve the damping effect of each damper.

2.1 Experimental investigation of dampers

Dampers' experimental setups are designed and used to simulate the dynamics of dampers in real case scenarios and to evaluate their damping characteristics. In addition, experimental investigation presents a reliable way to validate dampers' numerical models. Although numerical models could be verified analytically, analytical models suffer from limitations in showing nonlinearity and hysteresis damping behavior. Experimental tests overcome this limitation and strengthen the approach of discovering new models depending on the interpolation of experimental results. Generally, each setup consists of three main parts: damper, actuator, and sensor. The actuator can excite the damper with different forces (oscillating, impact, impulse, etc.). The vibration energy is then transferred to the damper through means of couplings. Eventually, to record the damper response, sensors measure many parameters such as displacement (LVDT), force, and acceleration (Accelerometer). However, these testing apparatus sensors' signals will not be acquired unless they are coupled to Data Acquisition System (DAQ) with appropriate sampling frequency. A brief review of scholars' experimental investigations associated with this study dampers will be discussed in the following sub-sections.

2.1.1 Experimental investigation of viscous dampers

Laboratory tests of vehicles' viscous dampers are preferable to road driving sessions because they are cheaper and may be performed more rapidly [34]. Researchers usually require a test setup similar to the axial fatigue machine to conduct an experimental investigation for the VFD. Usually, a viscous damper's test apparatus consists of a hydraulic actuator applying reciprocal motion with predetermined force magnitudes. These actuators should be equipped with a speed controller, force cells, and displacement sensors to measure the damping of the viscous dampers. The moving part of the actuator must be connected to the piston rod of the viscous damper from one side. On the other side, the damper is connected to fixed support through a force sensor. To measure the dynamic displacement of the piston rod, an LVDT is attached to the damper body, as shown in Figure 9. The LVDT will give a continuous displacement reading for the damper rod during its two strokes; compression and rebound.

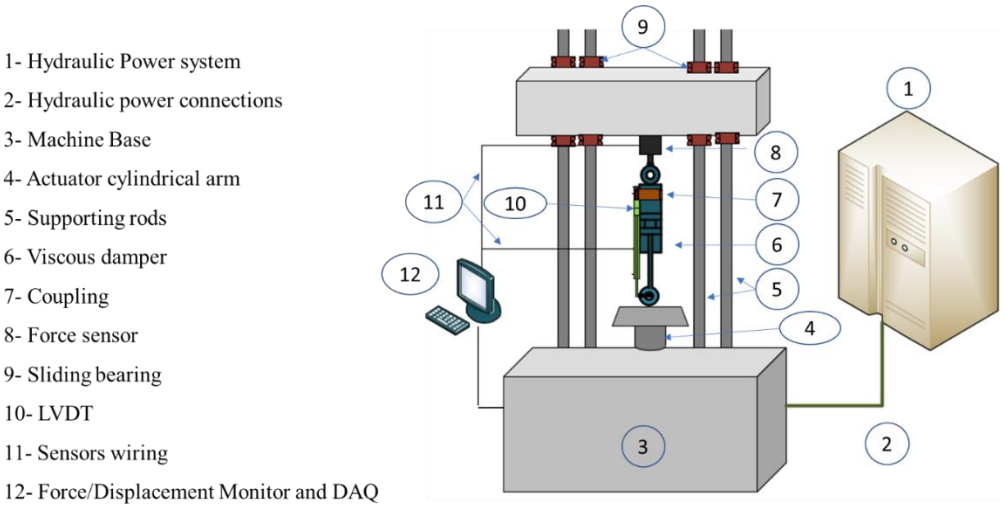

Figure 9. Viscous damper testing apparatus

To obtain an accurate reading of the damper's dynamic performance, the user could easily combine the two readings of time and displacement of the rod to get the velocity and use the load cell to make a continuous reading of the force. Consequently, the force-displacement and force-velocity graphs, which characterize the damping behavior, could be easily obtained [17].

Considerable studies were carried out using different experimental setups and procedures to better understand the viscous damper's behavior. For example, Guan et al. developed a twin-tube VFD test apparatus [35] that consists of a motor, a load rack, a static frame, and a crank. The crank transforms the rotation movement into a reciprocating displacement. The loading rack is connected to the crank through a linkage and then attached to the damper. A load cell is located at the bottom of the bench to record the damping force using a data acquisition (DAQ) system. Another experimental setup was introduced in [36] to test magnetorheological dampers. The shaking table was composed of a hammer, a basement, suspension springs, and a support structure. The impact load generated by the hummer impacts excites the basement, and the response of the MR damper is consequently measured. Instead of using a hydraulic actuator, Badri et al. [37] developed a small amplitude VFD setup using a shaker and a dual accelerometer-force sensor. Their experimental setup was designed to drive the VFD's rod into harmonic oscillations with small displacement amplitudes and excitation frequencies.

The shaker stinger was connected through couplings and a dual force-acceleration sensor to the damper rod. Both coupling and sensors were moving together to transfer the periodic motion to the rod. The state-of-art small-amplitude shaker setup allows linearization of fluid viscous damper characteristics. The design, manufacturing, and contribution of their novel shaker setup and the experiment results are discussed in

Chapter 4. In contrast to periodic loads setups, Narkhede and Sinha [38] developed a non-periodic shock testing machine for viscous dampers (Figure 10). The testing machine generates a half-cycle sine pulse using a corset, steel plate, and buffered mass. After releasing the corset from a suitable height, it will strike the buffered mass, which is linked to the damper rod. Two accelerometers are attached to the piston-end and the cylinder-end. Also, an LVDT is connected between the buffer mass and damper piston to record the damper's acceleration and displacement time responses [38].

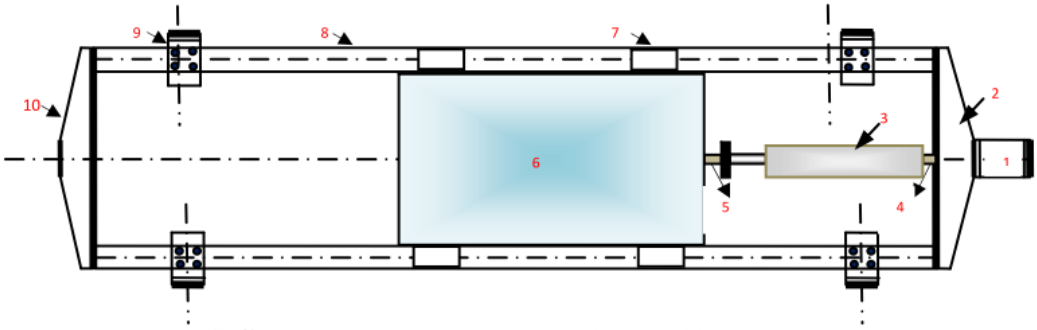

1. Striker
2. Corset Front
3. Fluid Viscous Damper
4. Bracket Damper Cylinder End
5. Bracket Damper Piston End
6. Mass 10 Tonne
7. Rollers for Sliding Mass
8. Corset Bed
9. Pendulum Swings
10. Corset Rear

Figure 10. Half sin pulse experimental setup [38]

To sum up, the various devices and sensors used in testing viscous dampers, Table 2 addresses most of their measured parameters.

Table 2. Summary of the testing devices of Viscous Damper from the literature review

Device	Measuring Parameters	Frequency Range
Axial fatigue machine	Force, Displacement, Acceleration.	0-10 Hz

Device	Measuring Parameters	Frequency Range
Damper testing setup	Force, Displacement, Acceleration	-
Load Cell	Force	-
Position Sensor	Displacement	-
Accelerometers	Acceleration	-

2.1.2 Experimental setup of PIDs

In particle-impact-based dampers, an experimental investigation is usually used for two purposes; validating a numerical model or/and parameters identification. Such parameters could easily be obtained by a statistical process of the force, acceleration, velocity, and displacement experimental results. Usually, the testing setup consists of a structure, a PID, an exciter, and a DAQ system to record the structure's acceleration time response (Figure 11). The particles' damping contribution is gaged by measuring the reduction in the response peak amplitude, the decay time, and the change of the structure’s natural frequency.

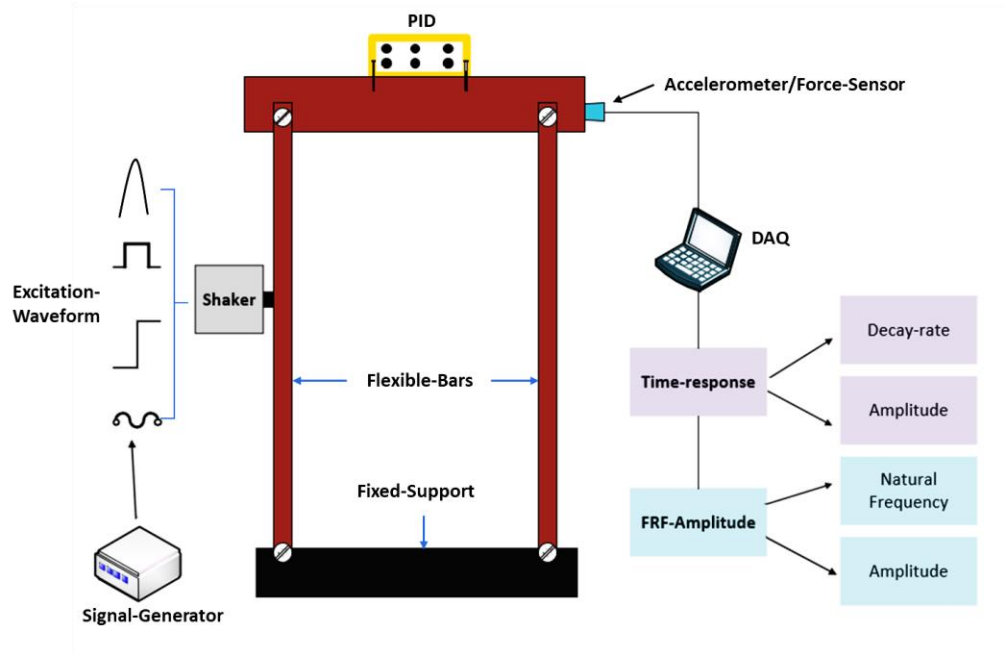

Figure 11. PID typical experimental setup structure.

In summary, the various devices and sensors used in testing the damping behavior of PIDs are depicted in Table 3 with their measured parameters.

Table 3. Summary of the testing devices of PID experimental setups from the literature review.

Device	**Measured Parameter**	**Frequency Range**
Shaker	-	-
Impact Hammer	Impact Load	0-10 kHz
Mass	Impact Load	-
Accelerometer	Acceleration-Velocity-Displacement	10mV/U-100mV/U
Position Sensor	Linear displacement	-

The test is repeated 3 to 5 times for each experimental investigation to reduce the statistical errors and ensure good experimental repeatability. In addition, the position where the structure or the PID is excited should be fixed and consistent during every test [15]. Numerous experimental studies were carried out to shed light on PID's behavior. Masmoudi et al. [39] investigated the energy dissipation of a PID, partially filled with particles and attached to a shaker. The shaker provided a sinusoidal load with 46 to 166 Hz and an acceleration amplitude from 0 to 1g. Their experimental investigation showed that the damping value is independent of the particle's material and quantity but strongly dependent on the particles' mass and the excitation magnitude. Li and Darby [21, 22] conducted two experimental studies describing a single ball PID's behavior attached to single and multiple degrees of freedom (SDOF, MDOF) structures. Their setup consists of a shaker moving a linear bearing attached to a frame. The response was recorded using LVDT and accelerometers. The SDOF system was designed as a single-story structure, while the MDOF system has three stories. The amplitude of the SDOF system decreased when the size and mass of the balls increased. The same result did not apply to the MDOF case. In other words, the trend of amplitude reduction of the PID does not behave the same through all modes. Moreover, all the experimental research works agree that PIDs are more efficient for low amplitude high-frequency vibration reduction applications [14]. In 2015, Gharib and Karkoub investigated the “linear particle chain impact damper” case [41], where particles were driven in straight-line motion In such experiment, the harmonic excitation shaker was replaced by a pulse excitation where an impacting mass hits the structure support.

Table 4. Summary of the Applications and Experimental setups from the literature review.

Damper Type	Experimental Setup	Measured Factor	Application	Ref
PID	Particles bed attached to a supported beam. The response is measured remotely by a laser vibrometer.	Velocity time response.	Dissipate the structure elastic energy	[19]
Viscous damper	None (Analytical Modeling)	Force and displacement of the piston rod.	Vehicle dynamics	[42]
PID	Multi-story structure with three accelerometers attached to each story. PID is located between two load cells.	Time response acceleration envelope curve + Power spectrum density	Earthquake Excitations	[43]
PID	Single degree of freedom structure having one accelerometer to measure structural response. The PID ball is located between two load cells.	Displacement time response	Not specified	[1]

Damper Type	Experimental Setup	Measured Factor	Application	Ref
PID	Linear balls chain attached to the rectangular frame structure with impact mass, position sensor, and DAQ.	Displacement time response + Frequency response function.	Small vibration magnitude with small frequency	[44]
Rubber supports	Railway tracks prototype with support equally spaced, having an accelerometer attached to the track end.	Response decay	Railway application	[45]
MRF damper	Viscous damper attached to a sliding structure and impact load of a falling mass.	The damping coefficient of a linear force-velocity model.	Power consumption is reduced.	[46]
PID linear particle chain	Balls with two different dimensions arranged in a line, each ball hung like a pendulum.	Acceleration time response	Not specified	[41]
PID	Balls with different mass ratios placed inside a box with LVDT and force cells	Acceleration time response	Not specified	[16]

2.1.3 MRF experimental investigation

Based on the type and number of parameters needed to be extracted from the damper, the experimental setup is designed. As discussed before, MRF dampers can operate in different modes and result in different types which function differently. However, the scope of the study is to investigate the classical viscous-based MRF damper. Therefore, almost the same experimental apparatus machines used in passive viscous dampers will be applied in analyzing the MRF dampers. The experimental work of the MRF damper includes designing the magnetic excitation system and building the testing apparatus. In the design phase of the excitation system, coils should be wounded around the metallic core to generate the magnetic field in a direction perpendicular to MRF flow inside the damper cylinder. The number of copper coils turns, wire dimension, current values, and excitation type (AC-DC) still investigate able parameters in the field of the MRF dampers. Moreover, no common relationship is yet developed to connect all the excitation system design parameters with the obtained damping values.

All the MRF damper's experimental studies were conducted whether to obtain models parameters statistically or to validate developed models of the MRF dampers. For example, Dong Guan et al. [35] designed a test bench for their twin-tube shock absorber investigation consisting of a motor, a load rack, a static frame, and a 25-mm radius crank. The crank function was to transform the motor rotational movement into a linear reciprocating motion. The loading rack is connected to the crank through a linkage and then attached to the damper. Meanwhile, a force cell was located at the bottom of the bench to record the damping force using a DAQ system. Their objective was to obtain Force-velocity and Force-displacement curves, then compare them to the numerical model results. They found that the damping force decreases at the end of the compression stroke. However, the testing mechanism was governed by the crank slider

(Scotch Yoke). In addition to the crank slider movement, T. M. Gurubasavaraju et al. [47] used a mechanical exciter in their MRF damper experimental setup. The mechanical exciter consists of a variable speed motor with a cam system. It provides the needed dynamic load up to 500N with 0.1-3Hz. An LVDT sensor and a force cell were mounted to the damper to measure the damper performance. The required excitation current was provided by a DC power supply that was connected to the MRF electromagnetic system coils. Subsequently, all the sensors were connected to a DAQ device that records the Displacement-Force data.

On the other hand, some scholars use specially made devices known as Damper Test System (DTS) [48] and [49]. In their investigations, [49] used an MTS-835, which is a damper testing system that can go up to 15kN with a maximum stroke length of 100mm. Moreover, their testing machine could provide a wide range of excitation waveforms (Sine, Ramp, Square, Sine-on-sine, Sine sweep, etc.). The variety of excitations forms gave advantages over the motor-based experimental setup. Continuing with the MRF damper study, the damper was excited with harmonic oscillations of increasing frequencies (frequency sweep). In addition, another test was conducted while increasing the load amplitudes for a fixed frequency (amplitude sweep). In all the tests, the excitation current values were increased by a constant step of 1A, from 1A to 6A. The used damper system helped them find the damping force behavior for a wide range of frequencies and amplitudes.

2.2 Numerical investigation of dampers

In the absence of exact solutions for complex and nonlinear problems, we usually require a numerical answer. The current growth in computing power strengthens numerical simulation software used to solve physical differential equations.

Furthermore, to seek a solution for a physical phenomenon, simulation software mainly adopts one of the three techniques: Finite Element, Finite volume, or Finite Difference. In the previous literature review, several numerical simulations of VFD, MRF dampers, and PIDs were encountered, using at least one of the previous methods. As a result, numerical models gave a good prediction of their damping, nonlinear behavior, and performance in absorbing the vibration energy.

2.2.1 Viscous damper numerical modeling

Many studies investigated experimentally and numerically the characteristics of viscous dampers in response to various forms of vibration excitation [7]–[9]. Analytically, two main models could be used to describe the VFD force-velocity relation: linear and generalized models. In a linear model, the damping force (F) is directly proportional to the velocity ($\dot{y}$) [9]:

$$F = C\,\dot{y} \qquad (1)$$

In the generalized model, the nonlinear behavior is defined by a fractional exponential coefficient (α), and the damping force is set as follows:

$$F = C\,(\dot{y})^{\alpha} \qquad (2)$$

The exponent values range from 0-1, and the VFD behaves fully linear when α=1 [6]. The Finite element (FE) software packages use a built-in element category to characterize both the viscous damper's linear and nonlinear behaviors. Bai [50] developed a finite element model (FEM) of a simply-supported beam using ANSYS. The authors investigated the beam response when using various damping elements (COMBIN14, COMBIN37) to control the vibration. The FEM time response results showed that the COMBIN14 element could simulate a linear viscous damper, while the

COMBIN37 element is more suitable for simulating the nonlinear viscous damper cases. Another numerical model was presented by Jugulkar et al. [3] to characterize the viscous damper using CFD Fluent Flow. They simulated the damper fluid flow through the orifices in rebound and compression chambers. Their model indicated a decrease in the damping value as the number of orifice holes increased. On the other hand, the damping is linearly proportional to velocity change and starts acting nonlinearly after a specific velocity value.

2.2.2 PID numerical modeling

To obtain the response of a structure equipped with PID, scholars use both analytical and numerical approaches. However, analytical models are rare to be used and limited to a few cases. The classical PID's damping behavior could be described using a rheological model [51], similar to the mass-spring-damper Maxwell model. Olędzki et al. [52] developed a model based on rheological models to characterize the moveable plastic inserts' collisions with a container with a non-metallic layer. Moreover, the material plastic deformation, coming from the plastic inserts' collisions, was considered the source of PID damping. The mathematical expression developed by Olędzki et al. is given in equation (3) below.

$$m\ddot{x} + ax|x^b| + c\dot{x}|\dot{x}^d| = 0 \qquad (3)$$

where m is the mass of the moving insert, and x is its displacement. The values of the parameters a, b, c, and d can be found by calibrating the experimental results based on the initial velocity of the moving parts and their coefficient of restitution.

In addition, most of the models developed in the analytical approach need some

numerical methods to be solved. Those Numerical methods are used because of the nonlinear PID's behavior, force-displacement, and force-velocity results curves. Basically, the contact problem between collided particles could be solved by referring it to Hertzian contact theory. Furthermore, Hertzian contact theory is driven from the elasticity theory equations [53] to calculate the forces, stresses, and displacement of collided bodies at the contact point [54]. Hertz's contact theory and its extensions are used inside a numerical method to define collided PID's particles behavior [15]. For example, Aryaei et al. [55] reviewed Hertz's theory's use in finding the coefficient of restitution (COR) between two collided bodies. They built a numerical model and experimental apparatus to retrieve the COR of falling mass on a squared plate. The study focused on finding the effect of ball size, material, and contact area on the energy loss or the COR value. The LS-Dyna FE explicit solver was used to conduct the dynamic analysis of the falling ball. Besides the FE method, the Discrete Element Method (DEM) was also used in modeling the PIDs [56]. DEM reduces the MDOF system to an equivalent system of masses, springs, and dampers. The DEM element motion is governed by local contact law and Newton equations, assuming interaction with neighbors at a small time-step [14]. Recently, a FEM and DEM coupling approach was implemented by scholars [57]. The DEM describes the interaction between particles and walls, while the FEM simulates the structure's response [57].

2.2.3 Characterization of MRF dampers

The MRF rheological characteristics are rapidly and reversely changed with the applied magnetic field [58]. The change in rheological characteristics results in adjustable damping force. MRF dampers have been widely investigated with the variable damping force where vibration controlling, reduction, and isolation are required.

2.2.3.1 MRF analytical models

MR damping force was modeled using different analytical models to describe its nonlinear and hysteretic dynamic behavior [27]. Viscoelastic material models are usually used to characterize the MRF fluid behavior. The viscoelastic material combines both the elastic properties (described by Hooke's law) and the viscous properties (described by Newton's law) [59]. Bingham model is the simplest model describing the behavior of the MR viscoelastic material. Bingham's model uses a Quasi-static approach to study the non-newtonian yield stress fluids flow of the MRF [60] [61]. In contrast, the Bingham model does not present the true non-linear hysteretic force-velocity relationship. Although the Bingham model limitation in characterizing nonlinearity, It is very useful in the damper designing phase and performance prediction [27].

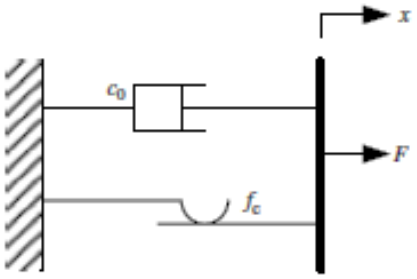

Figure 12. Schematic representation of Bingham damper model

Figure (12) shows a schematic of the Bingham damping force model where the damping force consists of passive and active components. The analytical equation expressing the Bingham model damping force is given in Eq (4).

$$F = f_c \, sgn(\dot{x}) + c_0 \dot{x} + f_0 \qquad (4)$$

where f_c is the friction force due to yield stress, c_0 is the damping coefficient, and f_0 is the force stored by the accumulator. Due to the previously mentioned limitation of the Bingham model, it is not preferable to use it in dynamic applications where nonlinearity

is observed. In contrast, many other models are developed to predict the nonlinearity/hysteresis behavior of the MRF damping force. These models are reviewed comprehensively in Table 1 of the study [62], including the mathematical expression for the damping forces. Each model has it is own parameters (as in eq.4); parameters values could be estimated by conducting statistical analysis fitting techniques for the experimental results of the MRF damper [63]. Although analytical models that describe the MRF damper behavior are out of scope for this study, one of the experimental investigation's objectives is to estimate those model parameters.

2.2.3.2 Viscous and MRF dampers CFD modeling

As mentioned before, MRF dampers are passive viscous dampers with integrated magnetic field sources and controllable damping fluid. Therefore, a numerical model characterizing the MRF damper will be built on the viscous damper model while involving the effect of the controllable fluid. Viscous dampers could be characterized by only simulating the flow inside the damper chamber using Computational Fluid Dynamics (CFD) analysis. In contrast, two physics are usually included in developing MRF dampers numerical models: fluid flow inside the damper piston and magnetic field analysis. Due to the continuous development of numerical packages of FE modeling, solving complex geophysical problems, which include the interconnection of fields, became possible. Numerous studies were conducted to investigate both passive MRF viscous dampers characteristics through developing computational fluid dynamic models. For example, using CFD analysis, Xiaolei Jiao et al. [66] characterized micro-vibration fluid viscous damper nonlinear behavior. Their study introduced passive viscous dampers used to isolate the high-frequency micro-vibration

produced from gyroscope satellites. In their CFD analysis, they obtained the damping coefficient and the damping ratio through two approaches; analytical and numerical. In the analytical approach, resistive forces acting on the pipe were calculated while assuming the fluid flow through the orifice was laminar. On the other hand, the numerical CFD model was developed using the ADINA software package. The model results concluded a relationship between the nonlinear damping force with the damper orifice dimensions, fluid viscosity, excitation amplitude, and frequency. Moreover, Lalitkumar et al. [3] used Ansys Fluent to develop a CFD model characterizing the viscous damper behavior. The damper fluid flow through its orifice's openings was simulated using K-epsilon (k-ε) turbulence model. (k-ε) is well known two equations model describing the mechanism that affects the turbulence kinetic energy [64]. However, their investigation focuses mainly on the effect of openings number on the viscous damper damping forces. It was clearly observed, increasing the number of outlets will decrease the damping force accordingly. As mentioned before, simulating the MRF viscous sums up the modeling of fluid flow and the excitation system's magnetic field. Usually, non-Newtonian MR fluid is modeled as Bingham fluid having magnetic-field-dependent yield stress [65], [66]. Engin Gedik et al. [70] studied a 2D MR fluid flow between parallel plates through CFD analysis based on Bingham fluid assumption. The CFD model was conducted using Ansys 14 Fluent MHD module, which uses momentum equations along with magnetic induction equations. Subsequently, a parametric study was conducted based on the effect of the magnetic field value on the fluid flow speed. However, it was found that the MR valve operating mode tends to decrease the fluid velocity as the magnetic field density increases.

In contrast, the shear mode was used to model the MRF twin-tube damper by Gurubasavaraju et al. [47]. Their numerical investigation delivered a 3D coupled CFD-

FE model. The FE-model is concerned with the simulation of the coils' magnetic field regarding the applied current. Then, the field-dependent yield stress) is obtained directly through the Bingham fluid model equation. The field-dependent yield stress is then adopted by the non-Newtonian fluid region defined in the CFD model. Dynamic CFD modeling was achieved using the CFX commercial package, which gave the privilege of applying reciprocation motions (such as Sin wave). Finally, their model was proven against experimental data, and good agreement was observed. In addition to the numerical models, a novel analytical equation was derived by Gołdasz [67], characterizing the behavior of a twin-tube MRF damper. Their model equation included the effect of different parameters values on the damping force, such as fluid chamber compressibility, fluid inertia, cylinder elasticity, friction. All the previous numerical models do not investigate the MRF damper characteristics based on experimental results of viscosity values regarding magnetic field. Moreover, all of those studies used simplified orifices geometries. However, the numerical model that will be presented in this study will try to overcome the mentioned literature pitfalls. Therefore, as is mentioned in Chapter 3, the CFD model will rely on a real case damper orifice geometry. Meanwhile, the viscosity value change with the magnetic field will be tested and included in the CFD model as well.

CHAPTER 3: NUMERICAL WORK

In this chapter, numerical modeling is adopted for understanding, characterizing, and predicting each damper behavior. Numerical modeling will use mathematical models associated with each damper, presented in numerical discretization [68]. In addition, this chapter will include solution algorithms, boundary conditions, and convergence criteria related to the numerical approximation. The FE method will be used to model both MRF damper excitation system magnetic field analysis and FIHD behavior. The COMSOL Magnetic Field (mf) Package was found to be suitable for the magnetic flux representation. On the other hand, FIHD collisions prediction used the LS-Dyna software package. In contrast, the Finite Volume method using CFD analysis was adopted to simulate the flow of the MRF inside the Semi-active damper.

3.1 COMSOL magnetic field analysis

The physics describing a phenomenon in space and time domains are usually expressed in Partial Differential Equations (PDE's) form. These PDEs are hard to be solved analytically when geometrical and boundary conditions complications are included. In contrast, Finite Element Software such as COMSOL solves these equations with a suitable approximation based upon different types of geometrical discretization. In particular, COMSOL-5.6 developed an AC/DC module that provides a solution for physics, including modeling interfaces of many application areas. For example, electrostatics, electric currents, magnetostatics, and time-varying electromagnetic fields applications. A magnetic field interface (mf) was selected to simulate the excitation system of the MRF damper. Magnetic field interface (mf) is used when magnetic field and induced current distributions in and around coils, conductors, and magnets are intended to be calculated and analyzed [69]. Moreover, this physics interface provides

material models regularly being used in magnetic field applications such as; copper, soft iron, and plastic insulators. The following section will present the phases adopted to conduct the magnetic field analysis of the MRF core excitation system.

3.1.1 Numerical model of the excitation system

A 3D SolidWorks drawing was developed for the entire excitation system. The magnetic field excitation system consists of three main parts; cores, core holder, and surrounding ring, as shown in Figure 13. In addition to simulations, 3D drawings have been used for manufacturing purposes of the MRF damper excitation system. The MRF excitation system developed in [46] presents a starting point for further work and improvement adopted in this study. In other words, the same number of cores and core holder dimensions in the previous study [46] was used in this study. In contrast, the core design was enhanced to involve more coils turns and allow a significant interaction between the core and the surrounding ring. In addition, the upper ventilation openings of the core holder were increased in number and dimensions as well to improve cooling by the natural convection.

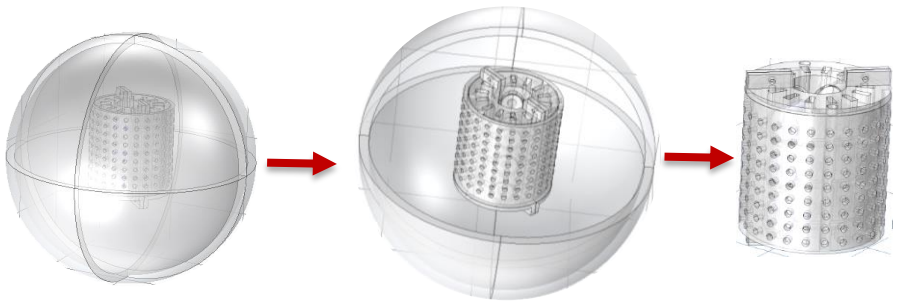

Figure 13. Magnetic field excitation system 3D model.

3.1.1.1 Meshing

As illustrated in Figure 14, the meshing was conducted using the built-in physical controlled meshing of COMSOL. Usually, when using the automatic mesh, tetrahedral elements are created with a predefined size. As in this case, Finer size was adopted. Using "Finer size" mesh, a total of 327043 tetrahedral elements was needed to simulate the entire domain, with a 5.419e-8 element volume ratio and a mesh volume of $0.01405m^3$. To ensure the solving process generates an excellent level of accuracy, the solution should be independent of the mesh size and the number of elements. Therefore, the mesh quality should be examined to confirm that its statistical parameters, such as the skewness, range within acceptable limits. The skewness, defined as the angular measure of the quality of elements, illustrates how ideal is a cell or a face [70]. In the actual meshing, the skewness quality value was found to be 0.615. This value indicates a good mesh quality since it is bigger than the minimum element value of 0.01, illustrated in [70].

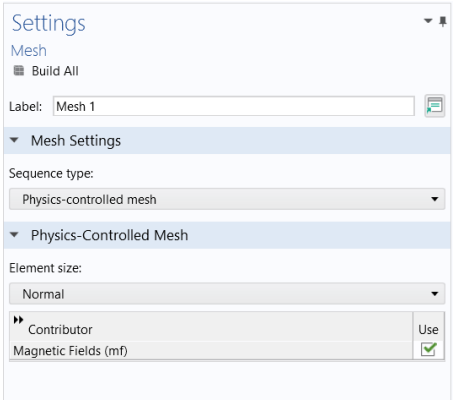

Figure 14. Meshing setup.

The SolidWorks 3D drawing already created four main domains; holder, ring, cores, coils. However, the coils were drawn in a cylinder shape surrounding the core and did not merge with the core body, as shown in Fig (15).

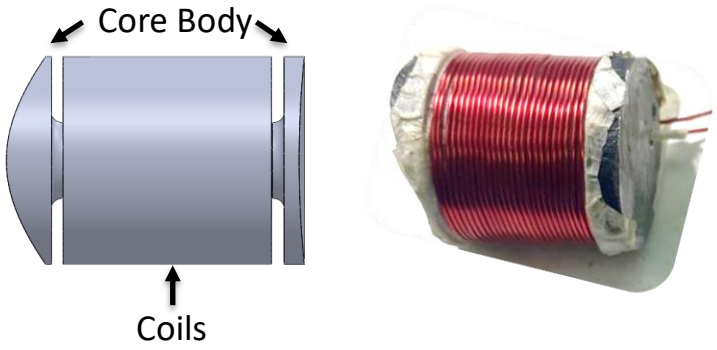

Figure 15. Core & Coils modeling.

The element arrangement through the entire domain is shown in Figure 16.

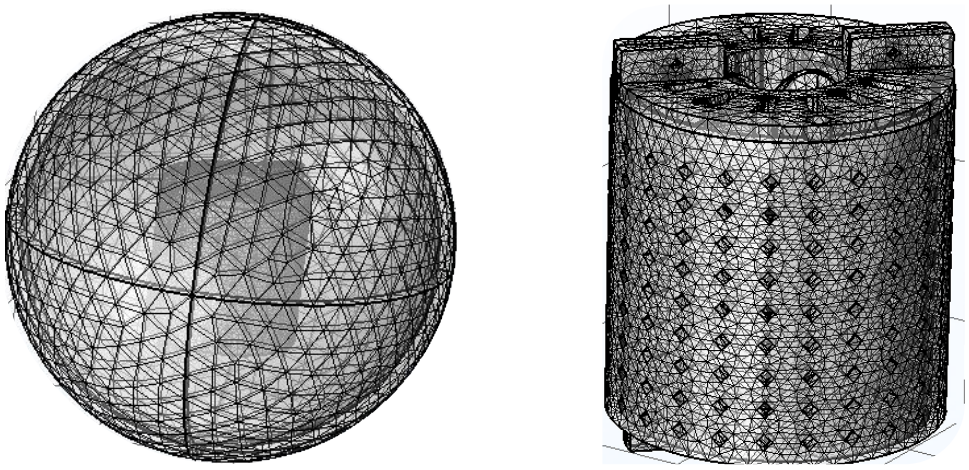

Figure 16. Mesh of the MRF damper excitation system.

3.1.1.2 Governing equations

In electromagnetics analysis, Maxwell's equations fundamentally describe the magnetic behavior when using any device that generates a magnetic field. Maxwell's equation also explains how the magnetic field interacts with different media. The following

equations solve for the “external magnetic field interface with no current”

$$\nabla.(\mu_0\mu_r H) = 0 \quad (5)$$

$$H = -\nabla V_m + H_b \quad (6)$$

$$H = -\nabla V_m \quad (7)$$

where μ_r is the material’s relative permeability, μ_0 is the empty space permeability, H is the magnetic field intensity, H_b is the background magnetic field intensity and ∇V_m is the magnetic’s potential vector. Eq (7) is usually used when simplifying the case by assuming zero surrounding background’s magnetic field intensity. The relationship differs for each material depending on its relative permeability. The general constitutive relation for the magnetic behavior of air medium is

$$B = \mu_0\mu_r H \quad (8)$$

where B is the magnetic flux intensity, and M is the magnetization. The general constitutive equation for the iron particles (magnetic material) is given by

$$B = \mu_0(H + M) \quad (9)$$

3.1.1.3 Electromagnetic excitation system Boundary conditions

Firstly, an infinite element was defined in a spherical shape with 0.1m diameter in order to maintain the system inside. The infinite element simulates the air volume that surrounds the excitation system. Secondly, the material selection was conducted to each domain (part) with properties built-in Comsol material library, as illustrated in Table 5 below.

Table 5. Material electromagnetic properties.

Domain	Materials	Relative Permeability	Relative Permittivity	Electrical conductivity(S/m)
Infinite element	Air	1	1	0
Core	Mild-steel	6000	0.001	1.12e7
Coils	Copper	1	1	5.87e7
Plastic-Holder	ABS	1	1	7.05
Surrounding-ring	ABS/ Mild-steel	1 6000	1 0.001	7.05 1.12e7

Then, coils were modeled as multi-turns circular copper wire. The number of turns was set to 180, which replicates the real-case design of the coils. The current values were increased from 1A to 5A with an increment of 1A. Eventually, a Magnetic field (mf) study including Amper's law, magnetic insulation, and initial value equations was applied to the stationary study. Meanwhile, the (mf) analysis was conducted five times (1-5A) for the two materials of surrounding rings (Mild-steel & ABS). The computational time for each case was approximately 3 hours because of the huge number of meshing elements and the computer processor's mediocre potential.

3.1.3 Results and discussion

The main aim of the COMSOL magnetic simulation was to define the differences between using two different materials for the surrounding ring. The main properties affecting the magnetic field density were the permeability, permittivity, and electrical conductivity of the two materials (Plastic, Mild iron). Figure 17 clearly shows the differences in magnetic field density between the two cases; plastic & metallic rings.

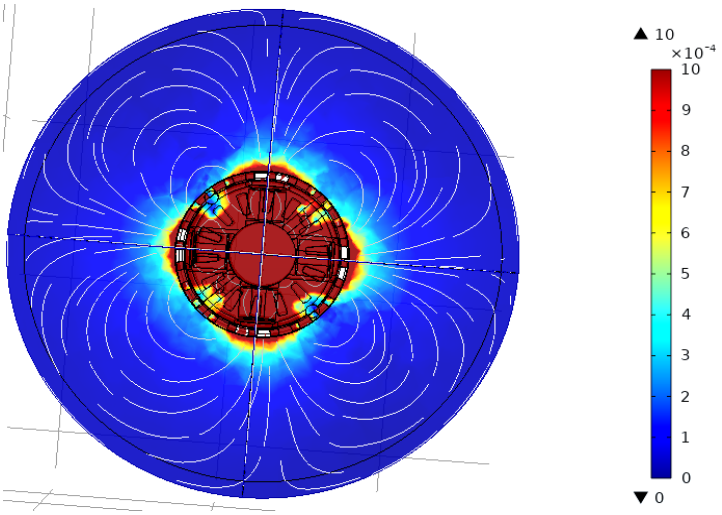

(a)

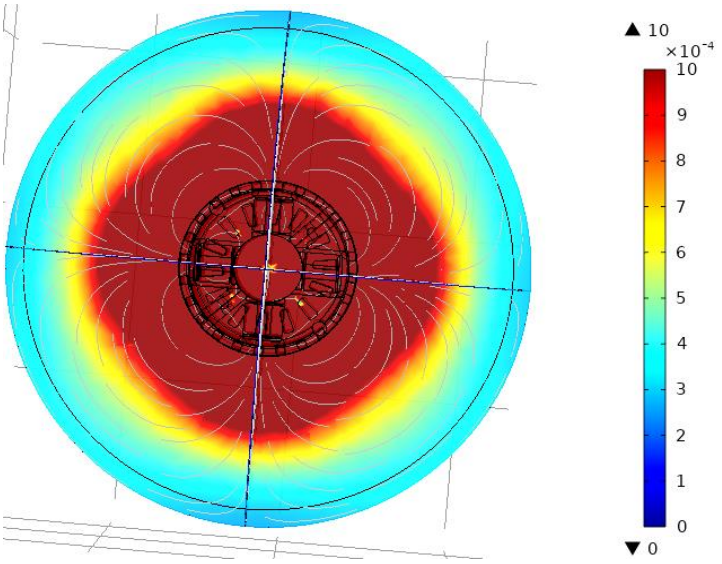

(b)

Figure 17. Magnetic field density contour plots: (a) Metallic ring, (b) Plastic ring.

The contour plot presents the maximum value of magnetic field density in red color, while green/blue colors correspond to its smallest value. An intense value of magnetic field density is concentrated at the center of the core's holder for the two cases. In contrast, the surrounding environment (0.1m away) will have approximately the same maximum value as its center when using a plastic ring. In other words, magnetic flux penetrates the plastic rings and diffuses on the surrounding in a spherical shape with a

0.1 m radius. Using a metallic ring will close the magnetic circuit and prohibit the magnetic flux from passing into the surrounding area. Hence, the maximum magnetic field density value is higher for the metallic ring than the one corresponding to the plastic ring. As displayed in Figure 18, to quantify the simulations' differences, a “Section Cut” is created in the plane (x-y-z). In COMSOL, a straight line, passing on the volume of interest, allows the reading of magnetic field density at those specific locations.

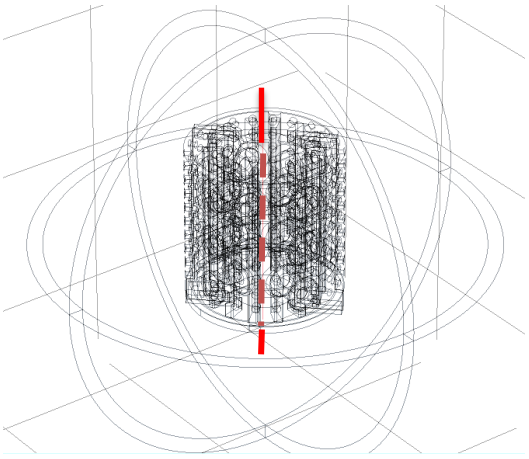

Figure 18. 3D surface line

This line was drawn for all the parametric study cases by using the Comsol Cut Line tool; 3D for Fig.18. Moreover, plotting the magnetic density values along a specific line or direction will highlight the effect of the current increase and surrounding material.

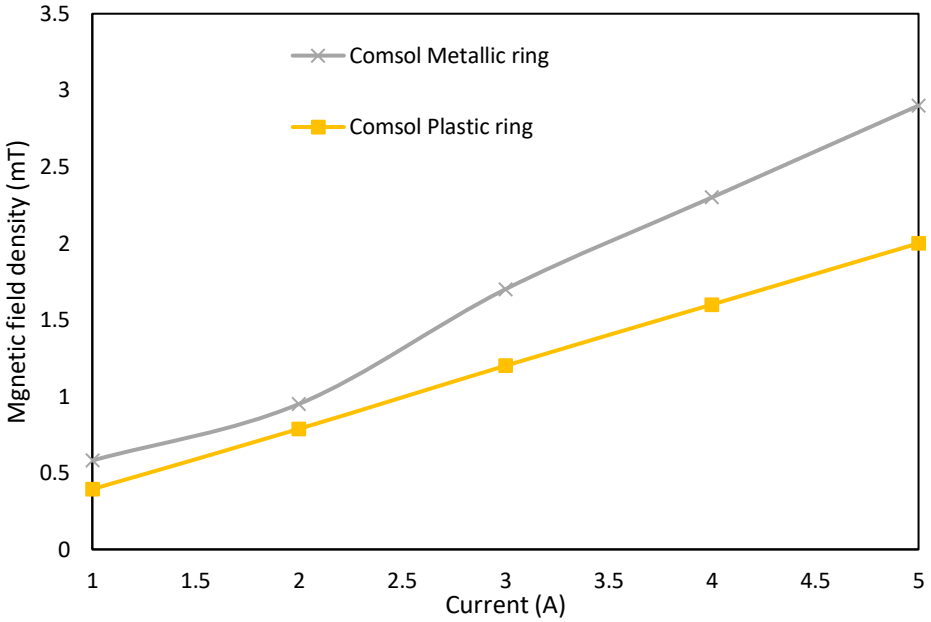

Figure 19. Magnetic field value for the center 3D line

Although the 3D line gave different magnetic density values along the z-axis, the average value was adopted in the above figure. The results illustrated in Fig.19 showed a significant increase in the magnetic field density when using a metallic ring instead of the plastic ring.

To validate the numerical results, a gaussmeter's experiment is conducted. The gauss-meter experiment is further discussed in sub-section (4.3.1). The experimental setup's configuration and the comparison between the experiment results and Comsol model results are shown in the validating the Comsol section in Appendix A. It was found that the Numerical model is very close to the real case scenario with almost 12% error. The permeability, permittivity, and electric conductivity defined in the model for all the domains play a major role in the numerical results' slight divergence from the experimental ones. However, the model's main aim is to show the magnetic field distribution and concentration in a 3D contour plot (Fig.17). In addition, this model was also developed to investigate the surrounding ring material's effect on the magnetic

field density. Therefore, the following Figure (Fig.20) gives the average amplification effect of the metallic ring with respect to the plastic ring.

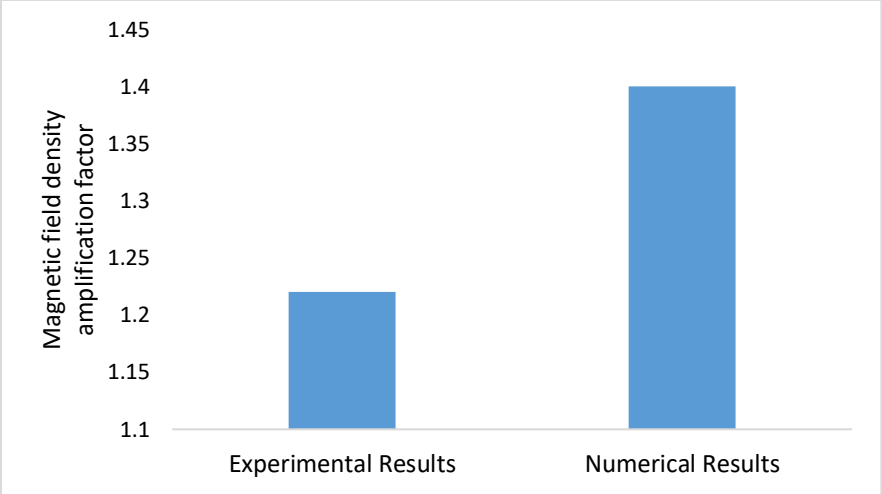

Figure 20. Metallic Ring's effect on the Magnetic field density value

It can be concluded from the previous figure that using a metallic ring will amplify the magnetic field density by almost 1.35 times. Therefore, using a metallic ring will concentrate the magnetic field at the area occupied by the damper and increase its value.

3.2 Viscous damper and MRF CFD model

The CFD numerical investigation requires three significant steps: pre-processing, solving, and post-processing. The pre-processing analysis starts by identifying all geometry dimensions to create the fluid domain. It is followed by an appropriate meshing of the elements, carefully selecting element types and sizes. Finally, initial phenomenon values of temperature and velocities may be calculated in the pre-processing analysis. The basic computational fluid dynamics methodology steps are shown in Figure 21.

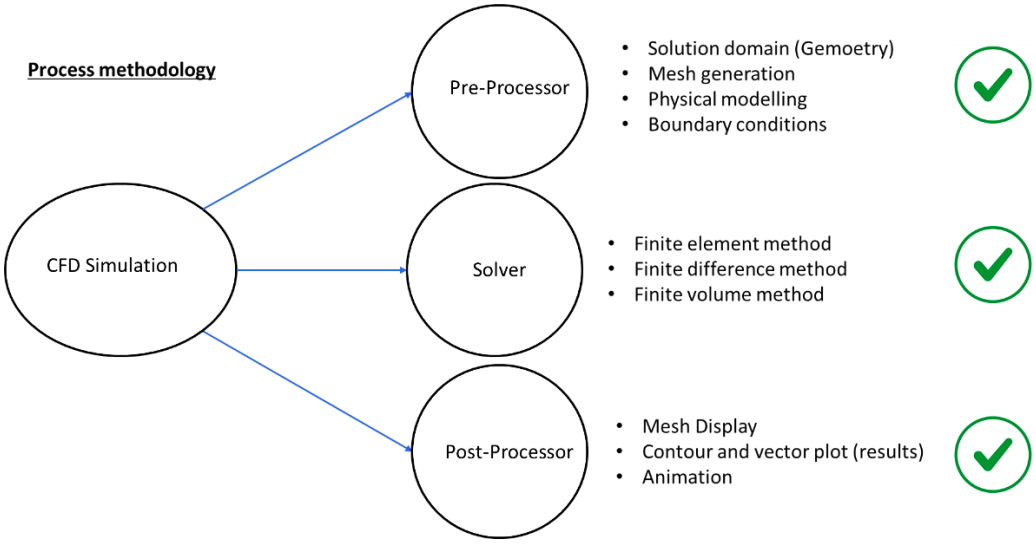

Figure 21. Numerical modeling methodology steps.

The main steps in the solving step include assigning the appropriate model for the study while applying all the boundary conditions needed; material, viscosities, velocity, and pressure to the fluid domains. The post-processing phase will show the contour plot of the static pressure related to the compressing and rebound side of the viscous damper piston.

3.2.1 CFD modeling methodology

The approach considered to develop the numerical model aligns with the procedures previously used in [3] and [47]. The CFD model reported in [3] obtained the damping values for a viscous damper by introducing a fluid flow with a given velocity through an orifice then calculating its pressure drop. The pressure associated with each chamber's side develops a force that contributes to the viscous damper's damping. In the calculation procedure, three main parameters are taken into consideration: fluid velocity, orifice geometry, and fluid characteristics. The main geometrical features that most of the viscous dampers include are shown below in Figure 22.

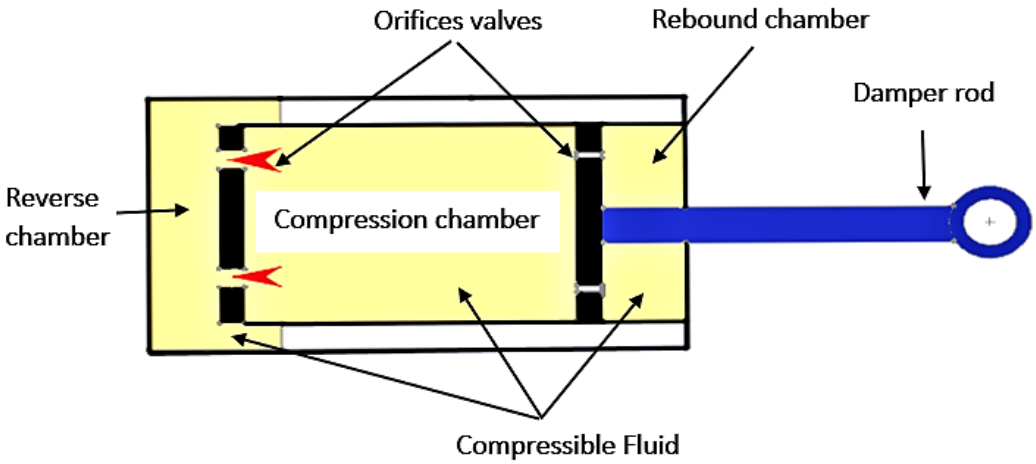

Figure 22. Damper schematic internal details.

The relationships between force and velocity in compression and rebound strokes of the viscous damper are usually nonlinear. However, for moderate values of forces and velocities, the relationship between them could be reasonably considered as linear [37]:

$$F_d = C_d\, V \tag{10}$$

where F_d is the damping force, C_d is the damping coefficient, and V is the piston-damper linear velocity.

According to [3], the damping force is defined as the difference between the rebound and the compression forces. When the damping force considers the fluid's friction effect, Guan et al. [35] proposed the following equation for a twin-tube shock absorber:

$$F_d = P_r A_r - P_c A_c + F_f \tag{11}$$

where F_d is the damping force, P_c is the pressure in the compression chamber, P_r is the pressure in the rebound chamber, A_c is the cross-sectional area of the orifice plate in the compression chamber, A_r is the cross-sectional area of the orifice plate in the rebound chamber, and F_f is the friction force.

Similar to model [13], no friction effect will be counted in the present work.

Although the friction is negligible for low magnetic field values, the micro metallic chain structure will develop considerable friction at high magnetic flux density values. Both rebound and compression forces depend on the static pressure value acting on the orifice surface during the piston's oscillating motions. The fluid is forced to flow from the rebound to the compression chamber across a tiny orifice inside the piston during the piston's reverse motion. Therefore, a pressure build-up, known as rebound pressure, takes place around that orifice. The value of that rebound force is depicted in the following Eq (12):

$$F_r = p_r\, A_r \tag{12}$$

where p_r is the pressure in the rebound chamber, and A_r is the cross-sectional area of the orifice plate located in the rebound chamber.

On the other hand, during the damper rod's extension stroke, the fluid tends to move back from the compression to the rebound chamber. This motion generates a high-pressure value at the compression side. The compression force is given by:

$$F_c = p_c\, A_c \tag{13}$$

where p_c is the pressure in the compression chamber, and A_c is the cross-sectional area of the orifice plate in the compression chamber.

The resultant damping force is due to the subtraction of the rebound force from the compressing force. In the case of constant velocity *V*, the damping coefficient for the rebound and the compression are given by:

$$C_r = \frac{F_r}{V} \quad \text{and} \quad C_c = \frac{F_c}{V} \tag{14}$$

where C_r and C_c are the rebound and compression damping coefficients, respectively. In both cycles of compression and rebound, the velocity values are considered constant [3].

3.2.1.1 Fluent Flow model

The CFD modeling involves the numerical solution of the conservation equations in the laminar and turbulent fluid flow regimes. Therefore, the theoretical predictions were obtained by simultaneous solution of the continuity and the Reynolds averaged Navier-Stokes (RANS) equations. The governing equations for an incompressible flow are [19]

Conservation of mass:

$$\vec{\nabla}.(\vec{v}) = 0 \tag{15}$$

Conservation of momentum:

$$\rho\left[\frac{\partial(\vec{v})}{\partial t} + (\vec{v}.\vec{\nabla}.)\vec{v}\right] = \rho g - \nabla P + \mu\nabla^2\vec{v} \tag{16}$$

where $\vec{v}$ is the flow velocity vector, ρ is the fluid density, g is the acceleration of gravity, ∇P is the, and μ is the fluid viscosity.

Since the flow in the shock absorber is in a state of turbulent motion, it is important to use an appropriate turbulence model for evaluating the flow field. The standard *k*-ε model is a semi-empirical model based on transport equations for the turbulent kinetic energy (*k*) and the dissipation rate (ε). Improvements have been made to the model to improve its performance by the Realizable *k*- ε model [20]. The realizable *k*-ε model has shown substantial improvements over the standard *k*-ε model, where the flow features include strong streamline curvature, vortices, and rotation. The flow governing equations are solved with ANSYS FLUENT 17R. A standard wall function is used for wall treatment since the focus is on the orifice plate. The velocity and pressure coupling used the SIMPLE algorithm with a second-order upwind spatial discretization for a pressure-based study.

The Fluent Flow ANSYS-17 provides different models to simulate turbulence. In this

work, and for the sake of simplicity, the standard - model was used. This choice was considered because this model does not include complex structures or flows involving [71]. The standard k-ε is a two-equation model that includes two transported variables: k is the turbulent kinetic energy, and ε is the dissipating rate of the kinetic energy. Although the realizable model represents an improvement in the standard model [72], a negligible pressure difference was found when comparing the two models' results.

3.2.2 Effect of viscosity and velocity using CFD

In this study, the orifice geometry was reproduced from dimensions used in [3]. According to study [3] findings, increasing the number of orifices will decrease the damping force. The orifices plate was redesigned by modifying the number and location of the orifice holes. A total of 8 orifice holes are placed near the edge of the plate, separated by an angle of (45°). The top view of the orifice plate is shown in Figure 23.

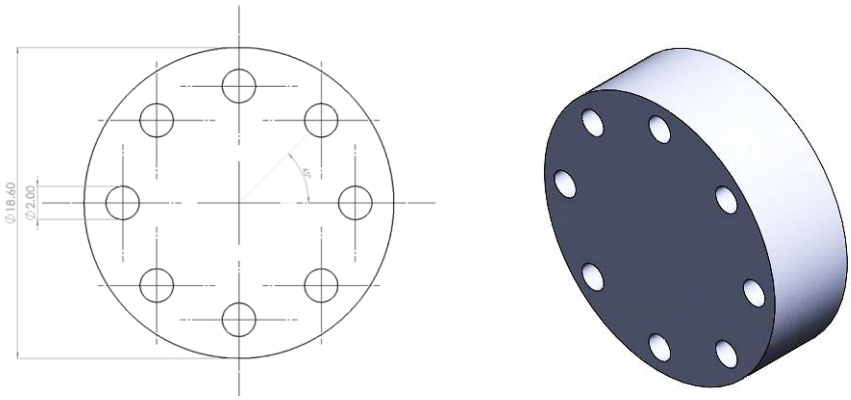

Figure 23. Orifice's geometry and orientation.

Fig. 23 shows the 3D drawing of the damper. The idea behind this model is that CFD simulation will be done inside the cylinder of the damper. As shown in Figure 24-a, this is the domain where the viscous oil will be moving through the orifice plate between the chambers at a specific velocity. Figure 24-b shows the 3D CAD model of the

damper with the eight orifices, as obtained in ANSYS.

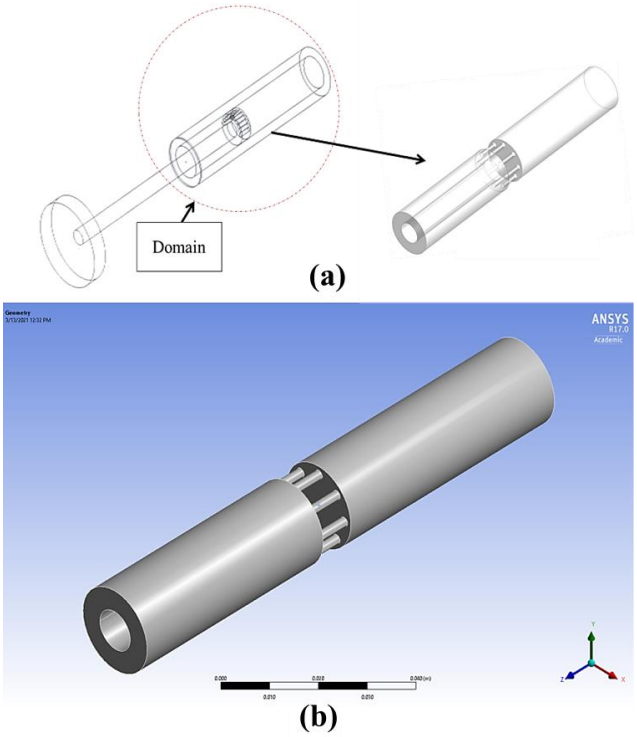

Figure 24. 3D CAD drawings of the damper.

The CFD analysis will be based on throttling the viscous oil through the orifice of the three different cases. This will require the drawing of the inside domain of the cylinder. The oil will be throttled between the two chambers. Therefore, the domain will appear as a solid, but it will be considered as fluid in the CFD simulations. The orifice plate is placed at the midpoint of the length of the cylinder, which is 118 mm. The volume of the orifice plate and the rod (piston) is subtracted so that the domain is only fluid throttling through the orifice for the three different cases.

3.2.2.1 Mesh generation and quality

Unstructured automatic fine meshing with 3D tetrahedral cells was used. The meshing smoothing chooses to be high while having a normal curvature angle of 15°. The mesh responded to high gradient and curvature areas by providing more cells to those areas. By increasing the number of cells at the throttling area while having fewer elements

near the inlet, the outlet ensures accurate results with less computational time. The grid is then generated having 445076 elements with 87552 nodes, as shown in Figure 25.

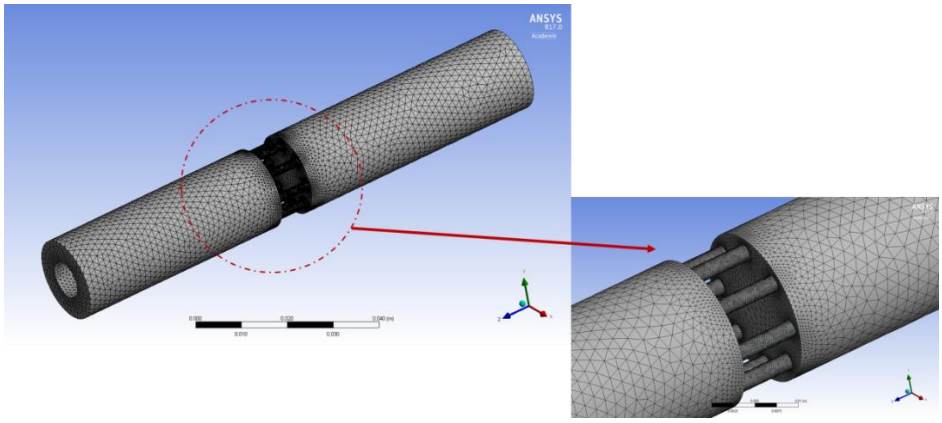

Figure 25. Meshing of the fluid domain.

3.2.1.1.1 *Meshing quality*

The mesh quality is identified through different procedures. A mesh dependence study is the most common method in finding the best size of the element that should be used in the analysis. Although this method is giving a good result, it was found to be a time-consuming method. Three different parameters located in the meshing statistics of Fluent ANSYS gave an indicator for the mesh quality, which are the skewness, the orthogonal quality, and the aspect ratio. Skewness is defined as the difference between the shape of the cell and the shape of an equilateral cell of equivalent volume. Its value ranges between 0 and 1. For tetrahedral elements, any value below 0.95 is acceptable [3]. The skewness of this study was found to be 0.79, which led to a faster solution convergence. Another meshing quality parameter is the orthogonal quality, which refers to how close the angles are between adjacent faces of cells. The conducted minimum orthogonal quality was 0.259, which is in the acceptable range above the minimum value of 0.01 [3]. Lastly, the aspect ratio for a tetrahedral element is the ratio between the sphere radius inscribed in the element and the sphere radius circumscribed in the

element. The maximum aspect ratio for the given mesh is 14.77, which is below the allowable max value of 500 for conducting a good mesh quality [22]. Meshing inputs and results are shown in Table 6.

Table 6. Meshing properties.

	Meshing Inputs				***Mesh Metric (Results)***	
Size Function	**Element type**	**Max element size**	**Min element size**	**Total Elements**	**Max Skewness**	**Min orthogonal quality**
Curvature	Tetrahedral	0.05 mm	0.005 mm	445076	87552	0.25906

3.2.2.2 Boundary conditions and simulation studies

This study focuses on investigating the damping effects on the proposed damper using different values of viscosities (hydraulic fluids) and different flow velocities. The model will simulate the viscous oil throttling from the compression piston side to the rebound piston side and vice versa. Fig. 26 (a) shows boundary conditions when the oil is to be throttled from the rebound piston side to the compression piston side, the inlet (A), the outlet (B), and walls that are separated by the orifice which the pressure is calculated (C). The inlet of Figure 26 (a) was made as an outlet for Figure 26 (b) to simulate the flow from the compression piston side to the rebound piston side.

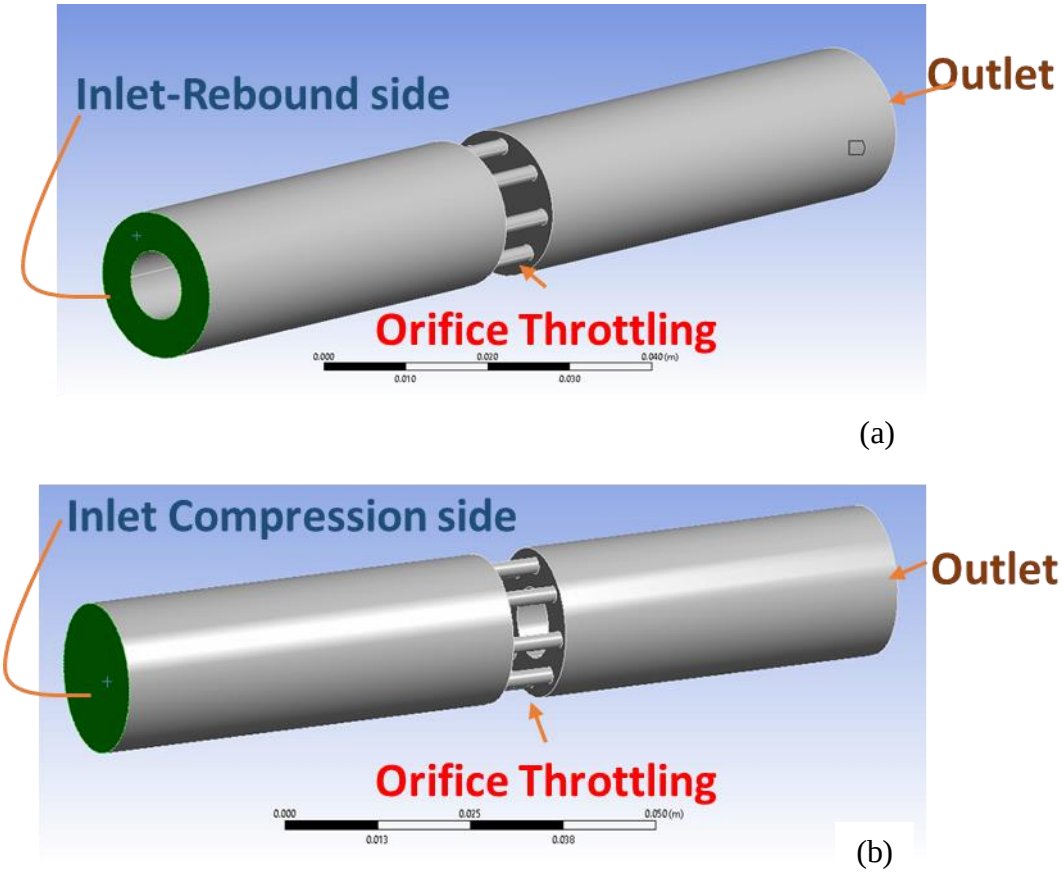

Figure 26. Boundary conditions at (a) Rebound stroke, (b) Compression stroke.

The area of both compression and rebound piston sides was determined, and then the pressure on each piston side was obtained from CFD results, and the force on each side was calculated. Finally, Eq. (13) is used to calculate the damping force. The viscous oil is throttled through the orifice for velocities of 0.8 m/s, 1.0 m/s, 1.2 m/s, and 1.5 m/s. The throttling velocity range and the different viscous oils used are summarized in Table 7. 150 iterations are selected for each simulation, and the convergence criteria are achieved. The solution converged with minimum residuals of 1E-3.

Table 7. Viscous oil types used and their properties [73].

Viscous oil type	Viscosity (Pa.s)	Density (kg/)	Velocity range (m/s)
SVI-25	0.009	841	0.8
3WT	0.0139	860	1.0
HPX R4	0.0169	885	1.2
5WT	0.0186	815	1.5

3.2.2.3 Results and discussion

Static pressure contours are required to identify the forces on the two orifice sides (rebound, compression). The pressure contours for the compression and rebound piston sides for one case are presented in Fig. 27 (velocity of 0.8 m/s and using SVI-25 oil; 0.009 Pa.s).

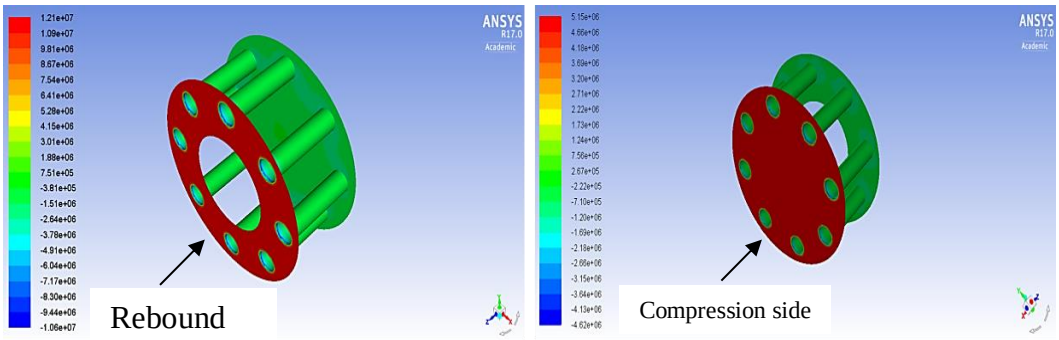

Figure 27**.** Pressure contour for (a) rebound piston side, and (b) compression piston side.

The pressures values for all cases in the compression and rebound piston sides are shown in Table 8.

Table 8. Pressure calculations for compression/rebound piston sides for all cases.

Oil type	Viscosity (Pa.s)	Velocity (m/s)	Pressure on the compression side (Pc) in MPa	Pressure on the rebound side (Pr) in MPa
SVI-25	0.009	0.8	5.15	12.1
		1	7.99	18.8
		1.2	12.4	29
		1.5	19.2	45.2
3WT	0.0139	0.8	5.38	14
		1	8.31	19.4
		1.2	12.9	30.2
		1.5	13.9	32.6
HPX R4	0.0169	0.8	5.6	18
		1	8.6	20.1
		1.2	13.3	31
		1.5	20.6	48.3
5WT	0.0186	0.8	5.27	17.6
		1	8.03	19.6
		1.2	11.4	28.8
		1.5	13.1	31

The rebound-compression forces are calculated with respect to the maximum pressure value observed at the contour plot range. These forces are also related to the piston side surface areas. The compression side area is 1.8569 $x10^{-4}$ m^2, and the rebound surface area is 2.4649 $x10^{-4}$ m^2. The forces acting on a small area (rebound) are greater than the forces acting on a bigger area (compression) due to the pressure difference.

Pressure drops and forces differences generate an essential damping coefficient as a result of subtracting the forces' values at each side divided by the inlet constant velocity. All the results involved in the damping values are shown in Table 8.

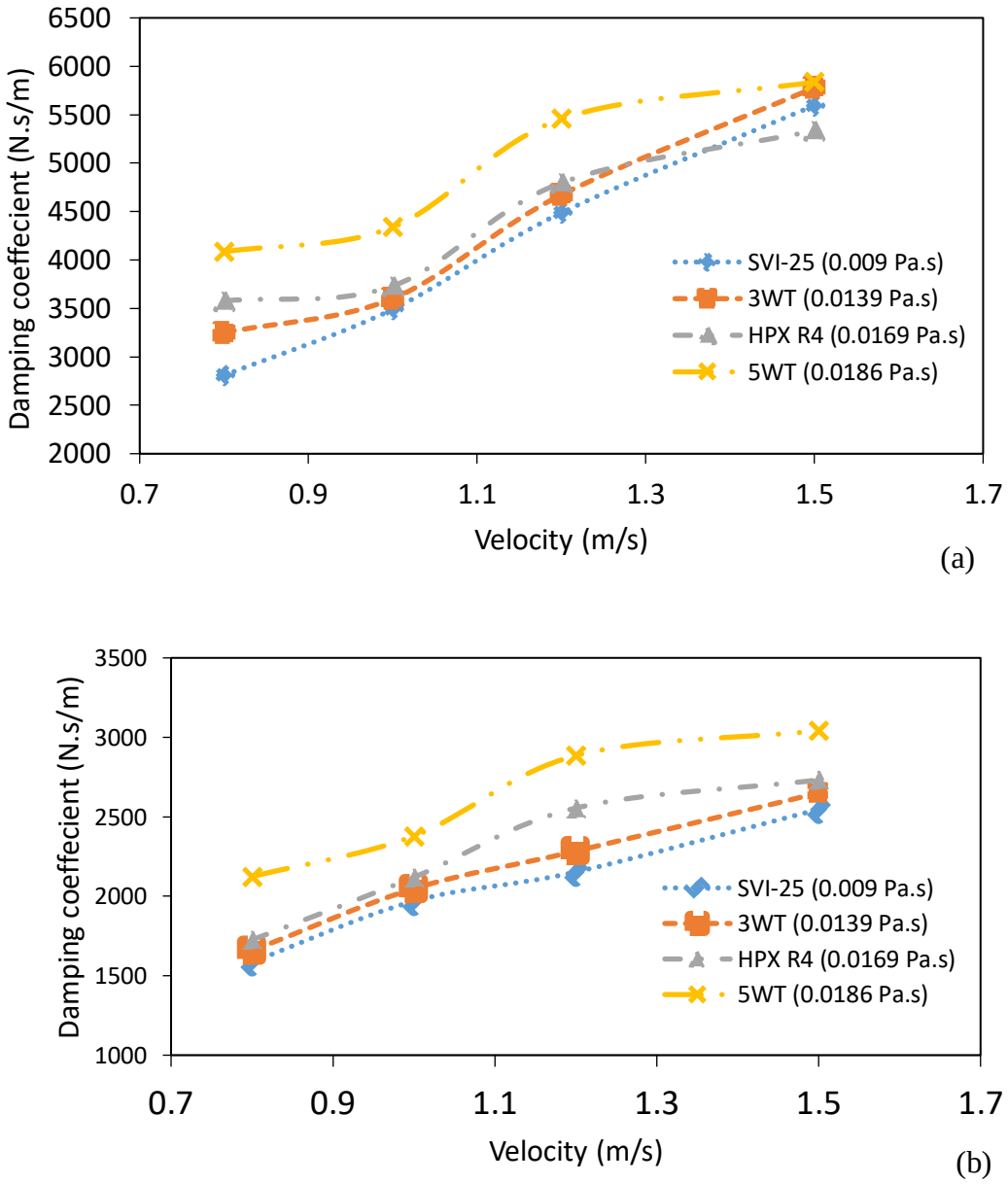

Figure 28. Damping coefficient vs. velocity in (a) rebound piston side, and (b) compression piston side.

Damping values results are shown in Fig. 28 for all types of viscous oils used within a velocity range of 0.8 m/s, 1.0 m/s, 1.2 m/s, and 1.5 m/s. Fig. 28 (a) shows the

damping coefficient variation inside the rebound chamber with respect to the velocity for each oil used. HPX R4 (0.0169 Pa.s) and 5WT (0.0186 Pa.s) oils show a nonlinear behaviour of the damping coefficient-velocity relation. For example, the damping coefficients for HPX R4 oil are 3578.025 N.s/m, 3732.369 N.s/m, 4796.992 N.s/m, and 5335.663 at a velocity of the fluid of 0.8 m/s, 1 m/s, 1.2 m/s, and 1.5 m/s, respectively. The increasing viscosity value can explain the nonlinear behavior of the graph since those oils are higher in viscosity than the other two oils (SVI-25, 3WT). In contrast, SVI-25 and 3WT oils show an approximately a force-velocity linear relationship. For instance, the compression side damping coefficient values for SVI-25 oil with a viscosity of 0.009 Pa.s are 2808.561 N.s/m, 3490.972 N.s/m, 4487.508 N.s/m, and 5595.459 N.s/m at a velocity of the fluid of 0.8 m/s, 1 m/s, 1.2 m/s, and 1.5 m/s, respectively. Similar trends are shown in the compression piston side, as in Fig. 28 (b).

The damping properties increase when the velocity increases. However, values of the damping coefficient increase as the viscosity increase as well. This can be seen from both Fig. 28 (a, b); the graphs are shifted upwards, indicating increases in damping coefficient due to viscosity increase. This means that the damping effect of the oil is enhanced if the oil is more viscous. In addition, the damping coefficient is larger on the rebound side due to the pressure difference between the two chambers. From Fig. 28 (b), the damping coefficient values at a flow velocity of 0.8 m/s are 1586.779 N.s/m, 1657.645 N.s/m, 1725.43 N.s/m, and 2123.753 N.s/m for a viscosity of 0.009 Pa.s, 0.0139 Pa.s, 0.0169 Pa.s, and 0.0186 Pa.s, respectively. However, at a velocity of 1.5 m/s, the trend of the graphs is shown to be different. Damping characteristics is not showing similarity in the direct proportionality. The Reynolds number of the fluids can have an effect in determining whether the flow is laminar or turbulent.

To investigate the hydraulic oil viscous properties, the change in damping

coefficients with respect to the viscosity values was assessed, and the results are displayed in Fig. 29(a) and 29(b). The fluid viscosity represents the resistance to the gradual deformation by shear stress. Fig.29 (a) and (b) depict the rebound chamber damping coefficient variation with the viscosity. It can be clearly seen that as the oil becomes more viscous, the damping effect is higher. This is because the resistance to the stresses and the ability to damp the motion is higher in the viscous oil. A linear relationship of damping-velocity was obtained for almost all oils used at low velocities. However, HPX R4 oil developed a nonlinear damping-velocity for all the values of the velocity range.

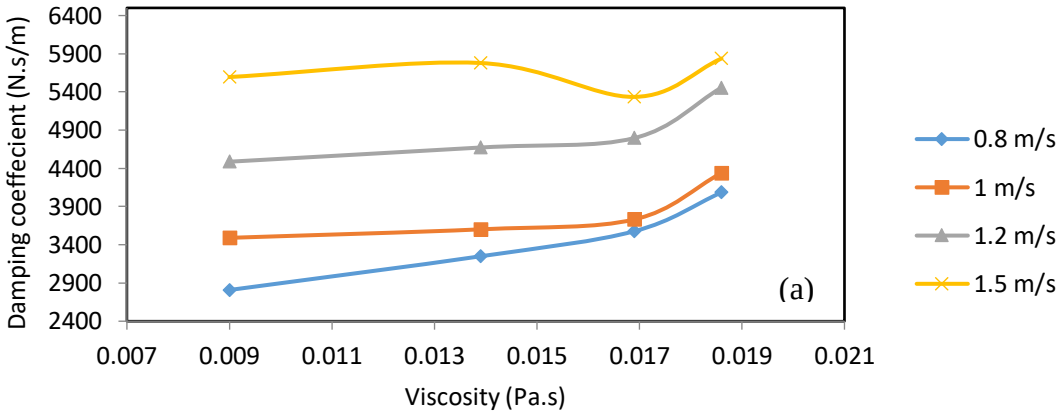

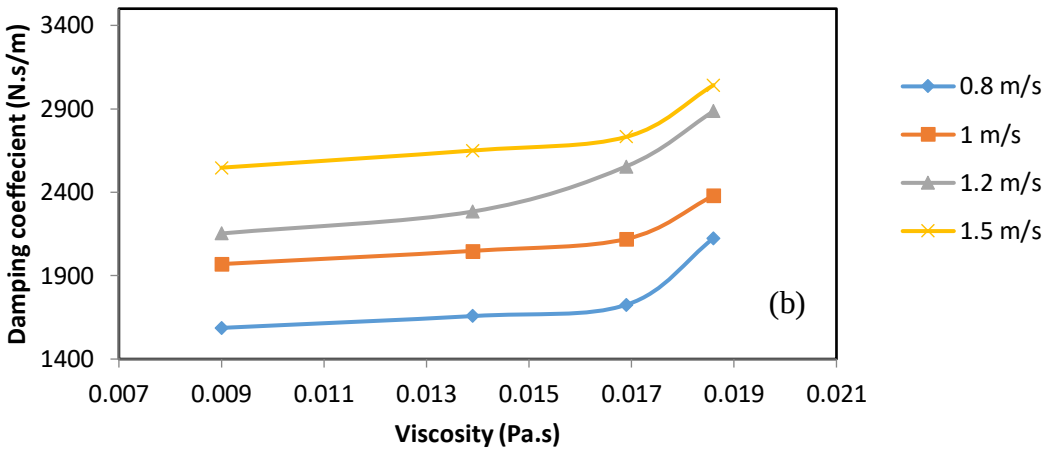

Figure 29. Damping coefficient vs viscosity in (a) rebound piston side, and (b) compression piston side.

3.2.3 Using the CFD model in MRF dampers

The fluid viscosity used in [3] was considered constant since the damper's viscous fluid was deemed Newtonian. However, the MRF is a non-Newtonian fluid, and therefore its viscosity value may change with the variation of the applied magnetic field. A typical change of an MRF viscosity is depicted in the results generated by an FE-CFD coupled model [47]. The FE magnetostatic model was developed to calculate the magnetic flux density inside the MR damper flow gap. Different viscosities were found and then implemented in the CFD model based on each excitation current's magnetic flux density values [47]. In this section, the MRF damper will be modeled using the model considered in the previous sub-section, which calculates the damping coefficient by calculating the forces acting on the compression and the rebound sides of the piston for constant velocities. Viscosity values illustrated in Chapter 3 will then be used and identified in the material properties section in the Fluent flow model.

3.2.3.1 Diaphragm geometry

The previous studies' orifices were commonly considered small thickness cylinders with many holes [7], [35]. The fundamental orifices' detailed small design features were frequently neglected. These small design features (like non-uniform edges) may substantially contribute to the pressure drop and the damping effect. In this study, the damper under investigation was previously used in a former experimental research work [46]. The damper was disassembled, and its internal parts were checked to get their accurate dimensions and shapes. The graphical details are displayed in Figure.30 and Figure.31.

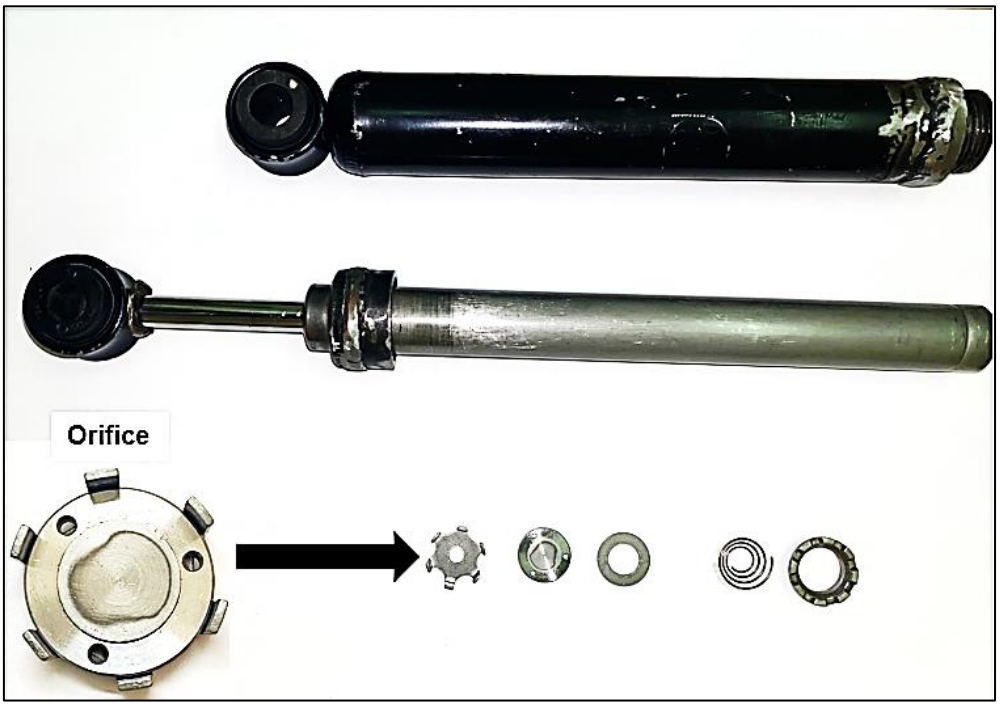

Figure 30. Damper internal components.

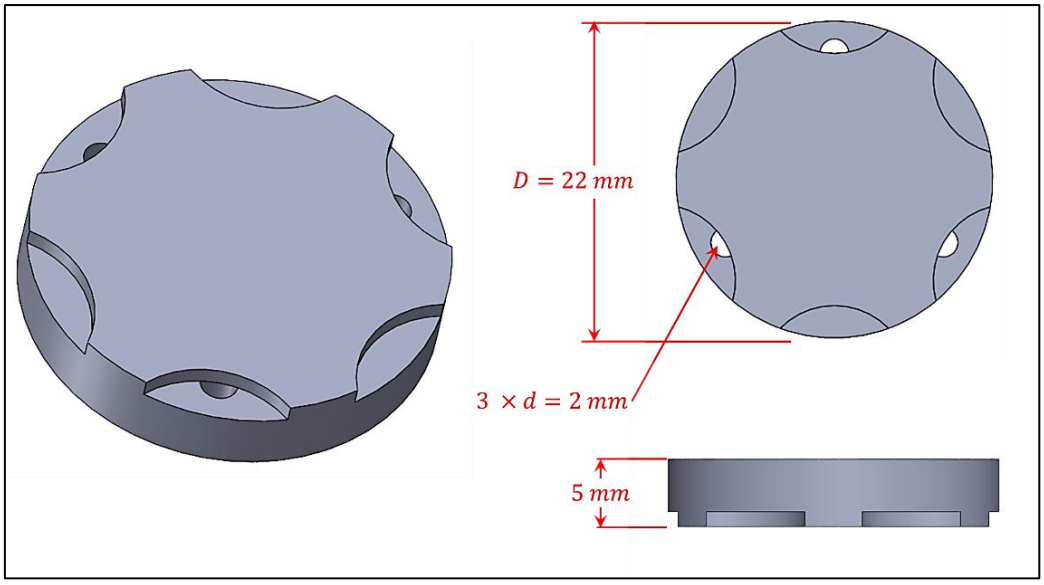

Figure 31. 3D CAD drawing of the orifice.

3.2.3.2 Meshing Computational Analysis

In this CFD model, the meshing is concerned with the flow area, which starts from the inlet through the throttling orifices, all the way to the outlet. Unstructured automatic fine meshing with 3D tetrahedral cells was used. The meshing smoothing was chosen to be high while having a normal curvature angle of 18. The mesh responded to high gradient and curvature areas by providing more cells to those areas. Increasing the number of cells at the throttling area while having fewer elements at areas near the inlet and the outlet ensures accurate results with less computational time. The grid is then generated having 58169 elements with 12151 nodes, as shown in Figure 32.

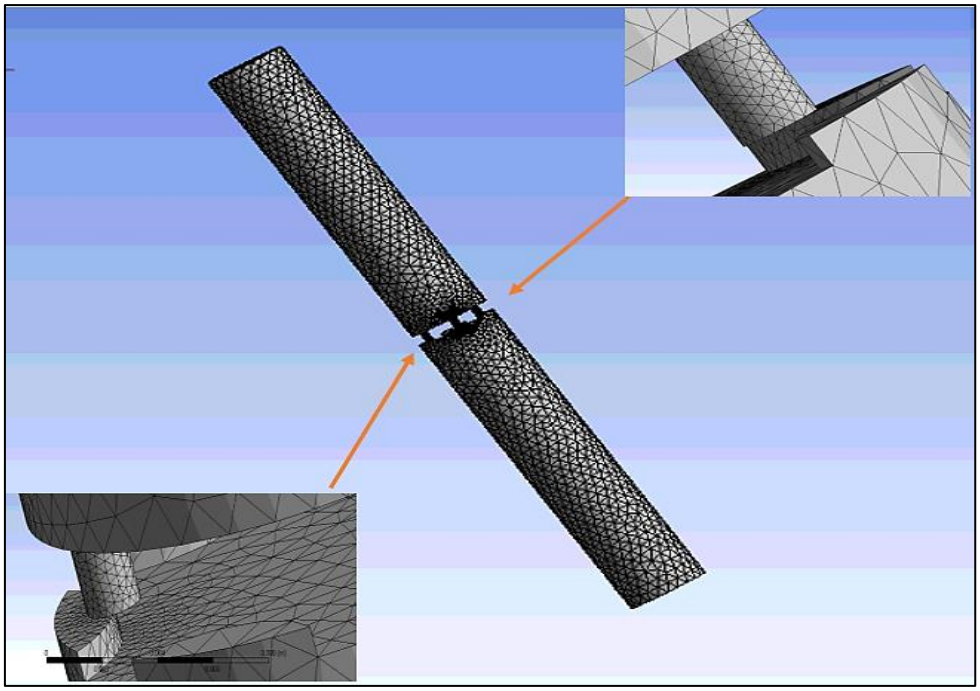

Figure 32. Meshing of the flow area.

The skewness of this study was found to be 0.72, which led to a faster solution convergence. Another meshing quality parameter is the orthogonal quality, which refers to how close the angles are between adjacent faces of cells. The minimum value of the orthogonal quality was found to be around 0.2. When such a value is above the minimum allowable limit of 0.01 [74]. In addition, the maximum aspect ratio for the given mesh is equal to 14.77. Such a value is below the allowable max limit of 500, usually obtained when the mesh is of good quality [74].

3.2.3.3 Simulation and Modeling

After achieving the grid of the fluid area, the standard - model was used, as discussed in the 3.2.1 sub-section. The viscosity values displayed in Fig.62 (Chapter 4) were assigned to the liquid-water material characteristics to investigate the magnetic field density variation effect. For the material type settings, the fluid was considered viscous with a density of 3090 Kg/m^3. The velocity was set to 0.08 m/s, as mentioned in the

experimental reference [37]. A simple method was used for coupling pressure and viscosity and a second-order upwind spatial solver to increase accuracy. The rebound and compression pressures should be both considered for finding the damping coefficients. Both scenarios were considered in the CFD model to find the pressure at both sides of the orifices. Firstly, the fluid flow was supposed to be from the rebound chamber to the compression chamber with an initial velocity at the inlet boundary layer. This scenario will have a maximum pressure value at the orifice surface directly facing the inlet boundary. Reversing the flow direction by changing the inlet and the outlet boundary while maintaining the same velocity will result in compression pressure.

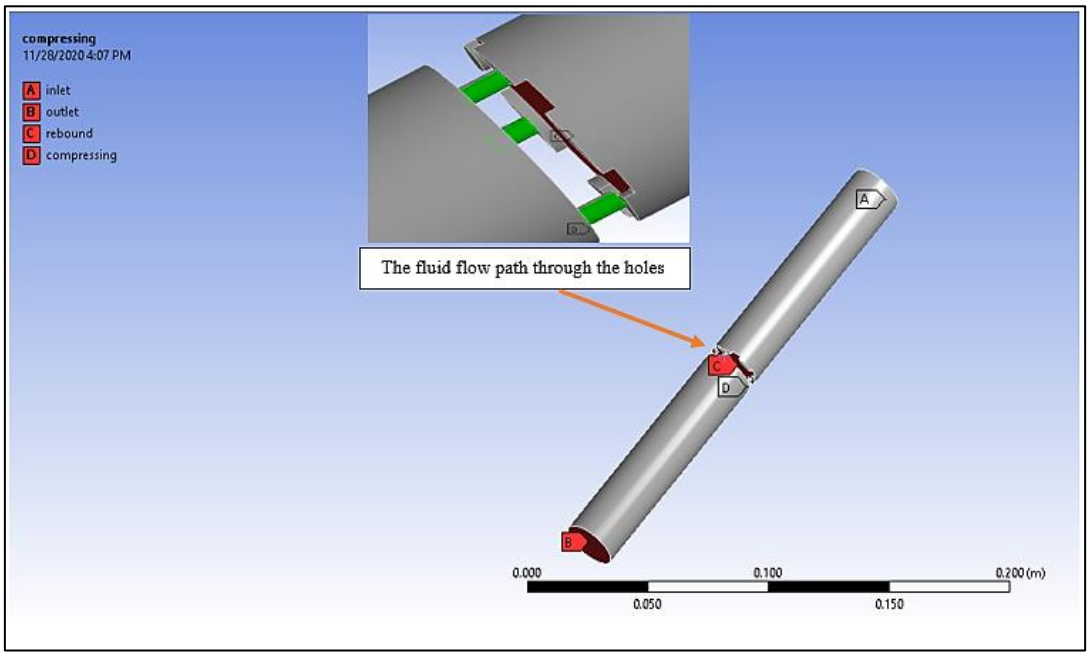

Figure 33. Boundary conditions.

Figure 33 shows the inlet, outlet, and three orifice holes of the fluid flow. Rebound and compression areas are name-selected for later pressure contour representation. A constant pressure condition was assigned to the outlet. In the meantime, as a boundary condition, the cylindrical partitions were modeled as walls. Only the inlet boundary is giving a constant value of 0.08 m/s representing the damper rod velocity that delivered

the first damping value in the reference experimental study [46].

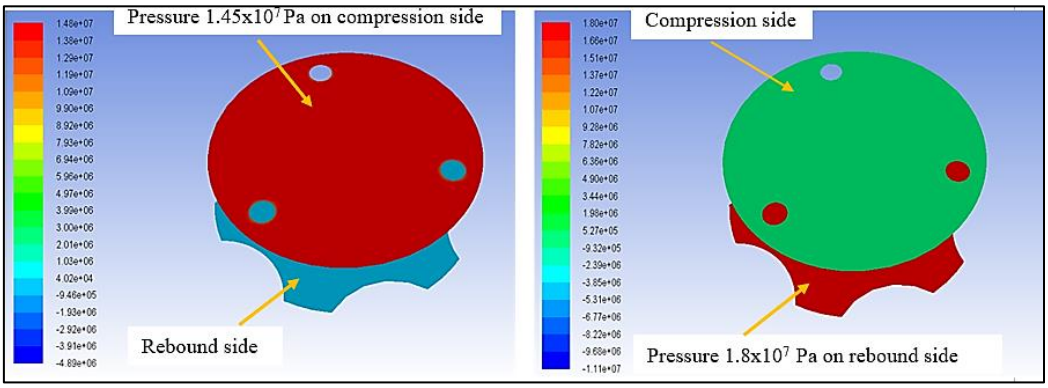

(a) (b)

Figure 34. Pressure contours for (a) compression stroke (b) rebound stroke of a piston for 1 A current applied.

After computing the results, the contours post-processing tool in CFD enabled showing the characteristic gradients, namely velocity, total pressure, dynamic pressure, and shear strain. In this study, only static pressure is required to identify the forces on both orifice sides (rebound, compression). Figure 34 displays an example of the static pressure contour plot for the rebound and compressing sides of the piston for an applied current of 1 A.

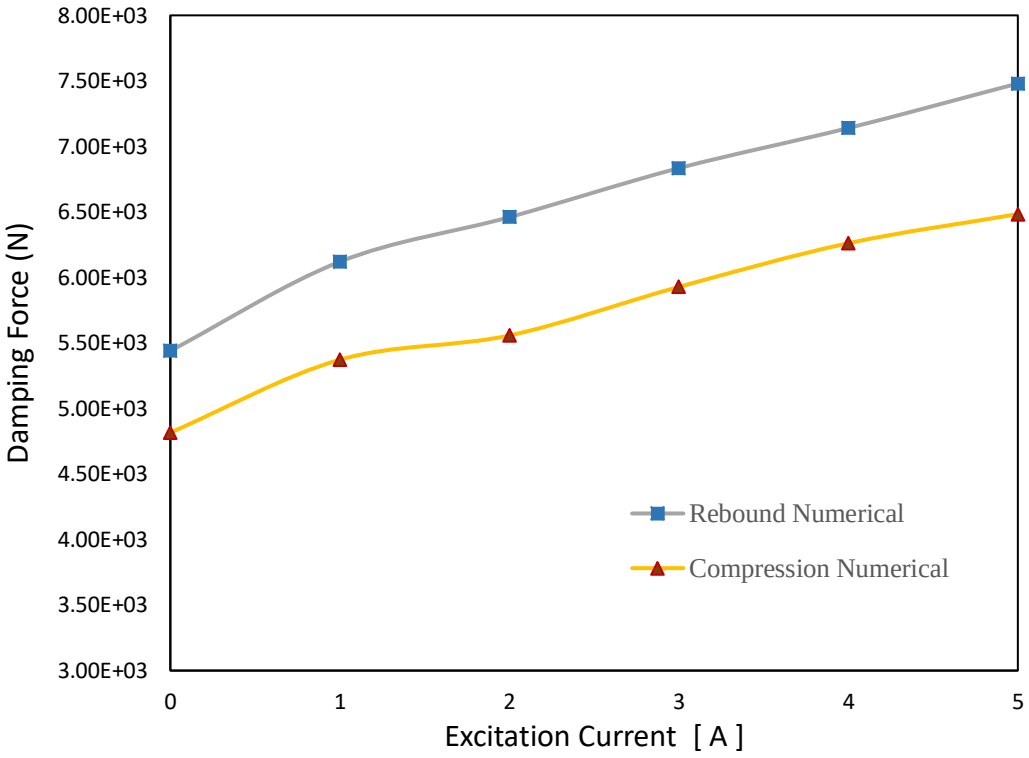

Figure 35. Damping Forces [N] Vs Excitation current in rebound and compression chambers

The rebound-compression forces are calculated for the maximum pressure value observed at the contour plot range. These forces are also related to the piston side surface areas. The sides areas are (3.71×10^{-4} m^2) at the compression side and (3.40×10^{-4} m^2) at the rebound side, respectively. Consequently, the rebound force is more significant than the compression one because of the difference in the area values. As already explained in equations (5) and (6), the pressure drop generates different forces on both sides of the piston which difference, divided by the inlet constant velocity, results in damping effect. All the results involved in the damping values are shown in Figure.35.

3.3 FIHD LS-Dyna model

To understand and gauge the damping when two different mechanisms (viscous and impact) are combined in a single device, a finite element (FE) investigation was conducted based on the commercial software LS-Dyna. It is an explicit multi-physics simulation program commonly used to simulate short-duration dynamic problems such as collision phenomena. Many parameters determine the need for using nonlinear analysis, such as geometry, material, support, and boundary conditions [75]. In order to have a better understanding and for further implementation of the LS-Dyna model in such an application, the below diagram (Fig. 36) shows the steps of the model.

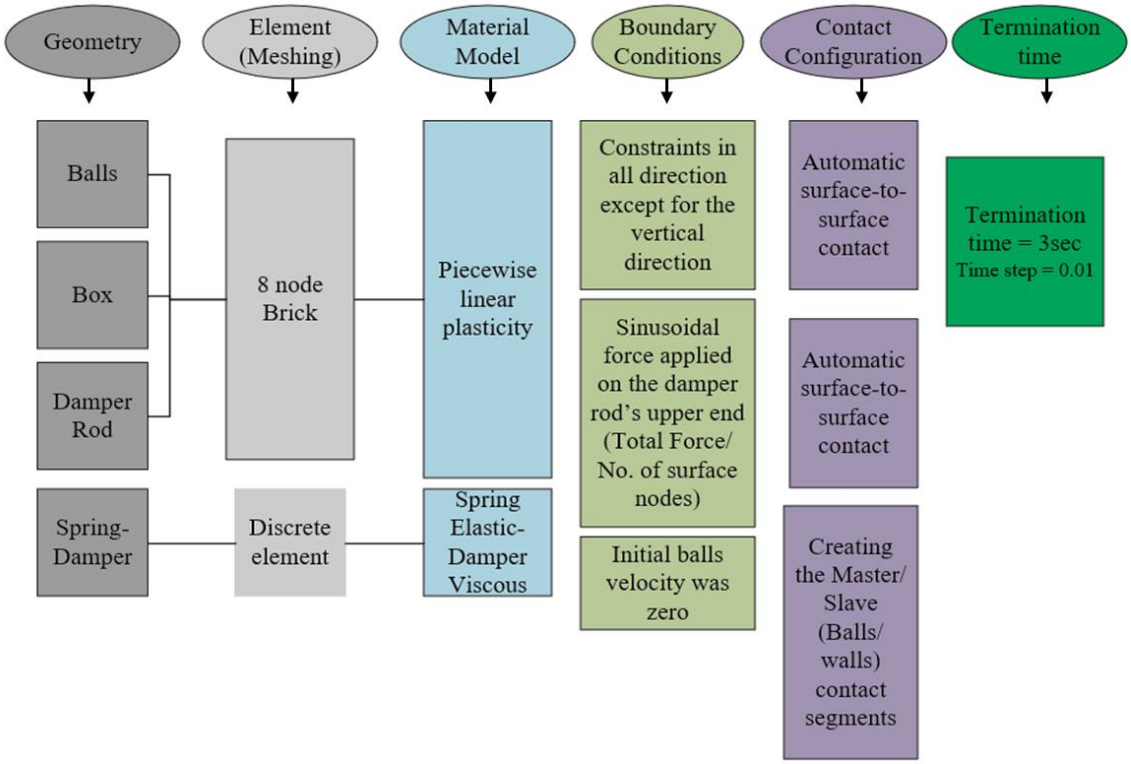

Figure 36. LS-Dy detailed modeling steps.

3.3.1 LS-Dyna governing equation

In general, LS-Dyna simulates the collision by finding a solution for the momentum Equation (17) [76]:

$$\sigma_{ij} + \rho f_i = \rho \ddot{x}_i \tag{17}$$

where σ_{ij} is the Cauchy stress tensor, ρ is the material density, f_i is the body force density, and $\ddot{x}_i$ is the body's acceleration. Cauchy stress tensor is a nine components tensor that defines the state of the stress inside the material, whether the state was deformation, placement, or configuration [77].

The changes of the deviator stress with time at the contact area affect the contact force value, hence changing the damper's acceleration response. The updated acceleration value in the momentum equation defines the contribution of the particles in the damping characteristic of the FIHD, as shown below in Fig.37.

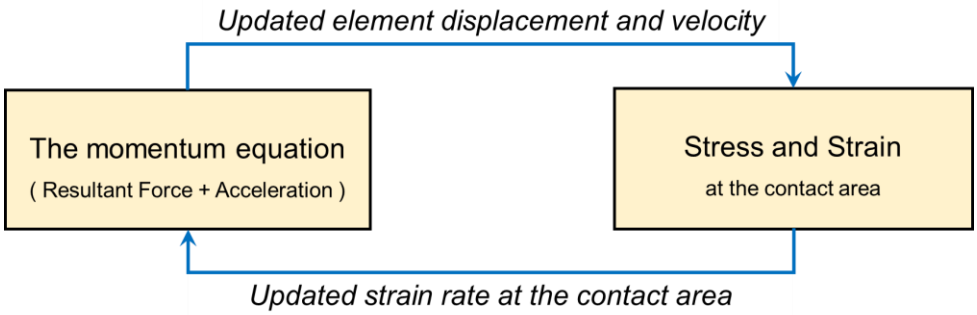

Figure 37**.** Numerical model analysis steps.

3.3.2 FIHD Geometry and Meshing

Five main parts were considered to create the model geometry: damper rod, box cover, base, spring-damper system (modeling the VFD), and balls. The cylindrical wall of the box was neglected because the study scope is focused on external collisions (balls box-cover, balls box-base). To include the mass of the walls, the density of the box material was increased with the appropriate fraction. The box's cover and base diameters were set to 70 mm, while their thicknesses were set to 10 and 5 mm, respectively. The meshing density was set at ten elements per mm, using an 8-node brick element. Such

element was assigned for all the solid parts, based on the findings of (Aryaei, Hashemnia, and Jafarpur, 2010), and the applicability material model and element table in the LS-Dyna manual [76]. The piston rod was modeled as a solid part with an element density of 10 elements per mm. Merging the rod with that PID box was conducted by refining the mesh at the rod edges, creating more nodes for duplication, and creating a rigid body movement. The fluid damper system was modeled by creating a straight line between the rod's lower face center and a constrained node (Fig. 38). The node is vertically distanced by 10 cm from the rod's lower face center. Two discrete elements section was assigned to the straight line to simulate the VFD using the Maxwell model.

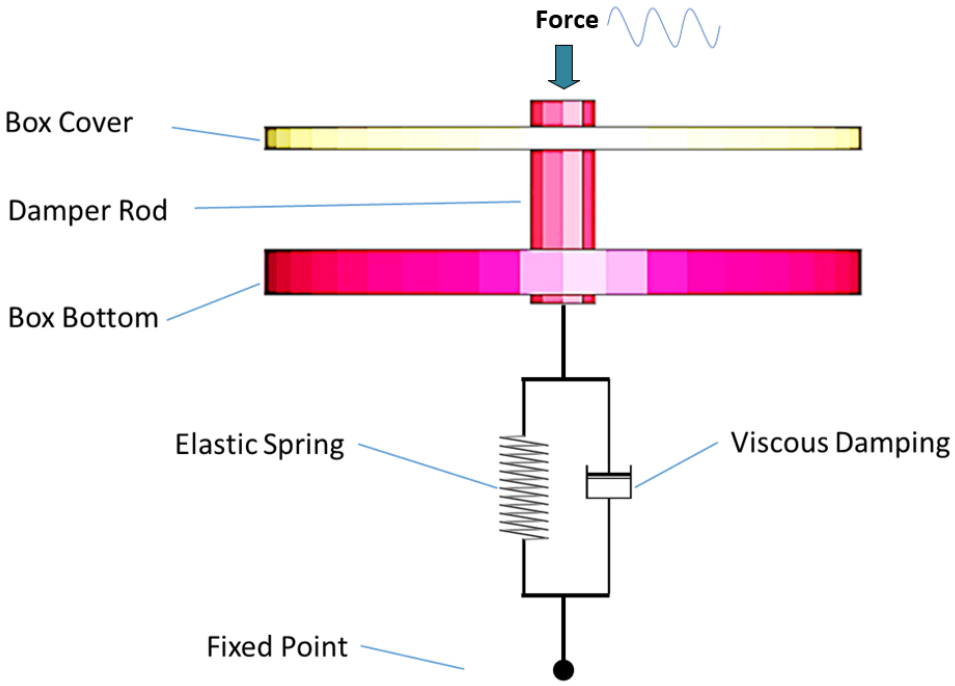

Figure 38. FEM model of FIHD without balls.

The Maxwell model consists of a linear spring and a dashpot in series (Akcelyan et al., 2018). The linear fluid damping coefficient (C) value was found based on the experimental test conducted on this damper [37]. The objective of the test was to investigate the linear change of damping value with the force-frequency magnitude.

The study observed the C value variation at five frequencies (1, 3, 5, 7, and 10 Hz). At the range between 1 and 6 Hz, the damping value was quasi-stable. However, starting from 7Hz, the amount of damping increases significantly, as shown in Figure 39.

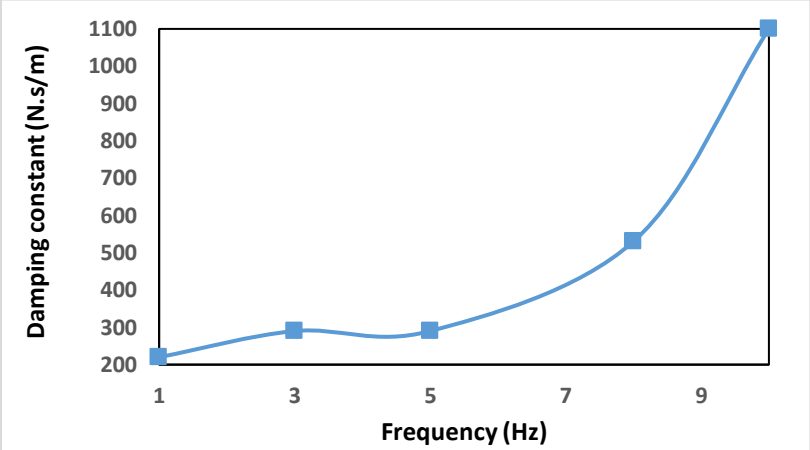

Figure 39. The changing of Damping Constant value with Frequency.

Based on the previous finding [37], 220 N.s/m was the C value adopted for the linear dashpot discrete element. The axial stiffness was estimated at 90 N/m, representing the slope of the force-displacement linear part, at the vicinity of 1 Hz.

3.3.3 Material Models

The LS-Dyna theory manual [76] also suggests using a piecewise linear plasticity (isotropic) material model for the understudy balls and box material. The selected material describes the elastoplastic balls-walls collision of the FIHD. The developed strain rate (determines the Cauchy stresses, which affect the system acceleration value. This strain rate ($\emptyset$) is a function of the deviator stresses (s_{ij}), and the yield (σ_y) as shown in the Equation (18) [76]:

$$\emptyset = \frac{1}{2} s_{ij} s_{ij} - \frac{{\sigma_y}^2}{3} \leq 0 \quad (18)$$

The isotopic values of density, Poisson ratio, elastic modulus, yield stress, and tangential modulus assigned to the materials of the box, rod, and balls are obtained from (Samal, Valko, and Pannell, 2009) and [80]. The material's mechanical properties used for the LS-Dyna model are provided in Table 9.

Table 9**.** FEM Material properties.

Part	**Damper Rod**	**Balls**	**Plastic Box**
Material	Mild Steel	440C Stainless Steel	ABS
Density, [g/cm3]	7.87	7.7	1.05
Poisson Ratio, ν	0.3	0.3	0.3
Elastic Modulus, E [GPa]	210	200	2.28
Yield Stress [MPa]	450	450	40
Tangential Modulus (1% of E) [GPa]	2.1	2	0.028

3.3.4 Boundary conditions & Contact configuration

To reproduce the experimental conditions of the shaking system (Chapter 4), a 400-N amplitude sine curve was selected inside the defined force of the LS-Dyna model. The contact was controlled by defining a primary/replica (balls/box walls) condition and selecting two-way automatic surface-to-surface to avoid nodes penetration in both the primary and replica. Finally, the termination was set to three seconds, with a step of 0.01 seconds in the software's database category. The LS-Dyna FE models of FIHD for the three considered cases are shown in Fig.40.

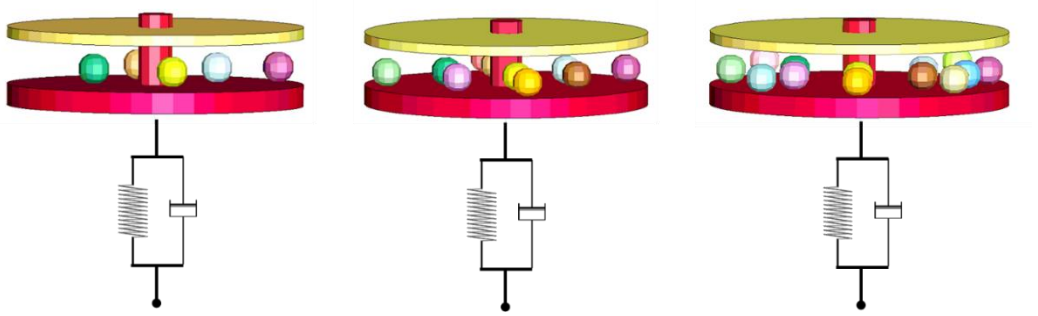

(a) (b) (c)

Figure 40. The FEM of the FIHD having a different number of balls;

(a) 5 balls, (b) 10 balls, (c) 15 balls

3.3.5 Model verification

Developing computational models to make engineering predictions with quantified confidence required implementing a verifying methodology. Verification and Validation (V&V) is the developed methodology to solve the growing people of numerical models uncertainty [81]. However, the Mesh dependence study presents a starting point for the V&V process. Moreover, model verification is usually conducted by comparing the numerical results to an analytical mathematical model. In our case, HFID without balls simulate the behavior of a simple mass-spring-damper system. and the balls' collisions.

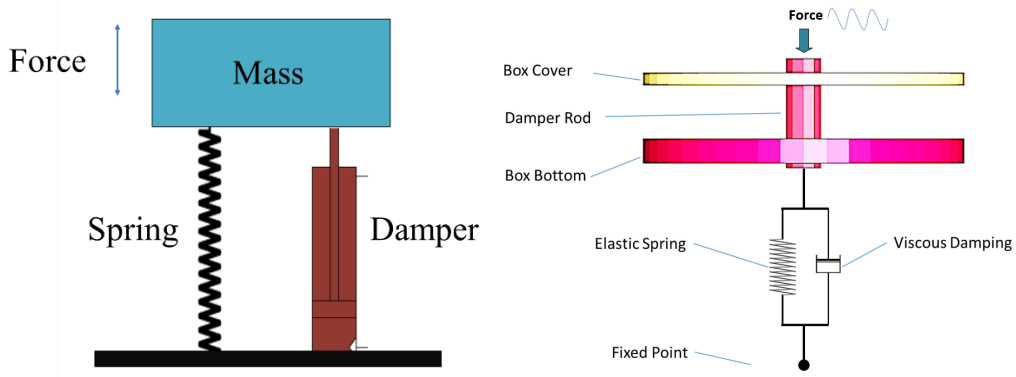

Figure 41. FIHD Mass-spring-damper system.

The above system (Fig.41) can be modeled using the basic second-order equation of motion by examining the sum of the forces acting on the mass Eq(19) [82].

$$F = M\ddot{x} + C\dot{x} + Kx \qquad (19)$$

where F is the dynamic force, M is the mass of the system, C is the damping coefficient, and K is the linear spring stiffness. Consequently, a single degree of freedom natural frequency equation could be subtracted from the above Newton's equation as shown in the below equation (Eq (20)) [82].

$$\omega_n = \sqrt{\frac{K}{M}} \qquad (20)$$

The second step was to obtain M value for the damper moving part and K values associated with passive fluid stiffness. The overall mass was found to be 0.6 kg (0.52 kg for the damper's rod and 0.08kg for the PID box). Viscous damper stiffness was found to be 90 N/m, by finding the slope of the Force-Displacement experimental results in [37]. Therefore, Consequently, 1.95Hz was the natural frequency of the mass-spring-damper system. Furthermore, the numerical FRF results shown in the following section (Fig.43) show a peak localized around 2Hz, which corresponds to the system's analytical natural frequency.

3.3.6 Results of the FIHD Numerical Model

LS-Dyna Post-processing shows different kinds of results to be shown as animation, fringe plotting, or even curve plotting [83]. Results are mainly concerned with the time dependency change of the model's energy, stresses, displacement. However, the understudy damper characteristics were evaluated by comparing the FRF results of the parametric study cases. FRF is defined as the amount of acceleration transmitted to the FIHD system regardless of the input force. Lower the FRF value indicates better damping capability of the FIHD damper. The plot time history interface used the plot function to obtain the damper rod part acceleration in the y-direction. Fig.42-a shows a sample result of FE acceleration time response at 1 Hz in the damper rod part's vertical (y) direction. The acceleration time response data was then processed by using the MATLAB vibration data analysis tool. This tool uses the well-known Fast Fourier Transform (FFT) built-in function to convert the original signal from time to frequency domain. Using this tool, the magnitude of the frequency response was calculated and displayed in Fig.42-b.

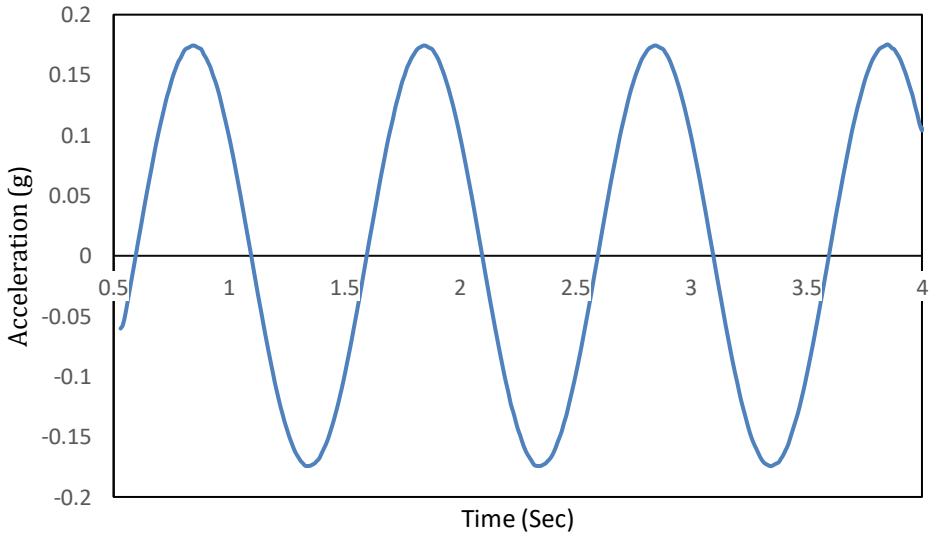

(a)

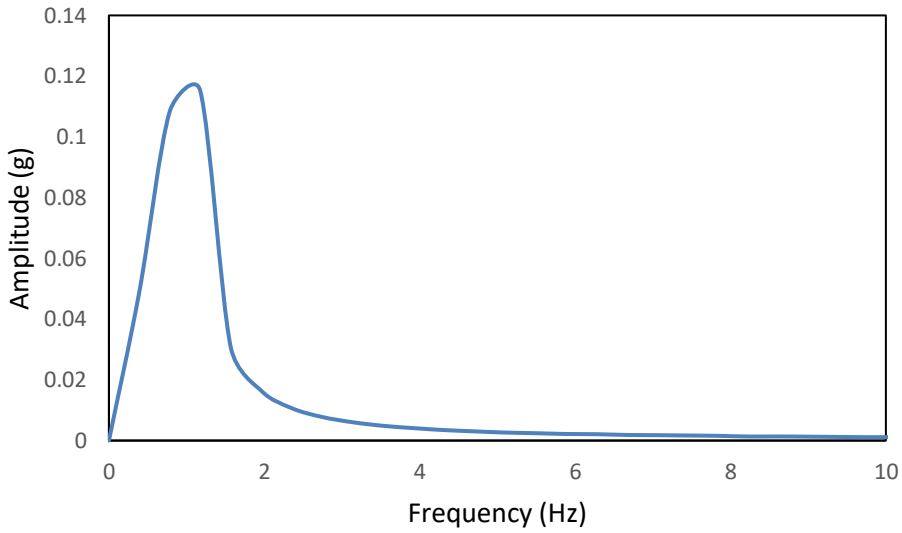

(b)

Figure 42**.** FEM sample result of acceleration at 1Hz; (a) Time response; (b) Frequency response.

The FRF was obtained by numerically dividing the spectrum of acceleration response (output) by the spectrum of excitation force (input). Both forces and accelerations responses in the frequency domain were processed by using the MATLAB vibration data analysis tool. The numerical model FRF parametric study of FIHD, when the PID box is empty and filled with a different number of balls, is presented in Fig.43.

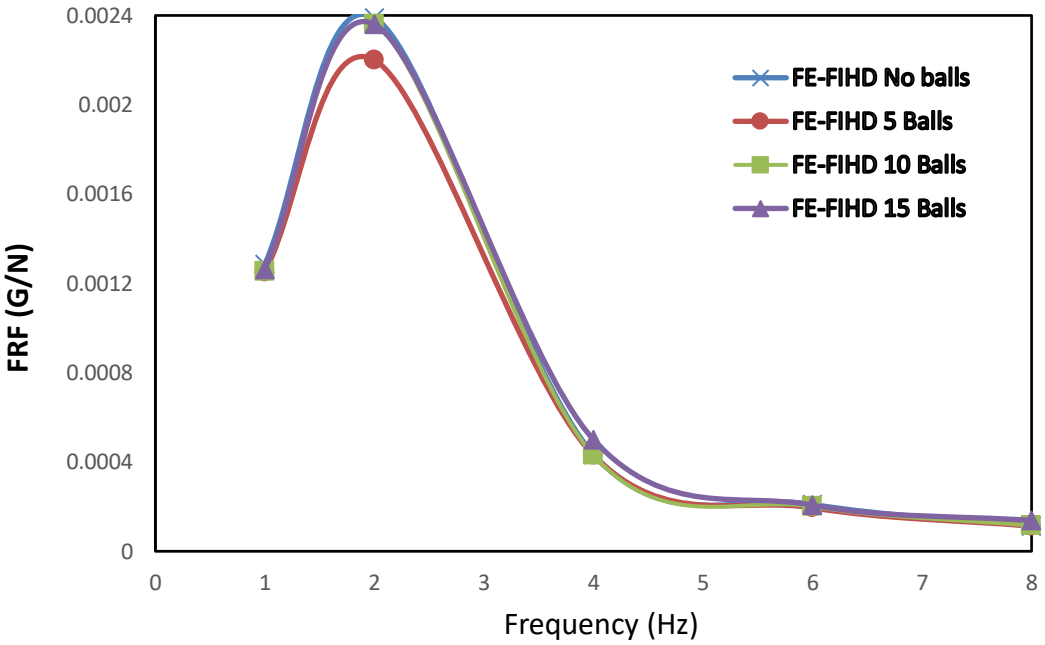

Figure 43**.** Numerical parametric study FRF fitting curve.

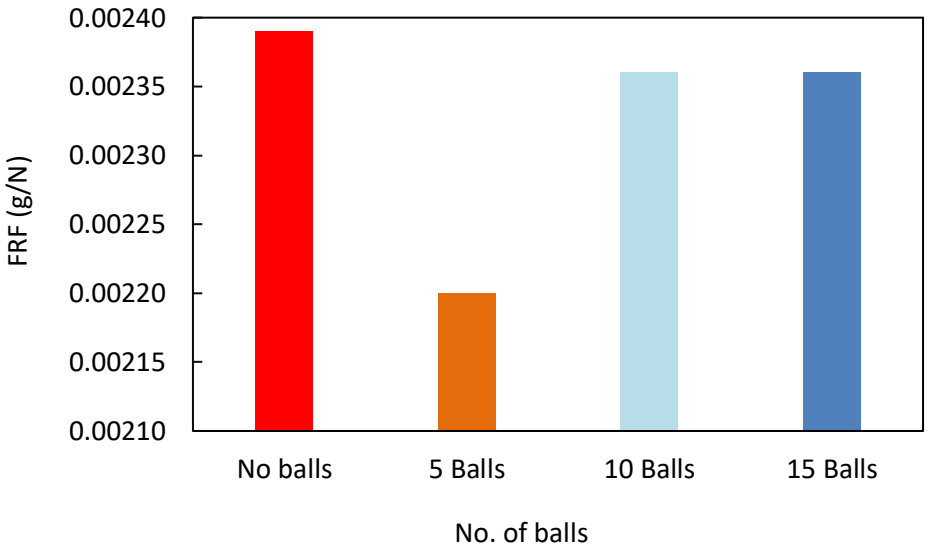

Figure 44. Numerical FRF values at 2Hz.

The bar chart illustrated in Figure.44 shows the amount of FRF value with respect to the number of balls used in the FIHD. As can be seen, using 5 balls results in a significant reduction in the FRF value of 6% at 2Hz, while using 10 and 15 balls

contribute to FRF reduction of less than 2.5%. Along with the PIDs' facts reported in the literature [14], the damping value of the PID is independent of the particles' mass, size, and number. In contrast, the damping value of PID depends on the compromise between the coefficient of restitution and the coefficient of friction. Moreover, providing a suitable empty space for the particles inside the enclosure associated with its size may help in generating more collisions, and hence more damping is obtained.

4.1 FIHD Experimental Work

The basic concept in the construction of the FIHD consists of combining a standard VFD to a PID. Therefore, a well-designed container that encloses the balls and facilitates their inter-collisions is needed. That box was designed to serve as an outlet for the release of destabilizing energy. For operational and manufacturing convenience, such a container should be cylindrical to allow the colliding balls to move freely inside the enclosure space and expel their undesired energy during the structure's motion. As portrayed in Fig 45, the PID box could be joined to the VFD structure in two possible locations: around the main body of the damper or the moving rod. However, as discussed in the literature [15] and practically noticed and confirmed during our first laboratory experiments, the most suitable location for most energy exchange is where the balls attain their maximum velocities. Therefore, the b-configuration (Fig.45-b) was implemented in this investigation.

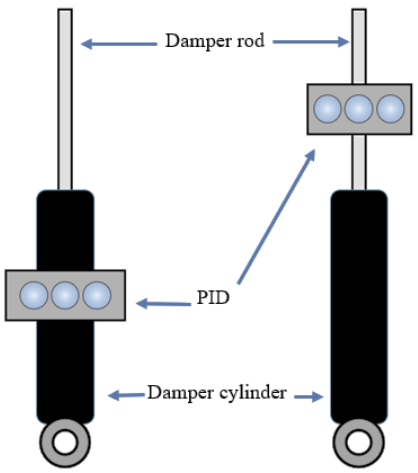

(a) (b)

Figure 45**.** FIHD design consideration: (a) The PID attached to the cylinder wall (b) The PID attached to the damper rod

The FIHD manufacturing and testing were conducted in many stages. First, a viscous damper was dismounted, adjusted, and tuned. Then, a PID was designed, 3D printed and assembled to the fluid damper rod. Finally, a test apparatus was built and used to characterize the dynamic behavior of the hybrid damper. Each of the previously mentioned processes will be addressed in a sufficient way in the following sub-sections.

4.1.1 Viscous Damper preparation

Using the shaker in exciting the hybrid damper with small amplitudes was the first intention of the FIHD experimental setup. Therefore, the viscous damper force has to be decreased to a certain level below the max shaker output (400N). This could only be conducted by changing the oil of the monotube cylinder chamber with low viscosity of the oil. In the beginning, two possible types of hydraulic oil were nominated as damper oil substitution; Brake fluid and Steering oil. In order to know which one is better, a small comparison study was conducted based on their main properties. The two types of oils are ISO 32, ISO 46, and ISO68. In contrast, steering oil has a high-temperature boiling point and a high tendency of compressibility than brake oil. All of the previous characteristics besides steering oils' low viscosity value of (0.028 Pa.s) made it a better damper oil substitution. The evacuation process took place by drilling a small hole (5mm) through the outer shell of the piston-cylinder to the inner walls of the oil chamber. Then a hard carbon steel nozzle with (5mm diameter) was attached to the hole using adhesive epoxy glue and gum tape to avoid oil leakage. Moreover, to prevent ending up with trapped air bubbles inside the damper cylinder, vacuum pressure (-15 psi) was created inside the cylinder. A vacuum pressure pump was used to conduct such a process (Pump type) (Fig.46). Eventually, a feeding tube was connected to the nozzle from one end and to the oil container from another end. Consequently, due to vacuum

pressure inside the cylinder, the oil flows smoothly to the inside damper cylinder.

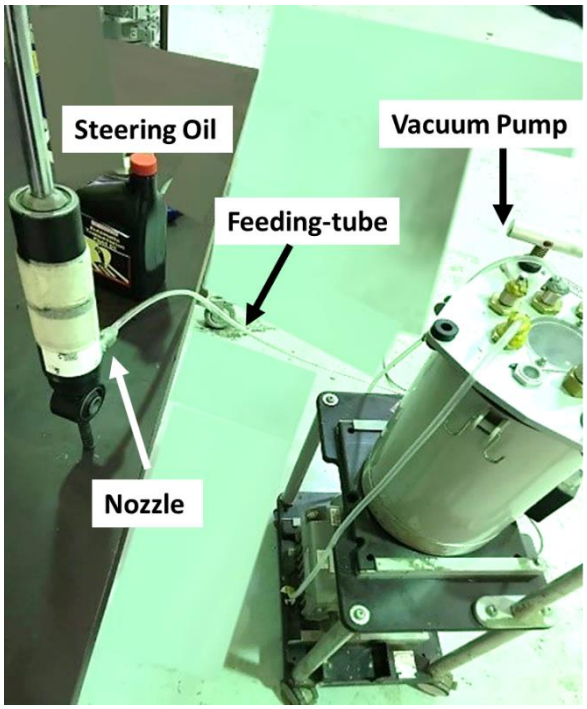

Figure 46. Replacing damper oil process

The previous manufacturing phase of the VFD is mainly focusing on limiting the possibilities of generating cavities and air bubbles inside the damper cylinder.

4.1.2 Particle Impact Box

The PID box was secured to the 16-mm diameter moving rod. The box height was set at 2.5 cm to avoid obstructing the movement of the rod of the VFD during the compression and extension strokes. For a future parametric study of balls number, the box inside the space was designed to receive a total number of 40 balls of 15 mm diameter each. Figure 47 (a) illustrates the 3D geometry of the particle impact box created using SolidWorks ®. Based on the preliminary drawings, the box was 3D printed from Acrylonitrile-Butadiene-Styrene (ABS) material, as shown in Figure

47(b).

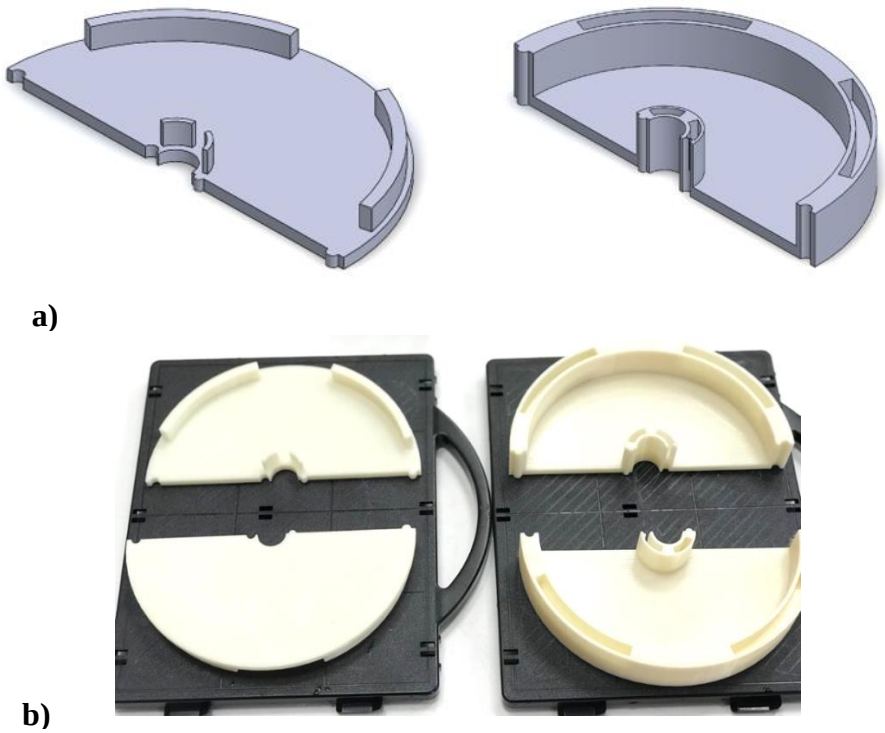

Figure 47. PID box: (a) 3D geometry, (b) 3D printed box

4.1.2.1 PID balls

15 mm diameter Stainless Steel 440C balls (Fig. 48) were used in filling the FIHD box. The material (SS440C) characteristics illustrated in Table 10 [84] govern the amount of vibration energy dissipating when the collisions take place, as is going to be shown in the results section.

Table 10. PID ball Mechanical properties

Balls Material	**Description**	**Density**	**Strength**
Stainless Steel 440C Series	corrosion resistance and toughness	27.68 g/cm3	370-460 MPa Mpa

Figure 48. Stainless steel bearing balls

4.1.3 Shaker test apparatus

The experimental setup was designed to drive the damper into a reciprocating motion with a controlled frequency (Fig.49). The harmonic motion was set by connecting a 3 V amplitude sine wave provided by a signal generator to an amplifier and a shaker input portal. The shaker Model 2100E11 TMS, with maximum output force 440-N. All the devices used in this experiment are shown in Fig.49. To secure a stable position of the damper, its body was mounted between the two jaws of a vice, itself fixed on a heavy metallic bench. A dual force-acceleration sensor, Model 288D01, was installed between the damper rod and the shaker stringer. The signal generator was set to generate a sine wave with 3V amplitude and send it to an amplifier with 24dB gain.

Shaker Model 2100E11 TMS

Signal generator SDG 1000

Accelerometer Model 288D01

Figure 49. Testing setup devices.

Once the system is correctly installed in a vertical and stable position (Fig.50), the piston rod is driven vertically into a sinusoidal motion. The sensitivity range of the data acquisition system was set to 10.2 (mV)/(m/s²) for the sensor acceleration channel and 22.4 mV/N for the force channel. Five different excitation frequencies were considered, namely 1, 2, 4, 6, and 8 Hz. Above 8 Hz, it was observed that the VFD was not able to move, even at low displacement amplitude (less than 0.5 cm). Although the PID, when considered independently, can give effective vibration attenuation performance within a wide frequency band of 0 to 6000 Hz [14], it was observed that the understudy VFD was not able to move, even at low displacement amplitude (less than 0.5 cm).

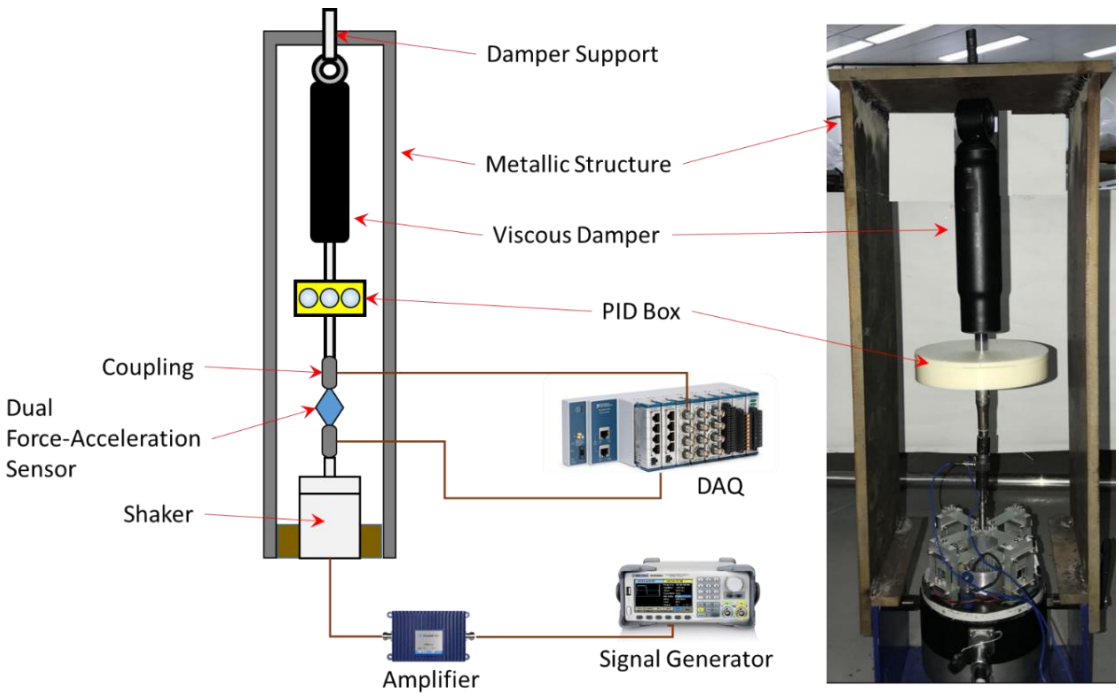

Figure 50. FIHD experimental setup.

As a first parametric investigation, the FIHD was emptied from its balls and tested over the whole frequencies range. Secondly, the FIHD was filled with a set of 15-mm diameter Stainless-Steel balls. Such stainless-steel, 440C series, was used because of its good hardness, dimensional stability, corrosion resistance, and toughness properties. The parametric study contains three sets of ball numbers, namely 5, 10, and 15. The case of 15 balls was the maximum number that provided correct spaces between balls.

4.1.4 Experimental Results

The response amplitude does not depend only on the size, number, and material of the balls but also on their kinematic conditions (initial positions and velocities). Consequently, a higher speed would generate a higher excitation force, which in turn would cause a higher response amplitude, even when the number or the size of balls is small, which could be misleading, especially for a novice user. To investigate the

effects of the essential experimental parameters (number, size, and material of balls) on the damping mechanism, independently from their initial kinematic conditions, the Frequency Response Function (FRF) must be considered.

- *Parametric study Results*

Dual force-acceleration sensor recorder both the force and the acceleration of the moving rod. A sample result of the time-domain results for damper rod's acceleration is displayed in Fig. 51 when no-balls fill the PID box.

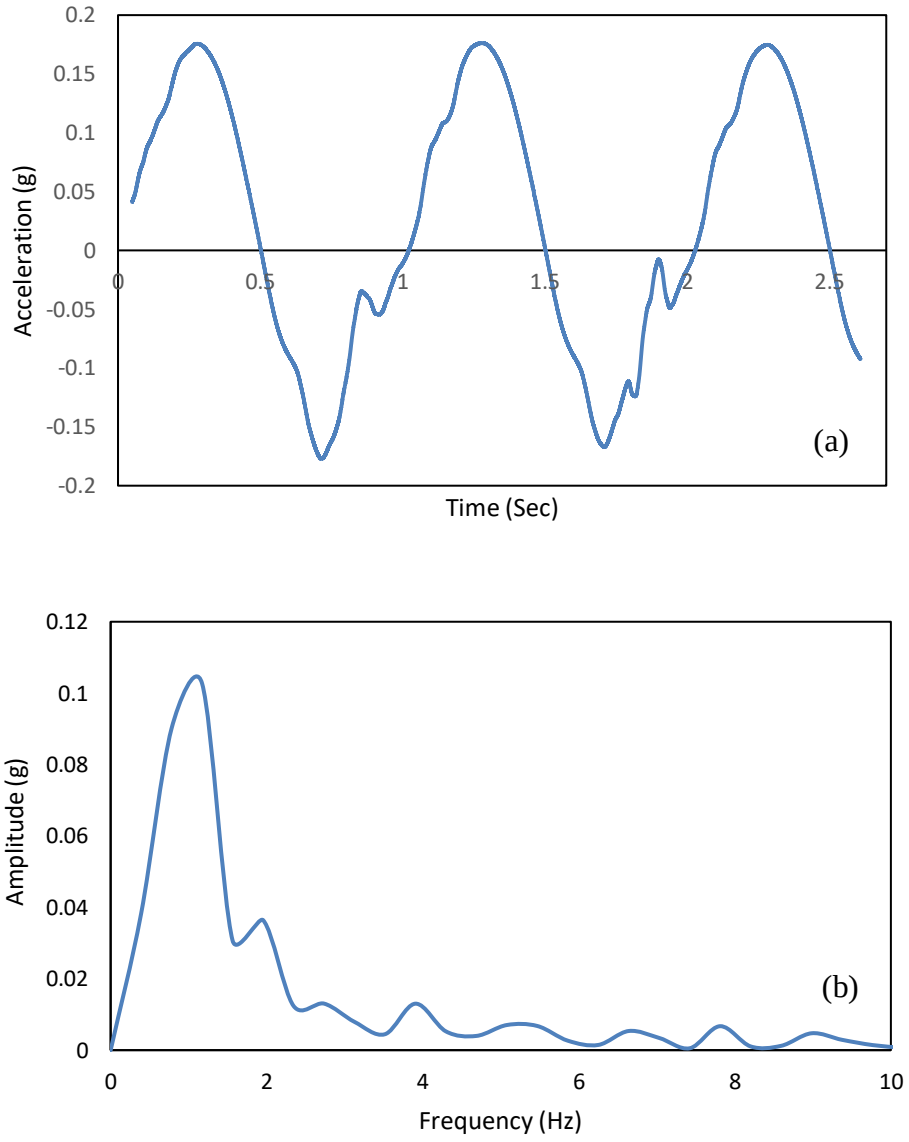

Figure 51. Experimental sample result of acceleration at 1 Hz; (a) Time response (b) Frequency response.

As shown in the numerical results section, FRF was obtained using the MATLAB vibration data analysis tool. The input force, in this case, is the recorded signal coming only from the force-portal of the dual sensor. The FRF parametric study of FIHD, when the PID box is empty and filled with a different number of balls, is presented in Fig.52 & Fig.53.

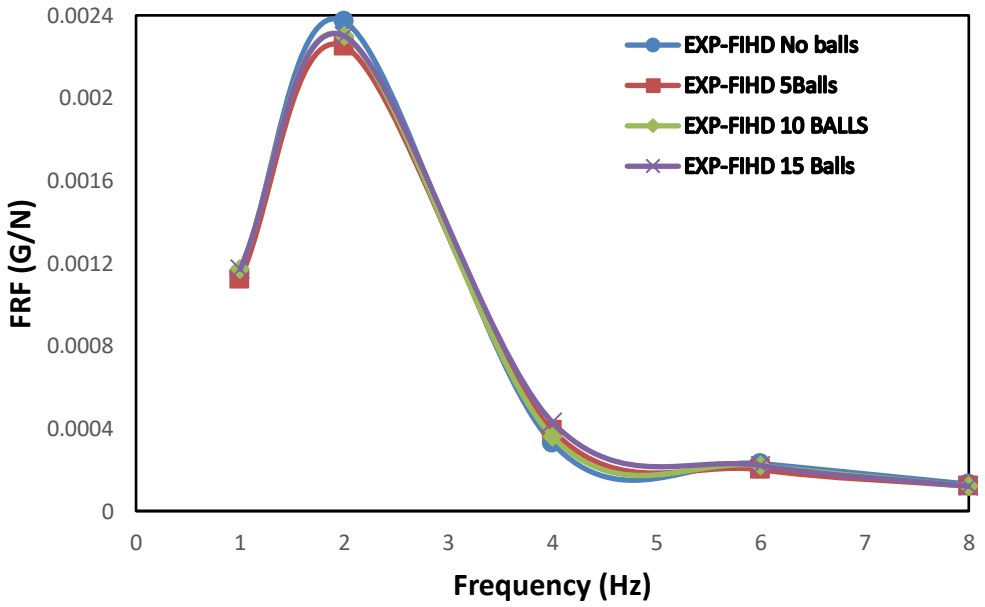

Figure 52. Experimental parametric study on FRF fitting curve

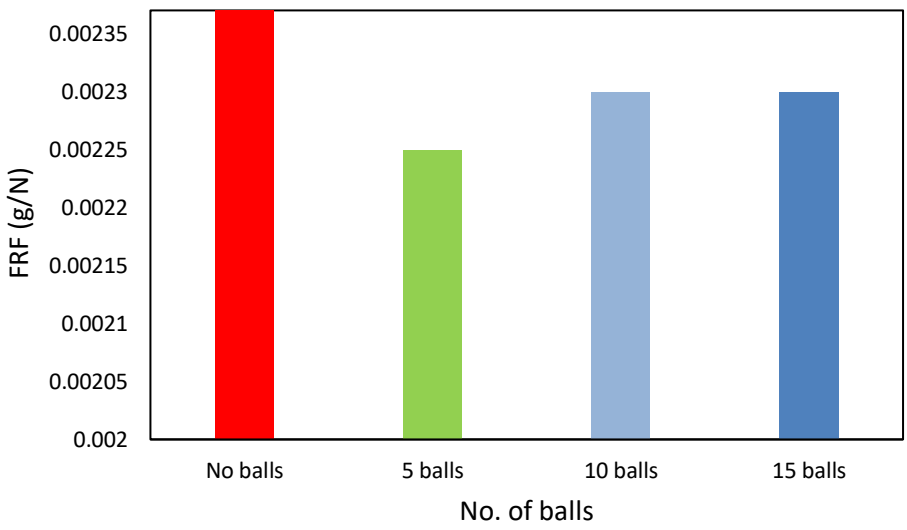

Figure 53. Experimental FRF values at 2Hz.

- *Numerical model validation with the experimental results*

FIHD went through a verification process (Chapter 3) in which its numerical model natural frequency was compared with the analytical one. Furthermore, for the sake of testing the numerical model accuracy, both its experimental and FE simulation acceleration time responses corresponding to 1-Hz were compared (Fig. 54). Based on the displayed acceleration time responses, one can see that the FEM is nearly matching everywhere with the experimental ones. In contrast, a small dissimilarity between the two results can only be seen in experimental bumps, which developed from imperfections in the design of the VFD.

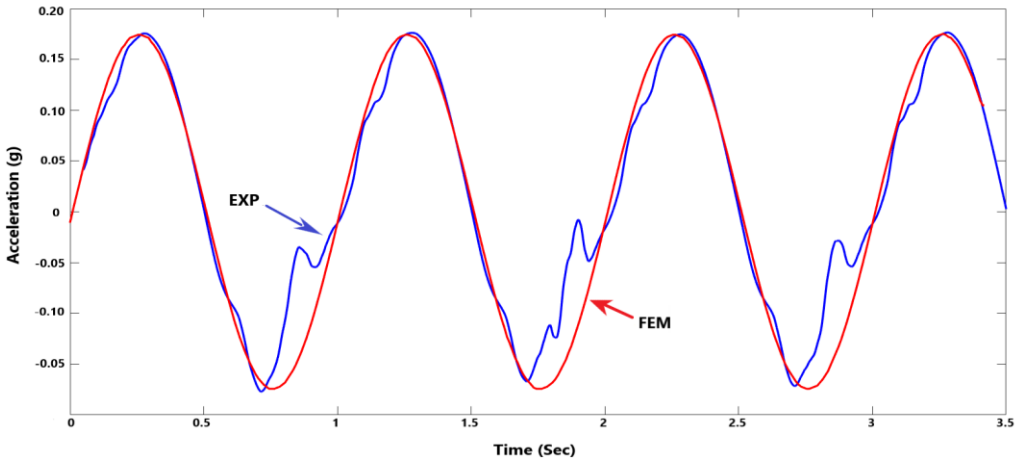

Figure 54**.** Comparison between the experiment and the FEM acceleration time response for 1-Hz acceleration.

To visualize the discrepancy between numerical and experimental results, three different cases are displayed in Fig.55. Each one of the numerical FRF of the parametric study is compared against its similar experimental ones. Although a good agreement is observed between both sets of results, a slight discrepancy could still be noticed around 2 Hz and 4Hz.

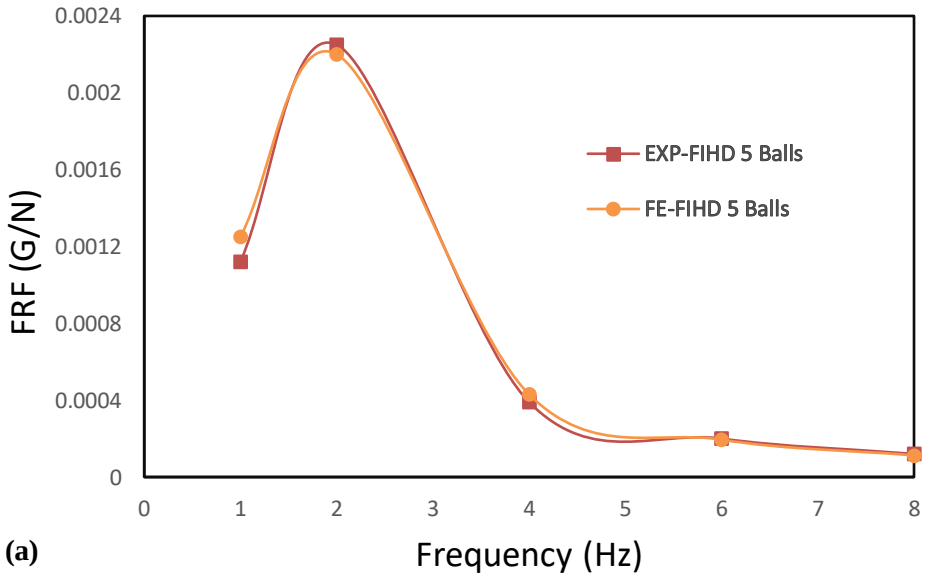

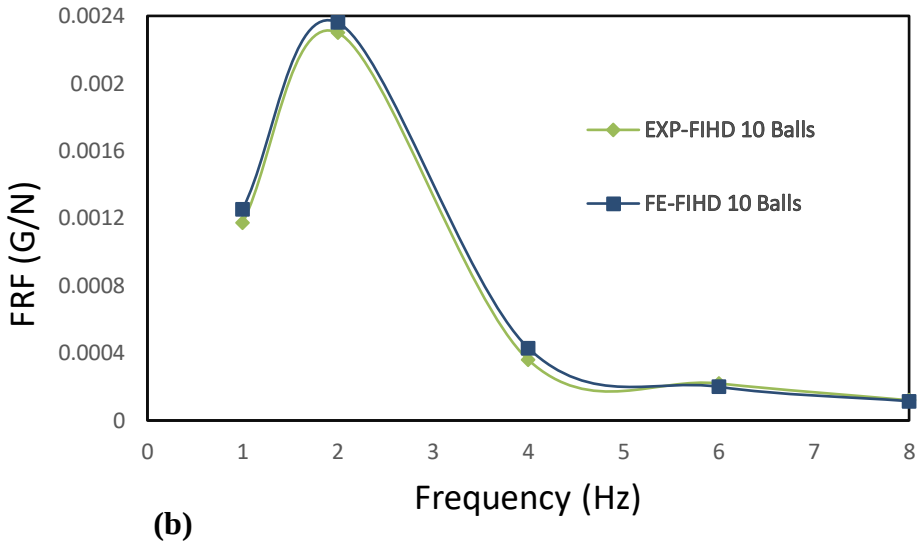

(b)

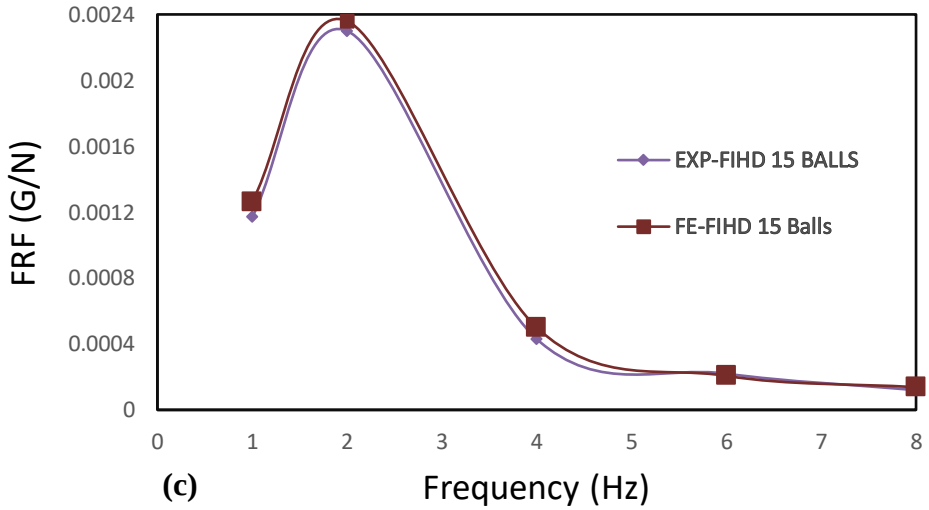

(c)

Figure 55**.** Comparison between the experimental and the numerical FIHD FRF results; (a) five balls, (b) 10 balls, and (c) 15 balls

In order to quantify the errors and ascertain the accuracy of the FE model, Table 11 highlights the dissimilarity between experimental and numerical results at 2 and 4 Hz for the different cases.

Table 11. The FRF amplitude variation between experiment and FEM at 2 and 4 Hz

Parametric study	**2 Hz**			**4 Hz**		
	EXP (g/N)	FEM (g/N)	Error (%)	EXP (g/N)	FEM (g/N)	Error (%)
5 balls	2.25×10^{-3}	2.20×10^{-3}	3	3.9×10^{-4}	4.3×10^{-4}	9
10 balls	2.30×10^{-3}	2.36×10^{-3}	2.8	3.6×10^{-4}	4.3×10^{-4}	16
15 balls	2.30×10^{-3}	2.36×10^{-3}	2.7	4.3×10^{-4}	5.0×10^{-4}	14

4.2 MRF Damper experimental work

The MRF damper of this study basically consists of a classical fluid damper connected to an excitation system. The viscous fluid damper cylinder was divided into two pieces and assembled through a male-female screwed groove. This modification allows replacing the viscous oil with the magnetological fluid. In addition, The magnetic field excitation systems were manufactured through three different work packages. Each work package was assigned to the manufacturing and delivery of one component of the magnetic excitation system. Furthermore, the following subsections will present the manufacturing process and the new design features considered in this work.

4.2.1 Core manufacturing

In order to amplify the magnetic flux density and coils inductance, a ferromagnetic core made from mild steel has to be used along with the copper coils. Although the design of the core was built on the core design used in [46], the new enhancement featured was considered to increase the system output magnetic capacity. The differences between the old and the new design are shown below:

- ✓ The core inner diameter was 1mm less using a CNC lace machine, which

enables more coils to be turned around the core circumference.

- ✓ The core outer edge was processed using an EDM machine to have a surface finish in a half-moon shape to fit the excitation system's ring internal circumference.

The 3D drawing of the core is conducted using SolidWorks 2020, as illustrated in the below figure (Fig.56).

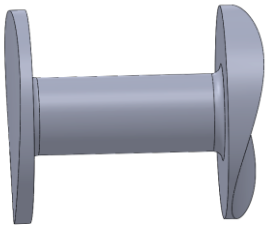

Figure 56 Core 3D drawing.

The 2D drawing of the core with its dimensions is clearly illustrated in Appendix A.

4.2.2 Plastic coil holder and metallic ring

The core's holder was designed to include the 12 cores in its body. The holder design was based on the one developed in the previous study [46]. In contrast, small connecting wire passages were made to provide a compactable space for the surrounding ring. The holder 3D drawing and is shown in Fig.57(a), which was further transformed to STL form for conducting the plastic model using a 3D printing machine.

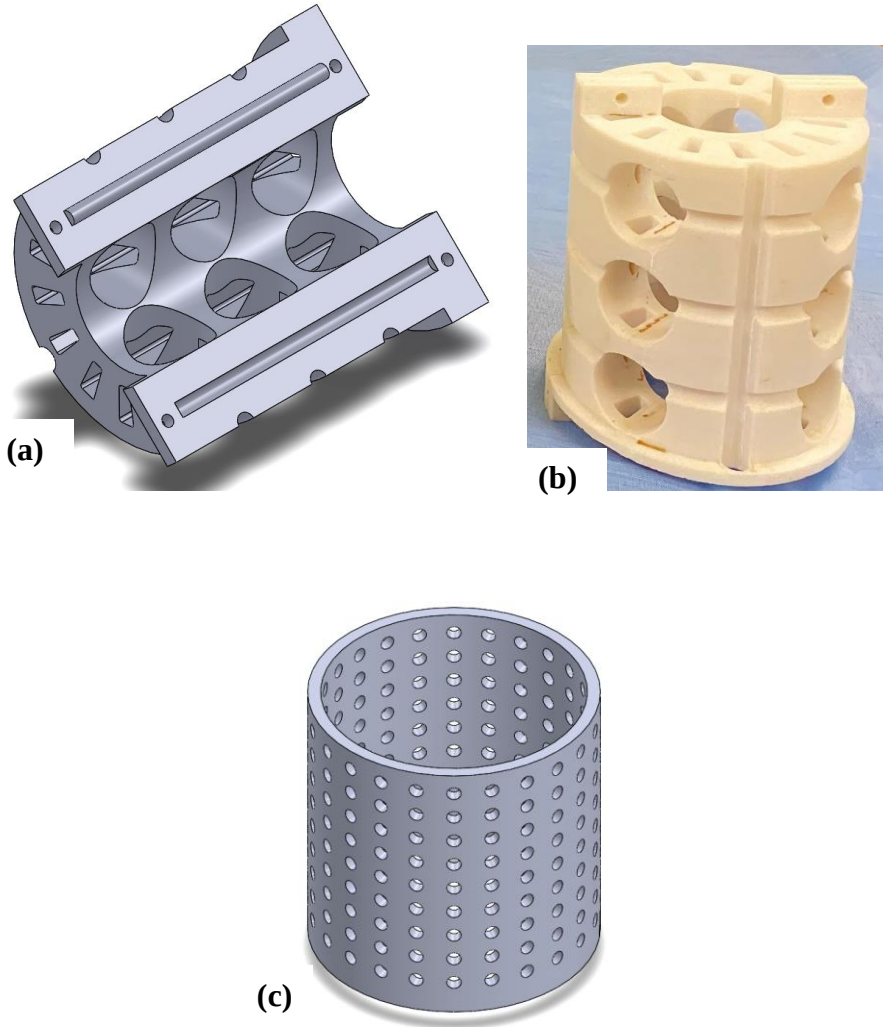

Figure 57 Excitation system holder: (a) Core holder 3D drawing, (b) 3D printed plastic holder, (c) Surrounding ring.

The coils were turned using a wounding machine similar to the lace machine. The total number of turns was 170 turns using 18 AWG copper wire with a 1mm diameter. The following figure (Fig.58) shows the excitation system parts, arrangement, and the two surrounding rings of the parametric study addressed in the previous chapter (Chapter 3).

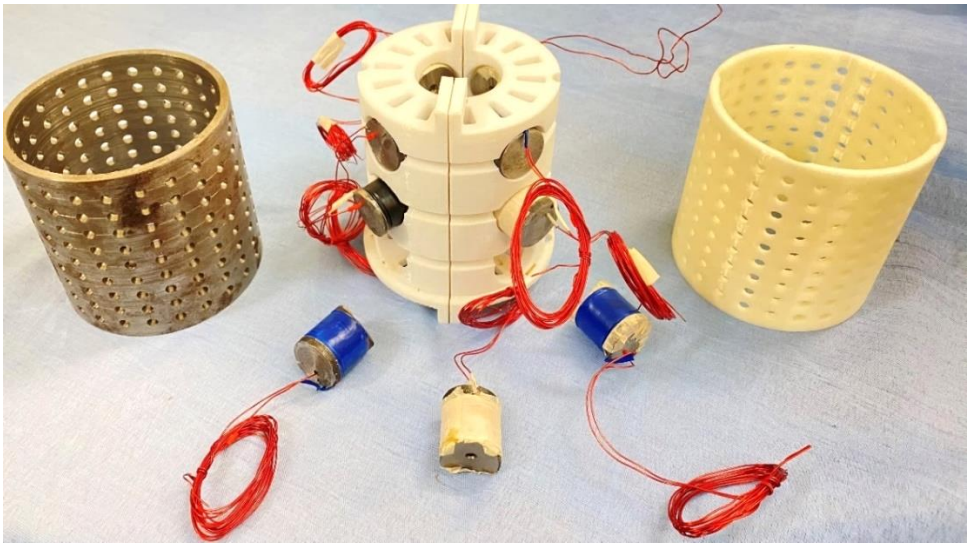

Figure 58. Magnetic field Excitation components.

4.3 The effect of the magnetic field on the MRF viscosity

The CFD numerical model illustrated in Chapter 3 required knowing the change of the viscosity value with the magnetic field. Furthermore, the finding of this section was used as one of the CFD model boundary conditions. In order to know the relationship between the MRF viscosity value and the applied magnetic field density, two stages procedure should be adopted. Firstly, the MRF damper's excitation system should be investigated to identify the relationship between; applied current and the magnetic field density. Secondly, the viscometer test should be adopted to detect the change of the MRF viscosity value with the magnetic field density. This two steps procedure will be discussed in the following sub-sections.

4.3.1 Magnetic field measurements

In the understudy MRF excitation system, different pole arrangements were investigated, and the best performance was found to be obtained when two neighboring poles had opposite charge signs, as shown in 59 (b).

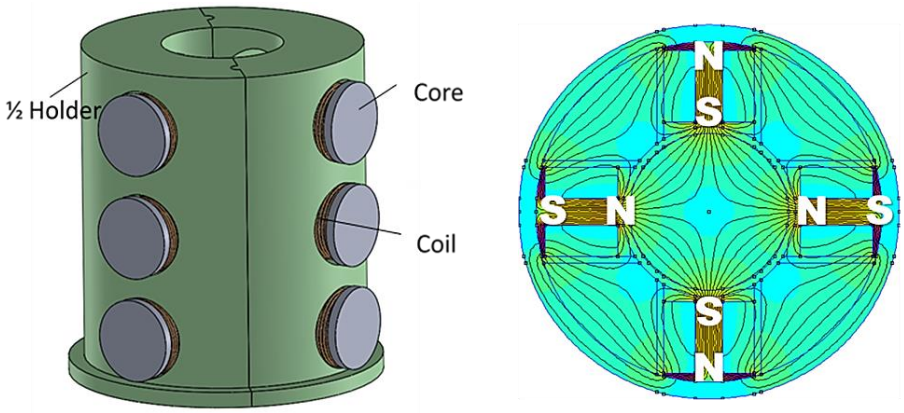

(a) (b)

Figure 59. Magnetic excitation system (reproduced from [46]).

Usually, the change in the magnetic flux density could be measured when the excitation current is varied. The magnetic flux density is recognized as:

$$B = \mu N I \qquad (21)$$

Where μ is the magnetic permeability of the core, N number of turns in the coil, and I is the excitation current.

The magnetic flux density was measured using the previously described excitation system and a Gauss meter, as in Figure 60. The twelve cores were connected to a power supply in a particular arrangement that matches the requirements specified in [46]. The meter needle was placed at a reference point located precisely in the center of the core holder. As the center is the most distant point from the cores (circumference), the reading taken at that point may have the minimum value of flux density because of the low air permeability.

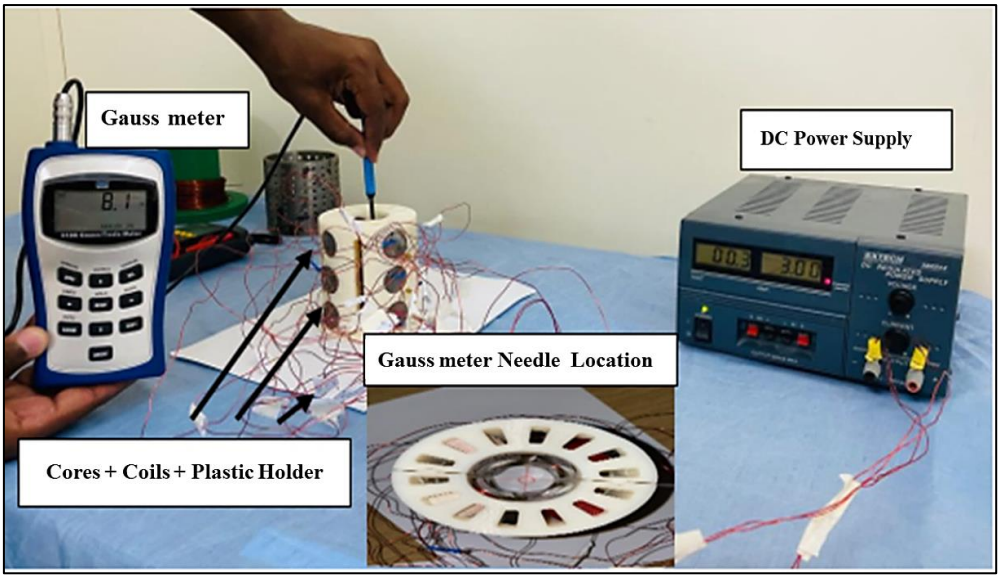

Figure 60. Measuring the magnetic flux density.

The excitation current was periodically increased, from 0 A to 5 A, with a 1 A increment. The magnetic field density value corresponding to each current value is shown in Fig.61.

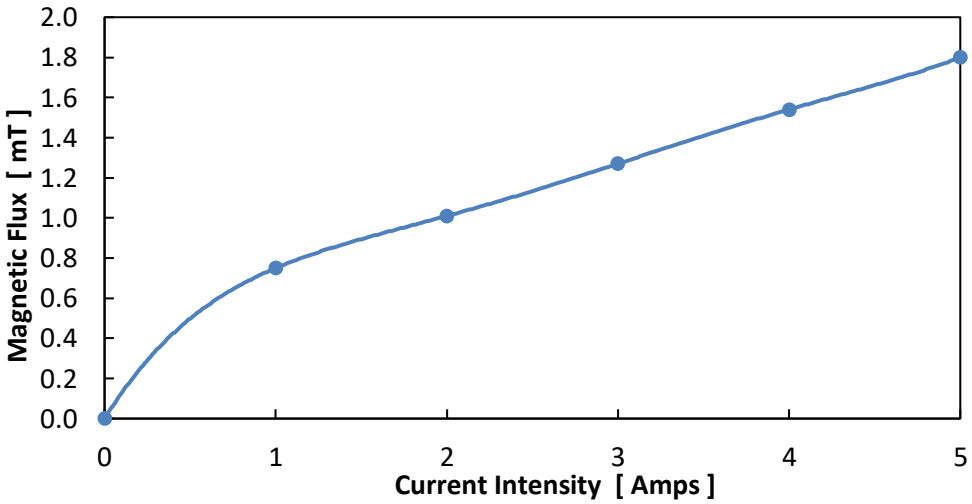

Figure 61. Magnetic field density values at the center point.

4.3.2 Viscometer setup

The viscosity value depends on the dependent yield stress value (τ_b), which varies as the magnetic (B) value changes. Based on previous experimental results, fourth-order fitting curve equations were developed to obtain a relationship between the applied (B) and the value.

$$\tau_b = 39.7B^4 + 119.1B^2 + 10.3\,B + 0.1 \qquad (22)$$

For the understudy MRF 132DG, its characteristic was investigated previously by [37], to obtain a relationship between its shear stress (τ) and the applied (B) value as shown in equation (23) below

$$\tau = 52.962B^4 - 176.51B^3 + 158.79B^2 + 13.708B + 0.1442 \qquad (23)$$

The obtained stress value is used along with the Bingham plastic model to conduct the corresponding dynamic viscosity value (equation 24).

$$\mu = \frac{\tau_B}{\gamma} + \mu_0 \qquad (24)$$

where μ is the dynamic viscosity, τ_B is the dependent magnetic yield stress, γ is the shear strain, and μ_0 is the fluid viscosity in the absence of a magnetic field.

Rotational viscosity meters are devices that provide dynamic viscosity values by measuring the required torque to rotate a spindle with a known RPM inside a fluid container [85]. Usually, a viscosity meter device consists of a motor, spindle, motor controller, rotational motion sensor, and force sensor. The spindle rotates inside the fluid container, forcing the fluid to move accordingly, generating essential torque. By measuring the force at the oil reservoir outer cylinder, spindle RPM speed, and knowing the distance from the axis of rotation, the dynamic viscosity is obtained using equation (1) in Ref [85]. The advanced viscosity meter used in this study is conducting the

viscosity value regarding the torque and RPM velocity of the spindle. The only difference here is that torque and RPM are measured using a servo system. The servo system determines the required current for moving the spindle inside the fluid with set speed. When set a velocity to the spindle the fluid started to decrease its velocity, that's when the servo system determined the required extra current needed to contain the same rotation speed. For testing the viscosity of the MRF 132DG, a unique setup has been developed using the Viscosity meter (Viscometer 2300 RV) (Fig.62).

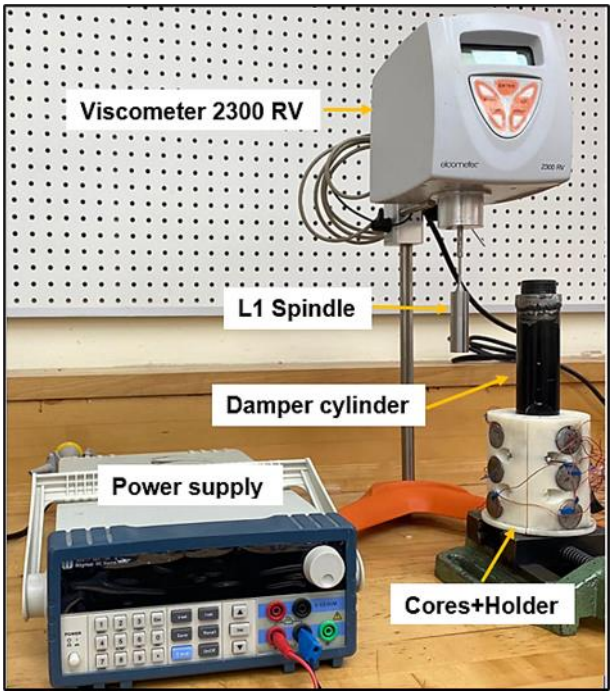

Figure 62. Viscometer experimental setup.

Viscometer comes with different spindles types regarding the viscosity range under study and its desired resolution. Spindle L1 was used to examine the MRF 132DG viscosity under different magnetic flux values. The L1 spindle has a minimum recording value of (1mPa.S) and a range of viscosity values (30-20000) mPa.s. Using a glass container to test the fluid's viscosity may decrease the magnetic field effect,

hence the error in viscosity value. Viscous damper's steel cylinder was used as a container, and cores were placed around it, as shown in Fig.62. The spindle (L1) goes inside the cylinder, and the viscosity meter starts measuring viscosity values corresponding to each excitation current applied.

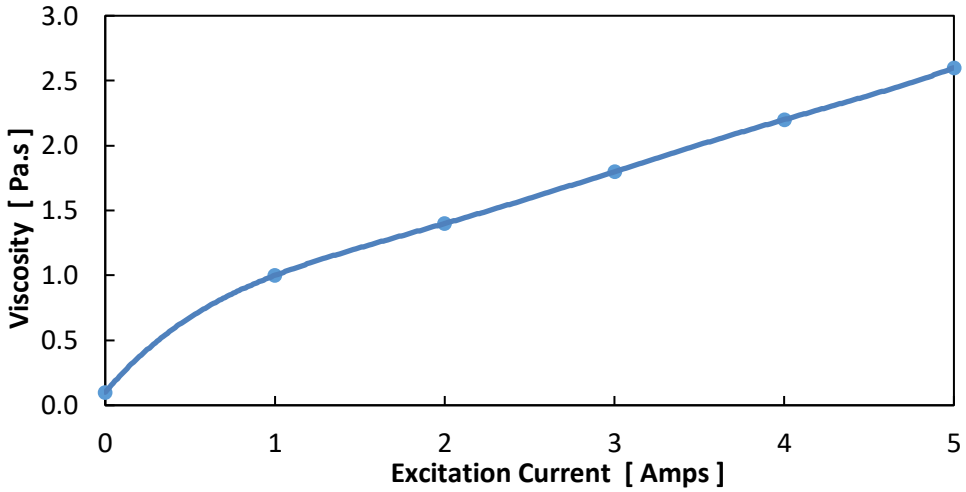

Figure 63. MRF viscosity reading vs. applied current.

Depending on the results displayed in the above figure (Fig.63), viscosity values could be predicted for (I) current value. Hence, a second fitting curve equation (R^2 =0.95) is presented below, which was found using excel statistical regression tool.

$$Viscosity = -0.0446\, I2 + 0.6946\, I + 0.1893 \quad (25)$$

4.4 MRF DAMPER EXPERIMENTAL SETUP

4.4.1 Released weight

As mentioned before, the MRF CFD model results will be compared with the experimental findings mentioned in Sassi et al. study [46]. Therefore, reviewing what has been done in that experiment is essential to find a sort of scientific validation clarifications. However, in the absence of such a machine, the authors decided to load

the damper with different dead weights and record the rod's time travels back and forth, as in Figure 64. Using the travel distance, the time was converted into speed. Consequently, the force and speed relationship was easily obtained for both rebound and compression cycles, as shown in 64(a) and 64(b), respectively.

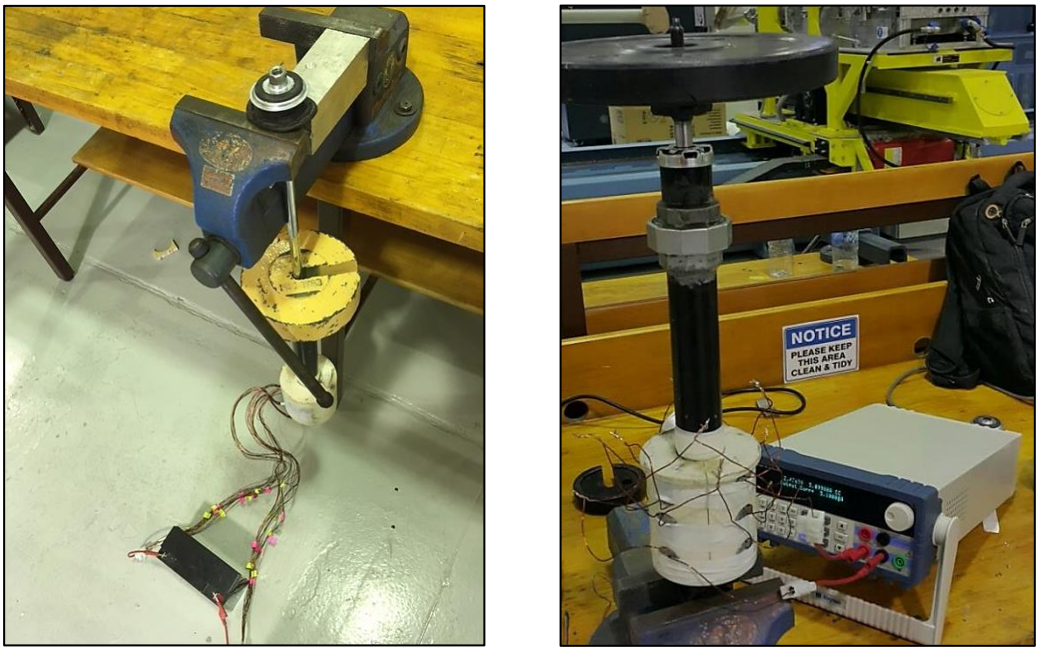

(a) (b)

Figure 64. Experimental testing of the damper filled with MRF; (a) Rebound test; (b) Compression test.

In their approach to measuring the rod's motion speed [46], the mass motion was considered uniform, which was not the case. Indeed, for a falling object, subjected to a resistive force which is proportional to the speed, the equation of motion is of the type:

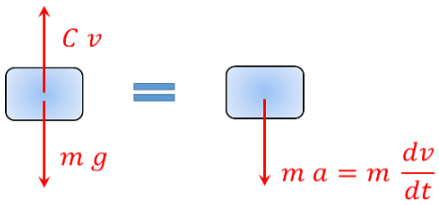

(27)

CHAPTER 5: Conclusion and future work

This study investigated experimentally and numerically the behavior of two dampers; Fluid Impact Hybrid Damper (FIHD) and magnetorheological (MRF) damper. The investigation aims to explore different parameters that affect each damper's damping effect. Moreover, the developed FIHD is a novel type of combination-type dampers introduced for the first time in this study. However, to sum up, the following sub-sections summarized the findings and conclusions of the two dampers' studies.

5.1 Magnetic field numerical modeling

The magnetic field of the MRF damper's excitation system was modeled numerically using Comsol FE- software. All the parts of the excitation system were included in the model besides the surrounding air. Part's material, number of coil's turns, and range of excitation current values (1-5 A) were also considered similar to the real experimental case. However, the main objective of the study was to detect the effect of the surrounding ring's material on the generated magnetic field density and distribution. Based on the magnetic field density 3D contour plots and the 3D line results for the two ring's material of the parametric study, the following was obtained:

- Surrounding the excitation system of cores with a ring made from mild steel will concentrate the magnetic density value at the place of interest. In contrast, using plastic (ABS) will dissipate the magnetic field in a large area around the interest area. In other words, for limiting the magnetic field with a certain area, mild steel with a medium relative permeability value (6000) could be functional. The steel interface shortens the magnetic flux's merging points and allows flux passages.
- Metallic (mild-steel) rings amplify the magnetic field density value by almost 35% than the magnetic density when using plastic (ABS) rings. Although the

plastic ring increases 5% in the magnetic field density compared to the no ring case, the mild steel material is still considered better in amplification.

5.2 MRF-CFD modeling

In this study, a CFD model was used to characterize passive and semi-active MRF mono-tube dampers for different viscosity values over a range of velocity using Ansys 17 Fluent. The CFD model only considers the fluid chamber compressibility and the variation of fluid viscosity. However, the contribution of the internal friction in the damping force was omitted. Based on the obtained numerical damping coefficient values for the two dampers of the parametric study, the following was concluded:

(A) Passive viscous damper

- Increasing the oil viscosity contributes to increasing the damping coefficient, and hence, the damper efficiency.
- For low values of viscosity (0.009 and 0.0139 Pa.s), the damping value increases linearly with the increase in velocity. In other words, using SVI, 3WT suspension oils will probably result in having a linear viscous damper.
- At high velocities (>1.1 m/s), the mono-tube damping coefficient tends to increase nonlinearly regarding the increase in velocity. In addition, the damping coefficient increasing trend when using 5WT oil is nonlinear even for small velocities. Hence, for high-viscosity values (>0.0186 Pa.s), the nonlinear behavior of the damping force is independent of the velocity increases.

(B) MRF damper

1- The MRF damper coefficient increases exponentially as the viscosity value of the rheological fluid increase.

2- For low excitation current values, particularly not exceeding 2 A, the internal friction forces induced to the MRF are insignificant. Therefore, the CFD model results are fairly close to the experimental ones.

3- The discrepancy between the model and the experimental results is significant for high excitation current and hence high magnetic field. The way that experimental results were computed is one of the main reasons for the discrepancy between results. In other words, the travel time of the piston rod recorded using a stopwatch results in a timing error due to human reaction delay in pressing the stopwatch's button.

4- In the absence of friction and cavitation force components, the CFD simulation generates accurate values that fairly match the experimental results. In its actual state, the proposed model is only applicable for magnetic field values that give a viscosity range of 0.1 Pa.s -1.4 Pa.s. These viscosity values are associated with the magnetic field excitation currents ranging from 0A to 2A.

5.3 FIHD conclusion

This study presented the design, construction, and testing of a novel hybrid damper that combines a viscous fluid damper (VFD) and a particle-impact damper (PID) to increase the overall damping of the VFD. The resulting fluid impact hybrid damper (FIHD) was modeled numerically using LS-Dyna and tested experimentally using a custom shaker setup. The effect of the number of balls on the performance of the FIHD was investigated numerically and experimentally. The testing was done using sinusoidal excitations at five frequencies: 1, 2, 4, 6, and 8 Hz. The same excitations were also used in the finite element model to investigate the contribution of the ball-box collisions on

the performance of the PID. The experimental results clearly showed a reduction in the amplitude of the acceleration after adding the PID. Based on the comparison of numerical and experimental FRF results, one can state that:

- In the FIHD response, the FRF showed a maximum peak around the system's natural frequency (2Hz), and the most peak reduction was observed at the same frequency. Since the other frequencies did not satisfy an efficient damping effect, the parametric study focuses on the 2 Hz results.
- LS-Dyna's piecewise linear plasticity material model is applicable for characterizing the collision between stainless steel 440C series balls and (ABS) plastic material box.
- The use of a FIHD with five balls was observed to reduce the FRF peak magnitude by almost 6% for both experimental (5.5%) and numerical (6%) models. Therefore, at 2Hz, the PID contribution in the damping effect can be modeled as two-way contact between the balls-box.
- The FIHD parametric study showed that using more balls (more than 5) does not affect the damping effect. Both numerical and experimental results show that the increase of balls to 10 or 15 did not show an increase in the percentage of peak reduction (less than 2.5%).
- A high error (9% - 16%) between the FEM and the experimental approach results was obtained at 4Hz. Some internal collisions (balls-balls) were observed experimentally at that particular frequency, which was not considered in the FEM investigation. For future work, a discrete element model should be implemented in characterizing the ball-ball collisions.

5.4 Future work

From overviewing the previously mentioned dampers in this study, many research opportunities are opened for further investigations. In order to fill the gaps of each damper's investigation, further research should be focused on the following:

- In hybrid damper's (FIHD) numerical investigation, a discrete element model (DEM) should be implemented in characterizing the ball-ball collisions. DEM will overcome the error that occurred with the FEM by including the contribution of balls' collisions in the hybrid damper's damping effect.
- Rather than studying the magnetic effect of using the surrounding ring of the excitation system, its damping effect should be examined experimentally. Therefore the manufactured MRF damper has to be tested by developing testing apparatus to characterize its damping behavior. In contrast to the previous experiment of a falling mass, the proposed future testing setup will include the MRF damper hysteresis and nonlinear behavior of the Force-Velocity relationship.
- The proposed experimental setup required improving the MRF damper's steady-state CFD model by including the fluid movement. However, the fluid domain movement could only be addressed by creating a User Defined Function (UDF) to the meshing element.
- All the developed numerical models should be adopted in a given application to examine its efficiency related to a specific application. For example, the quarter-car model's damper could be replaced with the dampers' models addressed in this study.

References

[1] K. Li and A. P. Darby, “An experimental investigation into the use of a buffered impact damper,” *J. Sound Vib.*, vol. 291, no. 3–5, pp. 844–860, 2006.

[2] “Chapter 4 PASSIVE CONTROL,” 2001.

[3] L. M. Jugulkar, S. Singh, and S. M. Sawant, “Fluid flow modeling and experimental investigation on automobile damper,” *Constr. Build. Mater.*, vol. 121, pp. 760–772, 2016.

[4] R. Galluzzi, Y. Xu, N. Amati, and A. Tonoli, “Optimized design and characterization of motor-pump unit for energy-regenerative shock absorbers,” *Appl. Energy*, vol. 210, no. August 2017, pp. 16–27, 2018.

[5] Z. Lu, Z. Wang, Y. Zhou, and X. Lu, “Nonlinear dissipative devices in structural vibration control: A review,” *J. Sound Vib.*, vol. 423, pp. 18–49, 2018.

[6] D. I. Narkhede and R. Sinha, “Behavior of nonlinear fluid viscous dampers for control of shock vibrations,” *J. Sound Vib.*, vol. 333, no. 1, pp. 80–98, 2014.

[7] D. I. Narkhede and R. Sinha, “Behavior of nonlinear fluid viscous dampers for control of shock vibrations,” *J. Sound Vib.*, vol. 333, no. 1, pp. 80–98, 2014.

[8] P. Torino, “Experimental determination of viscous damper parameters in low velocity ranges,” no. July, 2017.

[9] R. Greco and G. C. Marano, “A comparative study on parameter identification of fluid viscous dampers with different models,” no. August, 2014.

[10] Y. Badri, T. Syam, S. Sassi, M. Hussein, J. Renno, and S. Ghani, “Investigating the characteristics of a magnetorheological fluid damper through CFD modeling,” *Mater. Res. Express*, vol. 8, no. 5, 2021.

[11] D. Cruze, H. G, S. V. S. Jebadurai, S. L, T. D, and S. S. J. E. Christy, “A Review on the Magnetorheological Fluid, Damper and Its Applications for Seismic

Mitigation," *Civ. Eng. J.*, vol. 4, no. 12, p. 3058, 2018.

[12] "https://www.strutmasters.com/the-difference-between-twin-tube-and-monotube-shocks/#:~:text=Twin%2Dtube%20shocks%20get%20the,stress%20in%20a%20particular%20area.".

[13] R. M. Desai, M. E. H. Jamadar, H. Kumar, and S. Joladarashi, "Experimental investigation and mathematical modeling of automotive passive damper for SUV suspension system," *AIP Conf. Proc.*, vol. 2247, no. July, 2020.

[14] Z. Lu, Z. Wang, S. F. Masri, and X. Lu, "Particle impact dampers: Past, present, and future," *Struct. Control Heal. Monit.*, vol. 25, no. 1, pp. 1–25, 2018.

[15] L. Gagnon, M. Morandini, and G. L. Ghiringhelli, "A review of particle damping modeling and testing," *J. Sound Vib.*, vol. 459, p. 114865, 2019.

[16] M. Gharib and S. Ghani, "Free vibration analysis of linear particle chain impact damper," *J. Sound Vib.*, vol. 332, no. 24, pp. 6254–6264, 2013.

[17] M. Mirtaheri, A. P. Zandi, S. S. Samadi, and H. R. Samani, "Numerical and experimental study of hysteretic behavior of cylindrical friction dampers," *Eng. Struct.*, vol. 33, no. 12, pp. 3647–3656, 2011.

[18] H. V Panossian, "Via Non-Obstructive Particle Damping Technique," *J. Vib. Acoust.*, vol. 114, no. January 1992, pp. 101–105, 1992.

[19] R. D. Friend and V. K. Kinra, "Particle impact damping," *J. Sound Vib.*, vol. 233, no. 1, pp. 93–118, 2000.

[20] G. Jin *et al.*, "Design of a particle damper and experimental study on vibration damping of the pipeline," *Adv. Mech. Eng.*, vol. 13, no. 9, p. 168781402110449, 2021.

[21] J. Chen and C. T. Georgakis, "Tuned rolling-ball dampers for vibration control

in wind turbines," *J. Sound Vib.*, vol. 332, no. 21, pp. 5271–5282, 2013.

[22] S. S. Simonian, "Particle damping applications," *Collect. Tech. Pap. - AIAA/ASME/ASCE/AHS/ASC Struct. Struct. Dyn. Mater. Conf.*, vol. 6, no. April, pp. 4145–4161, 2004.

[23] Y. Badri, S. Sassi, M. Hussein, and J. Renno, "Experimental and numerical investigation of damping in a hybrid automotive damper combining viscous and multiple-impact mechanisms," *J. Vib. Control*, no. July, p. 107754632110381, 2021.

[24] A. M. A. Soliman and M. M. S. Kaldas, "Semi-active suspension systems from research to mass-market – A review," *J. Low Freq. Noise Vib. Act. Control*, 2019.

[25] M. R. Jolly, J. W. Bender, and J. D. Carlson, "Properties and Applications of Commercial Magnetorheological Fluids," *J. Intell. Mater. Syst. Struct.*, vol. 10, no. 1, pp. 5–13, 1999.

[26] L. Vékás, "Ferrofluids and magnetorheological fluids," *CIMTEC 2008 - Proc. 3rd Int. Conf. Smart Mater. Struct. Syst. - Smart Mater. Micro/Nanosystems*, vol. 54, pp. 127–136, 2008.

[27] A. E. Ehret, M. Hollenstein, E. Mazza, and M. Itskov, "Mechanics of Materials and Structures," vol. 6, no. 7, 2011.

[28] N. V. Quoc, L. D. Tuan, L. D. Hiep, H. N. Quoc, and S. B. Choi, "Material characterization of MR fluid on performance of MRF based brake," *Front. Mater.*, vol. 6, no. June, pp. 1–15, 2019.

[29] X. Zhu, X. Jing, and L. Cheng, "Magnetorheological fluid dampers: A review on structure design and analysis," *J. Intell. Mater. Syst. Struct.*, vol. 23, no. 8, pp. 839–873, 2012.

[30] I. Bica, Y. D. Liu, and H. J. Choi, “Physical characteristics of magnetorheological suspensions and their applications,” *J. Ind. Eng. Chem.*, vol. 19, no. 2, pp. 394–406, 2013.

[31] A. Hoyle, S. Arzanpour, and Y. Shen, “A novel magnetorheological damper based parallel planar manipulator design,” *Smart Mater. Struct.*, vol. 19, no. 5, 2010.

[32] J. De Vicente, D. J. Klingenberg, and R. Hidalgo-Alvarez, “Magnetorheological fluids: A review,” *Soft Matter*, vol. 7, no. 8, pp. 3701–3710, 2011.

[33] A. G. Olabi and A. Grunwald, “Design and Application of Magneto-Rheological Fluid,” pp. 1–19.

[34] Ł. Konieczny, “Analysis of Simplifications Applied in Vibration Damping Modelling for a Passive Car Shock Absorber,” *Shock Vib.*, vol. 2016, 2016.

[35] D. Guan, X. Jing, H. Shen, L. Jing, and J. Gong, “Test and simulation the failure characteristics of twin tube shock absorber,” *Mech. Syst. Signal Process.*, vol. 122, pp. 707–719, 2019.

[36] W. H. XIANG Hengbo, FANG Qin, GONG Ziming, “Experimental Investigation into Magnetorheological Damper Subjected to Impact Loads,” *Trans. Tianjin Univ.*, vol. 16, no. 50638030, pp. 81–88, 2008.

[37] Y. Badri, M. Hussein, S. Sassi, and J. Renno, “Investigation of the Effect of the Force-Frequency on the Behaviour of a New Viscous Damper for Railway Applications,” no. CIC, pp. 666–671, 2020.

[38] D. I. Narkhede and R. Sinha, “Shock Vibration Control of Structures using Fluid Viscous Dampers,” *15th World Conf. Earthq. Eng.*, 2012.

[39] M. Masmoudi, S. Job, M. S. Abbes, I. Tawfiq, and M. Haddar, “Experimental and numerical investigations of dissipation mechanisms in particle dampers,”

Granul. Matter, vol. 18, no. 3, pp. 1–11, 2016.

[40] K. Li and A. P. Darby, "Experiments on the effect of an impact damper on a multiple-degree-of- freedom system," *JVC/Journal Vib. Control*, vol. 12, no. 5, pp. 445–464, 2006.

[41] M. Gharib and M. Karkoub, "Shock-Based Experimental Investigation of the Linear Particle Chain Impact Damper," *J. Vib. Acoust.*, vol. 137, no. 6, p. 061012, 2015.

[42] W. Cheng-guo, Q. Lixin, L. Jin-zhao, Z. Wen-zhang, and F. Worth, "A New Shock Absorber Model with an Application in Vehicle Dynamics Studies Richard van Kasteel Meeting and Exhibition," *Engineering*, no. 724, 2003.

[43] K. Li and A. P. Darby, "Experiments on the effect of an impact damper on a multiple-degree-of- freedom system," *JVC/Journal Vib. Control*, vol. 12, no. 5, pp. 445–464, 2006.

[44] R. D. Nayeri, S. F. Masri, and J. P. Caffrey, "Studies of the performance of multi-unit impact dampers under stochastic excitation," *J. Vib. Acoust. Trans. ASME*, vol. 129, no. 2, pp. 239–251, 2007.

[45] B. Betgen, "Assessment of the efficiency of railway wheel dampers using laboratory methods within the STARDAMP project" pp. 671–672, 2012.

[46] S. Sassi, A. Sassi, K. Cherif, and F. Tarlochan, "Magnetorheological damper with external excitation for more efficient control of vehicles' dynamics," *J. Intell. Mater. Syst. Struct.*, vol. 29, no. 14, pp. 2919–2932, 2018.

[47] T. M. G. Hemantha and K. Arun, "An approach for characterizing twin-tube shear-mode magnetorheological damper through coupled FE and CFD analysis," *J. Brazilian Soc. Mech. Sci. Eng.*, vol. 40, no. 3, pp. 1–14, 2018.

[48] G. R. Iglesias, S. Ahualli, J. Echávarri Otero, L. Fernández Ruiz-Morón, and J.

D. G. Durán, “Theoretical and experimental evaluation of the flow behavior of a magnetorheological damper using an extremely bimodal magnetic fluid,” *Smart Mater. Struct.*, vol. 23, no. 8, 2014.

[49] T. M. T. S. Model, “Model 835 System For Testing Small Dampers,” *Test*.

[50] B. Bai and J. Guo, “Finite Element Damping Simulation of Viscous Damper for Simply Supported Beam Vibration Mitigation,” *IOP Conf. Ser. Earth Environ. Sci.*, vol. 525, no. 1, 2020.

[51] F. Edition and B. Raton, “Rheological models of viscoelastic bodies and materials Classical rheological models,” 2007.

[52] A. A. Olędzki, I. Siwicki, and J. Wiśniewski, “Impact dampers in application for tube, rod and rope structures,” *Mech. Mach. Theory*, vol. 34, no. 2, pp. 243–253, 1999.

[53] J. R. Rice, *Fracture mechanics*, vol. 38, no. 10. 1985.

[54] Valentin L. Popov, *Contact Mechanics and Friction*. Springer, 2009.

[55] A. Aryaei, K. Hashemnia, and K. Jafarpur, “Experimental and numerical study of ball size effect on restitution coefficient in low velocity impacts,” *Int. J. Impact Eng.*, vol. 37, no. 10, pp. 1037–1044, 2010.

[56] Z. Lu, X. Lu, H. Jiang, and S. F. Masri, “Discrete element method simulation and experimental validation of particle damper system,” *Eng. Comput. (Swansea, Wales)*, vol. 31, no. 4, pp. 810–823, 2014.

[57] X. Wang, X. Liu, Y. Shan, and T. He, “Design, simulation and experiment of particle dampers attached to a precision instrument in spacecraft,” *J. Vibroengineering*, vol. 17, no. 4, pp. 1605–1614, 2015.

[58] X. De-Kui, N. Song-Lin, J. Hui, and Y. Fang-Long, “Characteristics, Optimal Design, and Performance Analyses of MRF Damper,” *Shock Vib.*, vol. 2018,

2018.

[59] D. Gorman, S. Jerrams, R. Ekins, and N. Murphy, “Magnetic Field Design Reliable Data for Magnetic Field Design in Magnetorheological Elastomer Damping Applications is Essential for Accurate and Cost- …,” pp. 20–22, 2012.

[60] R. Stanway, J. L. Sproston, and N. G. Stevens, “Non-linear modelling of an electro-rheological vibration damper,” *J. Electrostat.*, vol. 20, no. 2, pp. 167–184, 1987.

[61] S. R. Hong, N. M. Wereley, Y. T. Choi, and S. B. Choi, “Analytical and experimental validation of a nondimensional Bingham model for mixed-mode magnetorheological dampers,” *J. Sound Vib.*, vol. 312, no. 3, pp. 399–417, 2008.

[62] T. M. I. Syam and A. G. A. Muthalif, “Hysteresis behaviour of different magnetorheological elastomer models: Modelling and simulation,” *Vibroengineering Procedia*, vol. 31, pp. 7–14, 2020.

[63] M. K. M. Razali, A. G. A. Muthalif, and N. H. D. Nordin, “Estimation of Parameter for Different Magnetorheological Fluids Model for Varying Current” *Int. J. Comput. Electr. Eng.*, vol. 10, no. 2, pp. 127–134, 2018.

[64] “https://en.wikipedia.org/wiki/K-epsilon_turbulence_model.”.

[65] J.-H. Park and O.-O. Park, “Electrorheology and magnetorheology,” *Korea-Australia Rheol. J.*, vol. 13, no. 1, pp. 13–17, 2001.

[66] B. Dyke, SJ and Spencer Jr, *T He Behaviour of Magnetorheological Fluids in Squeeze Mode*, no. August. 1996.

[67] I. Technology, “THEORETICAL STUDY OF A TWIN-TUBE MAGNETORHEOLOGICAL DAMPER CONCEPT Janusz Gołdasz” vol. c, pp. 885–894, 2015.

[68] B. H. T. S. W. D. F. M. H. M. C. A. J. E. P. E. A. Rodriguez, “Concepts of Model

Verification and Validation," *Los Alamos Natl. Lab.*

[69] COMSOL Multiphysics, "AC / DC Module User ' s Guide," *Manual*, p. 300, 2018.

[70] "'How to Inspect Your Mesh in COMSOL Multiphysics® | COMSOL Blog.' [Online]. Available: https://www.comsol.com/blogs/how-to-inspect-your-mesh-in-comsol-multiphysics/.".

[71] X. Jiao, Y. Zhao, and W. Ma, "Nonlinear dynamic characteristics of a micro-vibration fluid viscous damper," *Nonlinear Dyn.*, vol. 92, no. 3, pp. 1167–1184, 2018.

[72] F. H. Harlow, "Fluid dynamics in group T-3 Los Alamos National Laboratory (LA-UR-03-3852)," *J. Comput. Phys.*, vol. 195, no. 2, pp. 414–433, 2004.

[73] "https://www.peterverdone.com/wiki/index.php?title=Suspension_Fluid."

[74] "Gabriel J. DeSalvo and John A. Swanson. (1985). ANSYS engineering analysis system user's manual. Houston, Pa. :Swanson Analysis Systems"

[75] S. Larsson, "Characterization and Modeling of Rock Impact on Steel Plates - Thesis," *Thesis Master*, 2014.

[76] J. O. Hallquist, *LS-Dyna theory manual*. 2006.

[77] F. Irgens, *Continuum mechanics*. 2008.

[78] S. Akcelyan, D. G. Lignos, and T. Hikino, "Adaptive numerical method algorithms for nonlinear viscous and bilinear oil damper models subjected to dynamic loading," *Soil Dyn. Earthq. Eng.*, vol. 113, no. April, pp. 488–502, 2018.

[79] P. K. Samal, J. C. Valko, and J. D. Pannell, "Processing and properties of PM 440C stainless steel," *Adv. Powder Metall. Part. Mater. - 2009, Proc. 2009 Int. Conf. Powder Metall. Part. Mater. PowderMet 2009*, pp. 7112–7121, 2009.

[80] J. Cantrell *et al.*, “Experimental Characterization of the Shear Properties of 3D–Printed ABS and Polycarbonate Parts,” *Exp. Mech.*, vol. 58, no. 6, pp. 871–884, 2017.

[81] A. Seeni, P. Rajendran, and H. Mamat, “A CFD mesh independent solution technique for low Reynolds number propeller,” *CFD Lett.*, vol. 11, no. 10, pp. 15–30, 2019.

[82] J. He and Z.-F. Fu, “Basic vibration theory,” *Modal Anal.*, pp. 49–78, 2001.

[83] Q. Yan and P. Ho, “Introduction to LS-PrePost Table of Contents,” 2018.

[84] *TitleThermophysical Properties of High*.

[85] B. Cherrington and J. Rothstein, “Building and Validating a Rotational Viscometer,” 2014.

Appendix A: Magnetic field numerical modeling results

- *Excitation system component 2D drawing*

The 2D drawings of the MRF's excitation system presented in Chapter 4 are given in the below figures. All the drawings were conducted using SolidWorks2021. Those drawing were further used in defining the solution domain in the Comsol numerical model of the magnetic field analysis.

- *Plastic core holder*

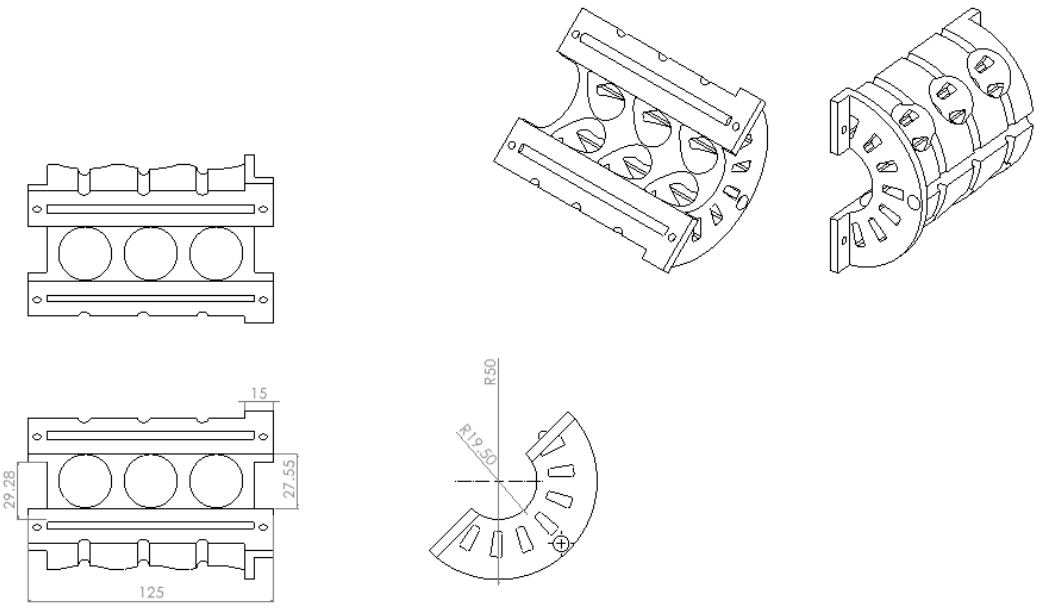

- *Magnetic Core*

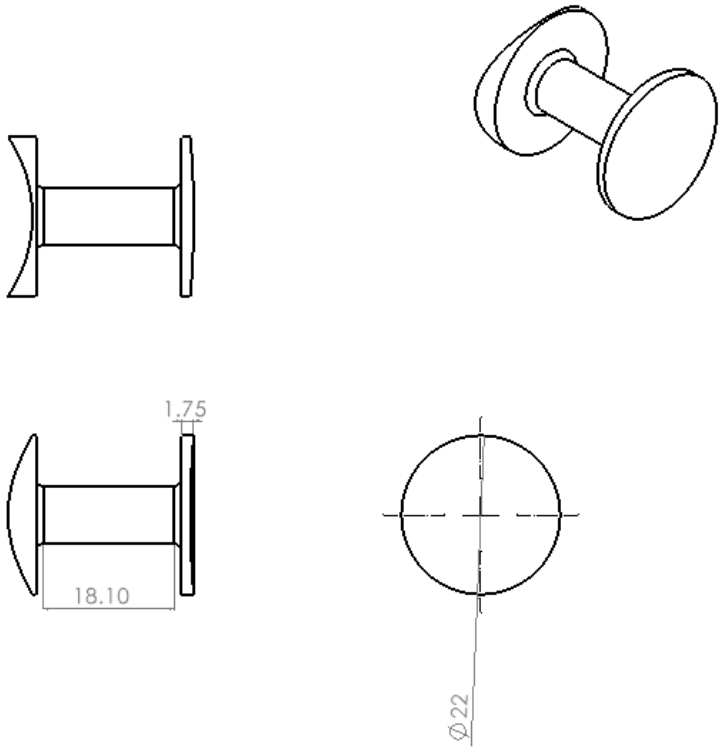

- *Magnetic field density*

A sample result of the magnetic field density was presented previously in Figure. 17-Chapter 3. In addition, magnetic field density's contour plots of the five current values for the two different ring materials (ABS and Mild steel) are shown below.

- *Magnetic field density values when using the plastic ring*

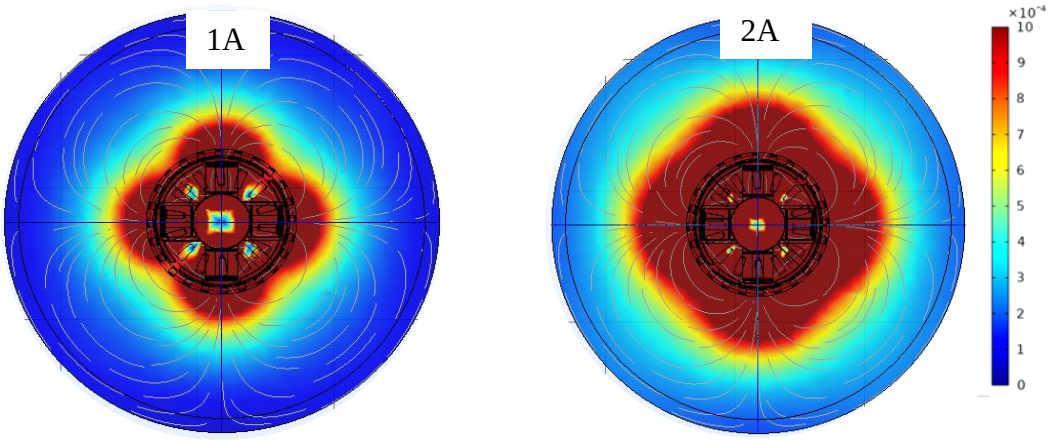

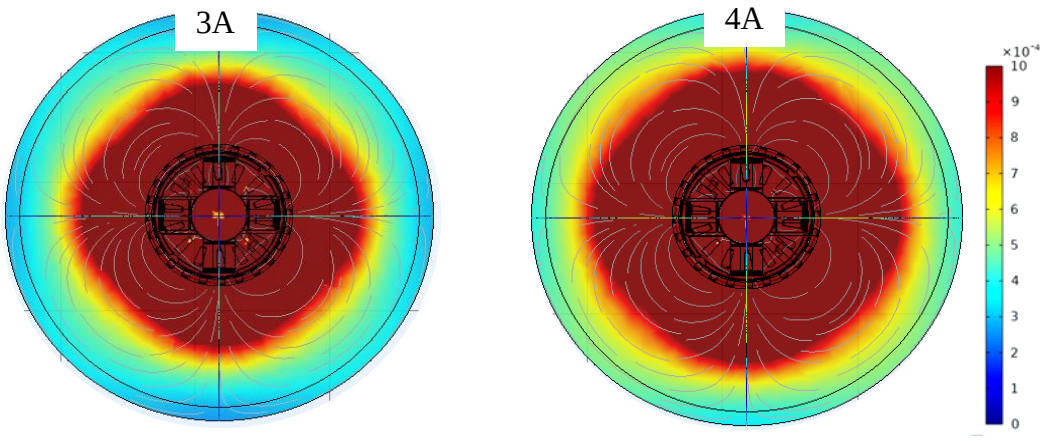

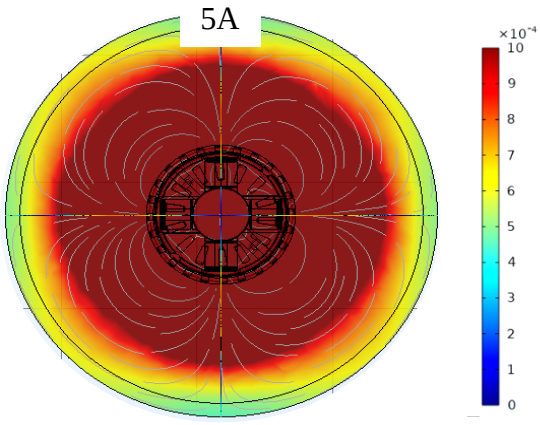

- *Magnetic field density when using the metallic ring*

1A

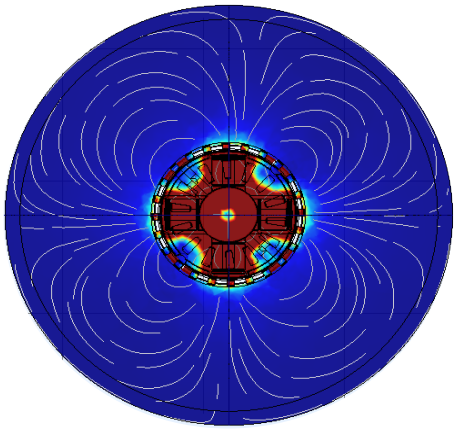

2A

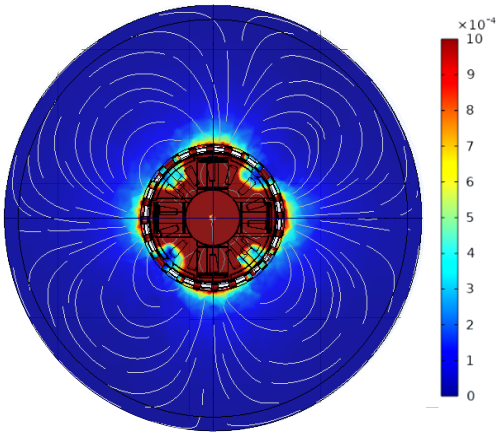

3A

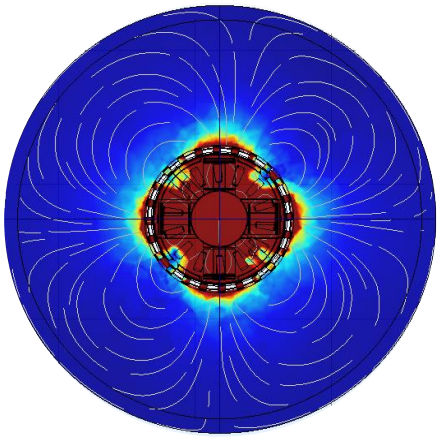

4A

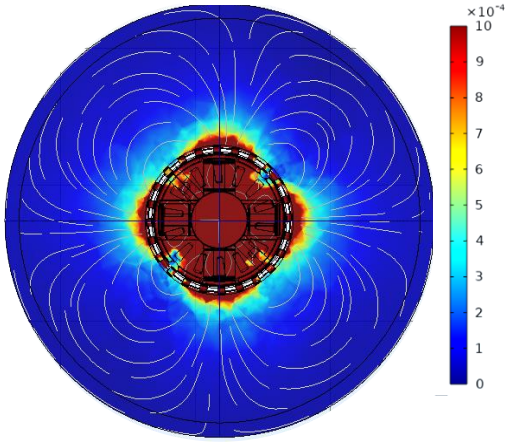

5A

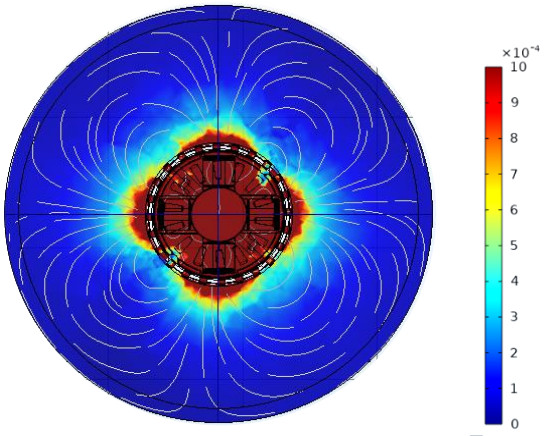

- *Validating the Comsol model through experimental setup*

In order to validate the magnetic field (MF) numerical model, its findings have to be compared against experimental results. Therefore, Gaussmeter is used in measuring the field density value at a reference line located at the center of the excitation system, as shown in the figure below.

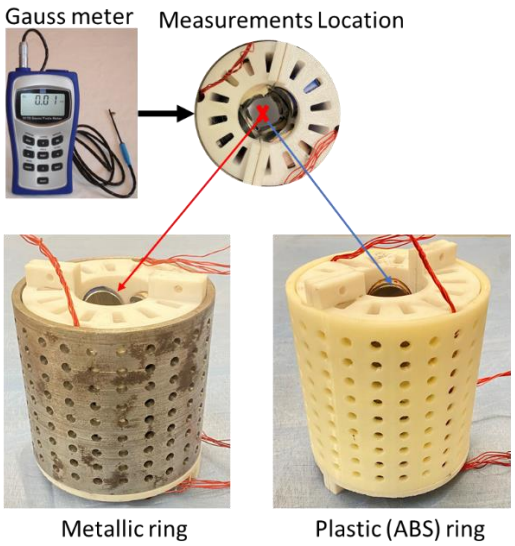

The magnetic field densities in mT recorded at the Gauss meter for the two cases (two ring's material) were further compared with the 3D line results of the Comsol MF numerical model.

➢ *Validation of the Comsol model results in the metallic ring case*

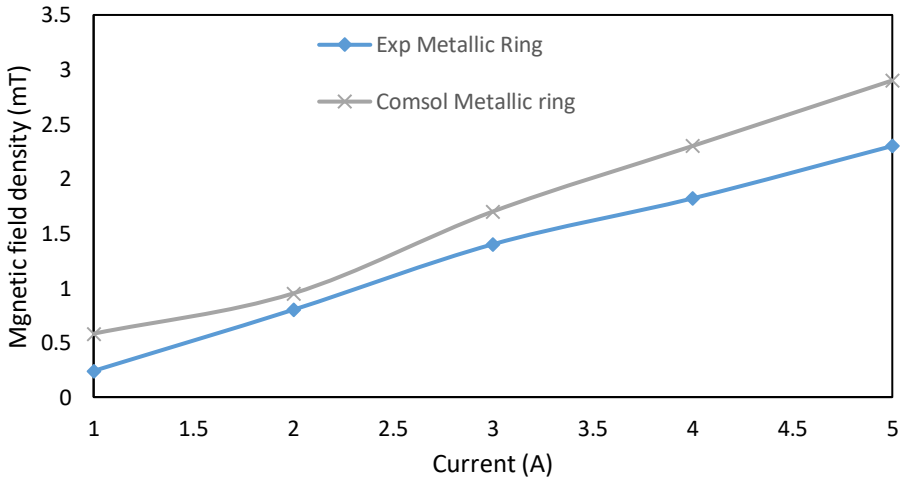

➢ *Validation of the Comsol model results in the plastic ring case*

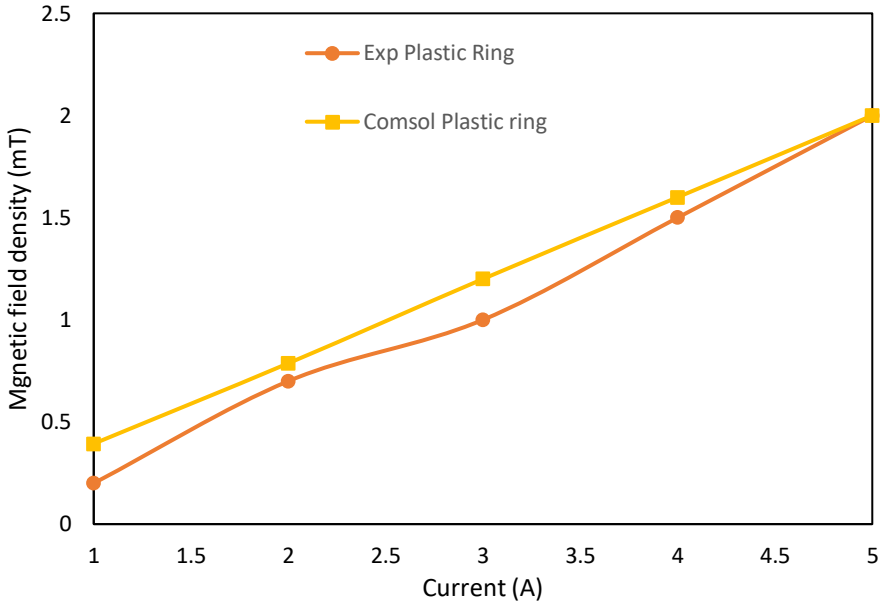

Appendix B: CFD analysis of the MRF damper

Continuing with the diaphragm contour pressure sample results mentioned in Figure.34, the figures below show the static pressure at the two chambers (Rebound and Compression).

- *Pressure contours at the rebound side*

0A

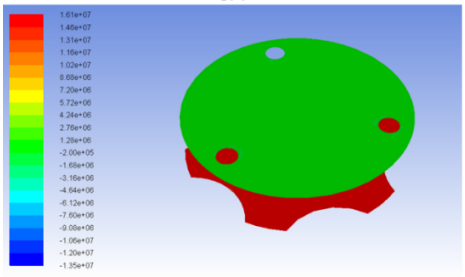

1A

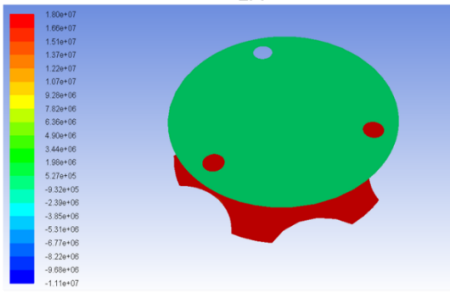

2A

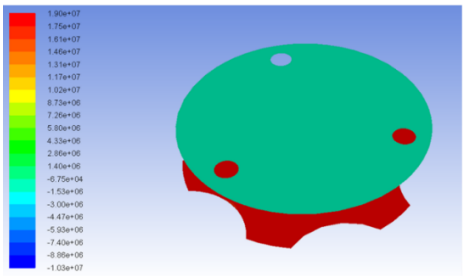

3A

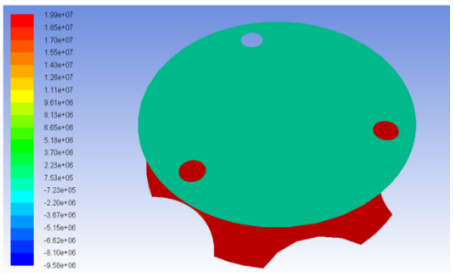

4A

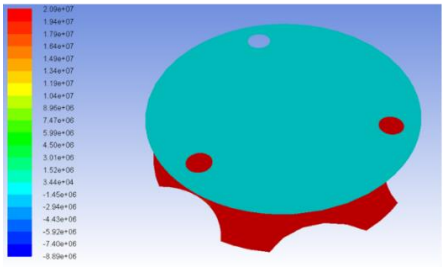

5A

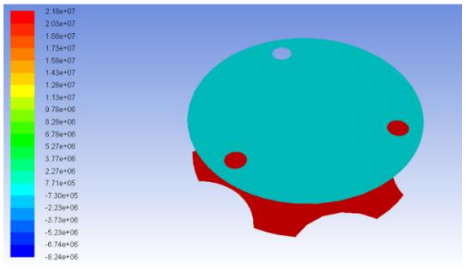

- *Pressure contours at the compression side*

0A

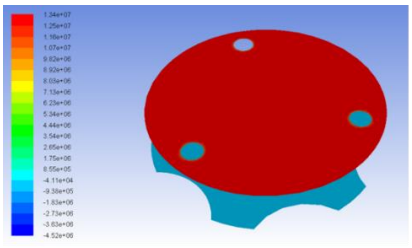

1A

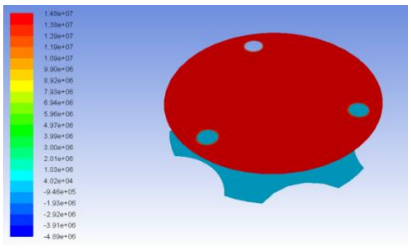

2A

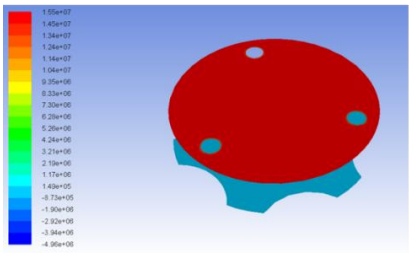

3A

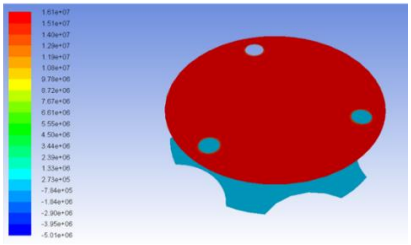

4A

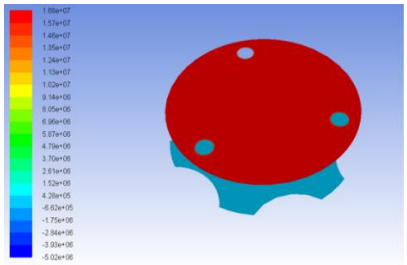

5A

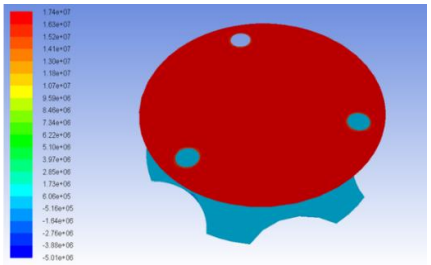

Appendix C: FIHD Numerical modeling

LS-Dyna software package provides numerous material models which simulate different materials' failure and collisions in many conditions and forms. LS-Dyna theory manual includes the below table, which eases the material model's selection based on the meshing element type, the scope of the study, and the material compound. The yellow squares highlight the material models used in the FIHD LS-Dyna model.

Material Models **LS-DYNA Theory Manual**

Material Number	Material Title	Bricks	Beams	Thin Shells	Thick Shells	Strain-Rate Effects	Failure	Equation-of-State	Thermal Effects	Notes: Gn General, Cm Composites, Cr Ceramics, Fl Fluids, Fm Foam, Gl Glass, Hy Hydro-dyn, Mt Metal, Pl Plastic, Rb Rubber, Sl Soil/Conc
21	Orthotropic Thermal (Elastic)	Y		Y	Y				Y	Gn
22	Composite Damage	Y		Y	Y		Y			Cm
23	Temperature Dependent Orthotropic	Y		Y	Y				Y	Cm
24	Piecewise Linear Plasticity (Isotropic)	Y	Y	Y	Y	Y	Y			Mt, Pl
25	Inviscid Two Invariant Geologic Cap	Y								Sl
26	Honeycomb	Y				Y	Y			Cm, Fm, Sl
27	Mooney-Rivlin Rubber	Y		Y						Rb
28	Resultant Plasticity		Y	Y						Mt
29	Force Limited Resultant Formulation		Y							
30	Closed Form Update Shell Plasticity			Y	Y					Mt
31	Slightly Compressible Rubber	Y								Rb
32	Laminated Glass (Composite)			Y	Y		Y			Cm, Gl
33	Barlat Anisotropic Plasticity	Y		Y	Y					Cr, Mt
34	Fabric			Y						
35	Plastic Green-Naghdi Rate	Y				Y				Mt
36	3-Parameter Barlat Plasticity			Y						Mt
37	Transversely Anisotropic Elastic Plastic			Y	Y					Mt
38	Blatz-Ko Foam	Y		Y						Fm, Pl
39	FLD Transversely Anisotropic			Y	Y					Mt
40	Nonlinear Orthotropic			Y			Y		Y	Cm
41-50	User Defined Materials	Y	Y	Y	Y	Y	Y	Y	Y	Gn
42	Planar Anisotropic Plasticity Model									

Material Number	Material Title	Bricks	Beams	Thin Shells	Thick Shells	Strain-Rate Effects	Failure	Equation-of-State	Thermal Effects	Notes:
										Gn General Cm Composites Cr Ceramics Fl Fluids Fm Foam Gl Glass Hy Hydro-dyn Mt Metal Pl Plastic Rb Rubber Sl Soil/Conc
177	Hill Foam									
178	Viscoelastic Hill Foam									
179	Low Density Synthetic Foam									
181	Simplified Rubber									
183	Simplified Rubber with Damage	Y		Y	Y	Y	Y			Rb
184	Cohesive Elastic	Y					Y			Cm, Mt
185	Cohesive TH	Y					Y			Cm, Mt
191	Seismic Beam		Y							
192	Soil Brick	Y								
193	Drucker Prager	Y								
194	RC Shear Wall			Y						
195	Concrete Beam		Y							
196	General Spring Discrete Beam		Y							
197	Seismic Isolator		Y				Y			Mt
198	Jointed Rock	Y					Y			
DS1	Spring Elastic (Linear)		Y							
DS2	Damper Viscous (Linear)		Y			Y				
DS3	Spring Elastoplastic (Isotropic)		Y							
DS4	Spring Nonlinear Elastic		Y			Y				
DS5	Damper Nonlinear Elastic		Y			Y				
DS6	Spring General Nonlinear		Y							